POLITECHNIKA POZNAŃSKA
WYDZIAŁ INŻYNIERII MATERIAŁOWEJ I FIZYKI TECHNICZNEJ
INSTYTUT INŻYNIERII MATERIAŁOWEJ

ROZPRAWA DOKTORSKA

Projektowanie właściwości stopów Ti-Mo metodami modyfikacji mikrostruktury i obróbki powierzchniowej do zastosowań medycznych

mgr inż. Patrycja SOCHACKA

Promotor*:* prof. dr hab. Mieczysław Jurczyk
Promotor pomocniczy: dr hab. inż. Andrzej Miklaszewski, prof. PP

Badania zrealizowano w ramach projektu finansowanego ze środków Narodowego Centrum Nauki UMO-2017/25/B/ST8/02494 „Projektowanie właściwości stopów tytanu typu beta metodami modyfikacji mikrostruktury i obróbki powierzchniowej dla aplikacji medycznych”

Poznań, 2021

Spis treści

STRESZCZENIE

Celem pracy było zaprojektowanie właściwości dwuskładnikowych stopów tytanu o strukturze β oraz pseudo β zawierających molibden (Ti-Mo). Zbadano wpływ zawartości molibdenu (10-35 at. %) na przemiany fazowe oraz właściwości mechaniczne stopów otrzymanych w procesach mechanicznej syntezy i metalurgii proszków (prasowanie na zimno i spiekanie lub prasowanie na gorąco). Dla stopu Ti23Mo przeprowadzono analizę porównawczą struktury i właściwości w zależności od metody otrzymywania. W celu poprawy biokompatybilności wytworzonych układów naniesiono powłoki apatytowe na wybranych stopach. Fluoroapatyt osadzono na utlenionej powierzchni (MAO) stopu Ti23Mo metodą elektroforetycznego osadzania, natomiast powłokę hydroksyapatytu z niewielką ilością $CaHPO_4 \cdot 2H_2O$ podczas obróbki hydrotermalnej na stopie Ti31Mo. Zmodyfikowano także skład chemiczny stopu Ti31Mo poprzez wprowadzenie hydroksyapatytu i wybranych dodatków antybakteryjnych: Ag, CeO_2, Ta_2O_5.

Dla otrzymanych biomateriałów przeprowadzono analizę: struktury krystalicznej z wykorzystaniem metod rentgenowskich, mikrostruktury za pomocą mikroskopii optycznej oraz skaningowej i transmisyjnej mikroskopii elektronowej, odporności korozyjnej w roztworze Ringera z wykorzystaniem potencjostatu, kątów zwilżalności metodą osadzania kropli oraz właściwości mechanicznych wykorzystując metody nanoindentacji (moduł Younga, twardość), a także badań mikrotwardości metodą Vickersa. Zbadano właściwości przeciwbakteryjne kompozytów w stosunku do szczepu *Staphylococcus aureus*. W pracy określono również cytokompatybilność stopów Ti31Mo przed i po modyfikacji powierzchni oraz kompozytów dla osteoblastów i fibroblastów więzadeł ozębnej.

Molibden jako stabilizator fazy Ti(β) umożliwił otrzymanie stopów jednofazowych w procesie prasowania na gorąco lub stopów pseudo β w procesie prasowania na zimno i spiekania. Zastosowanie procesu mechanicznej syntezy doprowadziło do znacznego rozdrobnienia mikrostruktury otrzymanych materiałów. Najniższe moduły Younga otrzymano dla kompozytów o niskiej porowatości (95 GPa, 4%) lub stopów charakteryzujących się wysoką porowatością (Ti31Mo 55 GPa, 29%). Modyfikacja powierzchni spowodowała polepszenie odporności korozyjnej stopów oraz zwilżalności powierzchni wpływając na poprawę proliferacji komórek kostnych. Żywotność osteoblastów oraz fibroblastów była wyższa lub zbliżona dla badanych kompozytów w porównaniu z tytanem mikrokrystalicznym. Ponadto dla biomateriałów zawierających srebro lub tlenek ceru (IV) współczynnik redukcji dla bakterii *S. aureus* wynosił ponad 97 %.

Wytworzone biomateriały z ultradrobnoziarnistą stukturą charakteryzują się lepszymi właściwościami niż mikrokrystaliczny tytan ze względu na potencjalne ich zastosowanie jako implanty dentystyczne lub endoprotezy stawu biodrowego. Modyfikacja składu chemicznego lub powierzchniowa, spowodowały obniżenie modułów Younga, poprawę odporności korozyjnej i biokompatybilności.

ABSTRACT

The work aimed to design the properties of titanium alloys with β and pseudo β structures containing molybdenum (Ti-Mo). The effect of molybdenum content was investigated (10-35 at. %) on phase transformations and mechanical properties of alloys obtained in the processes of mechanical synthesis and powder metallurgy (both cold and hot approach). On the other hand, a comparative analysis of the structure and properties of Ti23Mo alloys was carried out depending on the processing method. Proposed procedures of surface treatment led to the formation of apatite layers on selected alloys. Fluorapatite was deposited on the oxidized surface (MAO) of the Ti23Mo alloy by the application electrophoretic deposition method. After hydrothermal treatment of Ti31Mo alloy, the surface layer mostly consists of the $Ca_{10}(PO_4)_6(OH)_2$ with $CaHPO_4 \cdot 2H_2O$. The Ti31Mo alloy was also modified by introducing hydroxyapatite and selected antibacterial additives.

For the processed biomaterials was followed analysis of: structure by an X-ray diffractometer, microstructure by optical microscopy, scanning or transmission electron microscope, corrosion resistance in Ringer's solution by a potentiostat, wettability angles by droplet deposition, and mechanical properties (Young's modulus, hardness). The antibacterial activity of composites against *Staphylococcus aureus* was studied. The in vitro cytocompatibility of synthesized materials was also assayed for osteoblasts and fibroblasts.

Molybdenum as a Ti (β) phase stabilizer allowed to obtain single-phase alloys by applicated the hot pressing process or pseudo-β alloys by the cold pressing and sintering process. The application of the mechanical synthesis process leads to nano-scale size object formation. The lowest Young's modulus was obtained for composites with low porosity (95 GPa, 4%) or alloys with high porosity (Ti31Mo 55 GPa, 29%). The modification of the surface layer caused improvement of the corrosion resistance of the alloys and the wettability of the surface, thus improving the proliferation of bone cells. The viability of osteoblasts and fibroblasts was higher or similar for composites compared to microcrystalline titanium. Moreover, for biomaterials containing silver or cerium (IV) oxide, the reduction factor for *S. aureus* bacteria was over 97%.

The obtained ultrafine grain biomaterials have better properties than microcrystalline titanium, which causes their potential use as medical implants. Produced composites containing Ti-based alloys and bioceramic and antibacterial additives as a reinforced and surface modification of alloys resulted in the reduction of Young's modulus, improved corrosion resistance, and biocompatibility.

STRESZCZENIE GRAFICZNE (GRAPHICAL ABSTRACT)

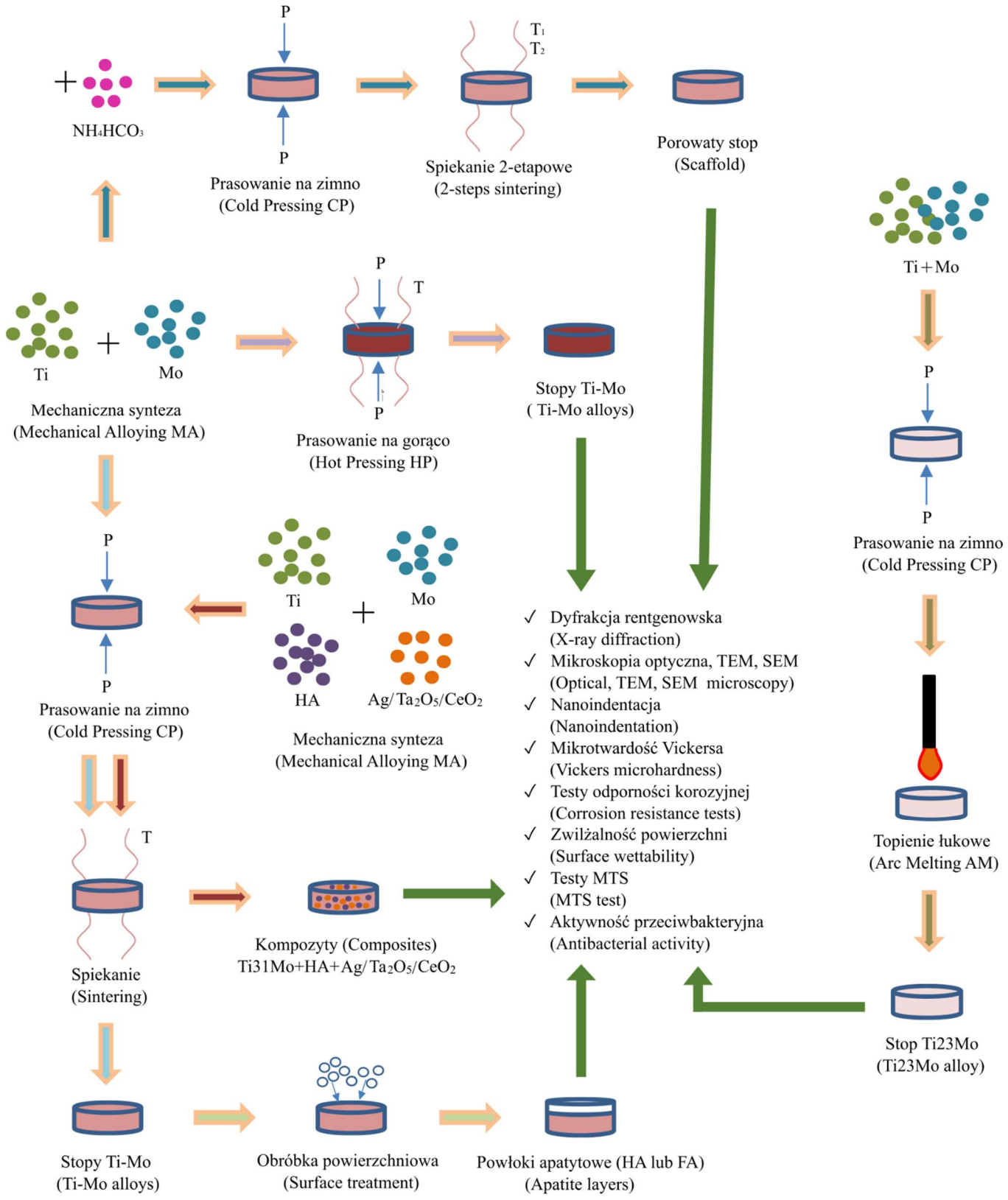

1. Wstęp

Z powodu coraz bardziej starzejącego się społeczeństwa poszukiwane są nowe rozwiązania dla medycyny, w tym ortopedii. W 2017 roku osoby powyżej 60 roku życia stanowiły 13% światowej populacji. Dla Europy wskaźnik ten wynosił aż 25% [1]. Wiek jest najistotniejszą przyczyną wpływającą na rozwój i progresję choroby zwyrodnieniowej stawów. Inne czynniki, jak otyłość, brak aktywności fizycznej, palenie tytoniu, nadmierne spożycie alkoholu oraz kontuzje powodują wzrost dolegliwości układu mięśniowo-szkieletowego [2]. Według danych Światowej Organizacji Zdrowia (ang. *World Health Organization* WHO) choroba zwyrodnieniowa stawów jest jedną z dziesięciu chorób powodujących największą niepełnosprawność w krajach rozwiniętych. W 2014 roku szacowano, że na całym świecie choruje na nią 10% mężczyzn i 18% kobiet w wieku powyżej 60 roku życia [3]. Od 2000 roku liczba zabiegów endoprotezoplastyki stawu biodrowego gwałtownie wzrosła w większości krajów należących do OECD (Organizacja Współpracy Gospodarczej i Rozwoju, ang. *Organisation for Economic Co-operation and Development).* Ilość wykonywanych operacji wymiany stawu biodrowego wzrosła o 30% w latach 2007-2017. [2, 4]. Problem chorób układu mięśniowo-szkieletowego wymusza poszukiwanie coraz lepszych, bezpieczniejszych i skuteczniejszych rozwiązań w zakresie implantologii [1, 5].

Ze względu na właściwości tytan i jego stopy stanowią najszerzej stosowaną grupę biomateriałów. Jednym z najpopularniejszych materiałów wykorzystywanym na implanty tkanki twardej jest stop tytanu Ti-6Al-4V [6-8]. Wykazuje on jednak istotne wady, takie jak wysoki moduł sprężystości, niska twardość, stosunkowo słaba odporność na zużycie ścierno-korozyjne [9, 10]. Ponadto aluminium i wanad mają bardzo negatywny wpływ na zdrowie człowieka, prowadząc m.in. do chorób neurologicznych takich jak Alzheimer czy Parkinson [9-10]. Jednym z rozwiązań umożliwiających poprawę jakości życia jest zastąpienie stopu Ti-6Al-4V nową generacją materiałów tytanowych typu β [11-13]. Charakteryzują się one wysoką odporność zmęczeniową, niskim modułem sprężystości, wysoką twardością i dobrą odpornością na korozję [7, 9]. Lepsze dopasowanie właściwości mechanicznych do właściwości kości względem stopów poprzednich generacji ogranicza obluzowywanie implantu na skutek resorpcji nieobciążonej kości (ang. *Stress shielding*) [14].

Dodatki stopowe wprowadzane do tytanu można podzielić na trzy grupy: stabilizujące fazę α (C, N, O, Al.), neutralne (Zr) i stabilizujące fazę β (V, Nb, Mo, Ta, Si, Cr, Mn, Fe, Co, Ni, W) [7, 9] Stabilizatory fazy β prowadzą do obniżenia temperatury przemiany fazowej $\alpha \rightleftharpoons \beta$

(882ºC dla tytanu). Faza Ti(α) krystalizuje w układzie heksagonalnym zwartym (P63/mmc), natomiast faza Ti(β) w regularnie przestrzennie centrowanym (Im-3m) [7, 15, 16]. Do nowej generacji stopów tytanu należą m. in. dwuskładnikowe stopy tytan-molibden. Stopy te wytwarzano różnymi metodami, m. in. topienia łukowego [17], przetapiania laserowego [18], czy w procesach obróbki cieplnej [19, 20]. Jednak do tej pory stopy Ti-Mo nie były otrzymywane w procesie mechanicznej syntezy (ang. *Mechanical Alloying* MA), która pozwala na uzyskanie materiałów trudnych lub niemożliwych do otrzymania konwencjonalnymi metodami topienia [21, 22]. Dodatkowo, proces ten pozwala na modyfikację właściwości stopów przez znaczne rozdrobnienie struktury do wielkości nanometrycznych, a w niektórych przypadkach poprzez powstawanie nowych faz [23].

Kompozyty na bazie tytanu lub jego stopów zawierające jako fazę wzmacniającą hydroksyapatyt (HA) lub bioszkło (BG) są obiecującą alternatywą w porównaniu z materiałami konwencjonalnymi [24-26]. Wpływ hydroksyapatytu na właściwości tytanu i jego stopów był przedmiotem wielu badań. Dodatek nanocząstek HA do tytanu spowodował wzrost twardości, obniżenie modułu Younga oraz poprawę odporności korozyjnej w porównaniu do tytanu mikrokrystalicznego [24]. Znaczna poprawa właściwości nastąpiła również poprzez wprowadzenie do stopu Ti23Mo bioszkła w połączeniu z modyfikacją warstwy wierzchniej [25].

Wraz ze wzrostem konieczności stosowania implantów medycznych rośnie możliwość występowanie infekcji oraz niepowodzenia integracji. W związku z tym istotne jest opracowanie biokompatybilnych materiałów łączących funkcje antyinfekcyjne z doskonałymi właściwościami osteointegracyjnymi [27].

Zarówno bakterie gram-dodatnie, jak i gram-ujemne mogą tworzyć biofilmy na wyrobach medycznych. Najczęściej występującymi szczepami są *Enterococcus faecalis, Staphylococcus aureus, Staphylococcus epidermidis, Streptococcus viridans, Escherichia coli, Klebsiella pneumoniae, Proteus mirabilis* i *Pseudomonas aeruginosa* [28]. Gatunki gronkowców stanowią zróżnicowaną grupę bakterii gram-dodatnich, zasiedlających głównie skórę i błony śluzowe człowieka oraz innych ssaków. Szacuje się, że spośród nich *Staphylococcus aureus* oraz *Staphylococcus epidermidis* są główną przyczyną zakażeń miejsca operowanego i 87% zakażeń krwi [28-31]. Dwie trzecie zakażeń związanych z implantologią jest wywołanych przez gronkowce, spośród których większość stanowią *S. aureus* oraz gronkowce koagulazo-ujemnymi [32, 33]. W celu zminimalizowania ryzyka zakażenia ważne jest wprowadzanie dodatków antybakteryjnych jako dodatkowych składników materiału bądź modyfikatorów warstwy wierzchniej. Ostatnie badania wykazały

aktywność przeciwbakteryjną ceramiki szklanej domieszkowanej Ta_2O_5 wobec bakterii bakterii gram-dodatnich: *Streptococcus pyogenes, Bacillus subtilis* i *Staphylococcus epidermidis* [34]. Natomiast nanocząstki tlenku ceru wykazują aktywność przeciwbakteryjną wobec *Escherichia coli* [35, 36]. Wykazano także podobne działanie srebra względem *S. aureus* [37].

Poprawę właściwości i biokompatybilności stopów przeznaczonych na implanty można osiągnąć nie tylko modyfikując skład materiału i jego mikrostrukturę, ale także przez modyfikację warstwy wierzchniej [25]. W przypadku implantów obróbka powierzchniowa jest stosowana m. in. w celu zmiany topografii i poprawy zwilżalności powierzchni, aby zwiększyć aktywność proliferacyjną komórek kostnych oraz poprawić proces osteointegracji [25, 38-41]. Jedną z grup materiałów wykorzystywanych na biokompatybline powłoki są fosforany wapnia, w tym hydroksyapatyt, szczawian wapnia $CaHPO_4 \cdot 2H_2O$, czy fluoroapatyt. [25, 27, 40-42]

W ramach prowadzonych badań wytworzono dwuskładnikowe stopy Ti-Mo metodą mechanicznej syntezy i metalurgii proszków. W pracy zbadano wpływ metody otrzymywania na właściwości stopów. W celu dalszej poprawy właściwości mechanicznych, ale także antybakteryjnych i biologicznych, zmodyfikowano ich skład chemiczny tworząc układy kompozytowe z hyroksyapatytem, oraz srebrem, tlenkiem tantalu (V) lub tlenkiem cyrkonu (IV), a także wytworzono powłoki fluoroapatytu lub hydroksyapatywu z niewielką ilością $CaHPO_4 \cdot 2H_2O$.

[1] M. Spector, Biomedical materials to meet the challenges of the aging epidemic, Biomed. Mater. 13 (2018) 030201. https://doi.org/10.1088/1748-605X/aab171

[2] OECD (2019) Hip and Knee Replacement, Health at a Glance 2019, OECD Publishing. Paris. https://doi.org/10.1787/4dd50c09-en

[3] WHO (2014), "Chronic Rheumatic Conditions", Fact Sheet, http://www.who.int/chp/topics/rheumatic/en/.

[4] I. Wallace, S. Worthington, et al., Knee osteoarthritis has doubled in prevalence since the mid-20th century, PNAS 114 (2017) 9332-9336. http://dx.doi.org/10.1073/pnas.1703856114

[5] V.M. Goldberg, J. A. Buckwalter, W. C. Hayes, K. J. Koval, Orthopaedic challenges in an aging population., Instr. Course Lect. 46 (1997) 417–422.

[6] C. Leyens, M. Peters, Titanium and Titanium Alloys: Fundamentals and Applications, Wiley-VCH Verlag GmbH & Co. (2005). https://doi.org/10.1002/3527602119

[7] H. J. Rack, J. J. Qazi, Titanium alloys for biomedical applications, Mater. Sci. Eng. C 26 (2006) 1269-1277. https://doi.org/10.1016/j.msec.2005.08.032

[8] M. Geetha, A. K. Singh, R. Asokamani, A. K. Gogia, Ti based biomaterials, the ultimate choice for orthopedic implants – a review, Prog. Mater. Sci. 54 (2009) 397-425. https://doi.org/10.1016/j.pmatsci.2008.06.004

[9] J. Y. Rho, R. B. Ashman, C. H. Turner, Youngs modulus of trabecular and cortical bone material - ultrasonic and microtensile measurements, J. Biomech. 26 (1993) 111-119. https://doi.org/10.1016/0021-9290(93)90042-d

[10] M. Valko, H. Morris, M. T. D. Cronin, Metals, toxicity and oxidative stress, Curr. Med. Chem. 12 (2005) 1161-1208. https://doi.org/10.2174/0929867053764635

[11] L. C. Zhang, L. Y. Chen, A Review on Biomedical Titanium Alloys: Recent Progress and Prospect, Adv. Eng. Mater. 21 (2019) 1801215. https://doi.org/10.1002/adem.201801215

[12] M. Kaur, K. Singh, Review on titanium and titanium based alloys as biomaterials for orthopaedic applications, Mater. Sci. Eng. C 102 (2019) 844-862. https://doi.org/10.1016/j.msec.2019.04.064

[13] M. T. Mohammed, Z. A. Khan, A. N. Siddiquee, Beta Titanium Alloys: The Lowest Elastic Modulus for Biomedical Applications: A Review, Int. J. Chem. Nucl. Metall. Mater. Eng. 8 (2014) 726–731. https://doi.org/10.5281/zenodo.1094481

[14] J. Nagels, M. Stokdijk, P. M. Rozing, Stress shielding and bone resorption in shoulder arthroplasty, J. Shoulder Elb. Surg. 12 (2003) 35–39. https://doi.org/10.1067/mse.2003.22

[15] D. Kuroda, M. Niinomi, M. Morinaga, Y. Kato, T. Yashiro, Design and mechanical properties of new β type titanium alloys for implant materials, Mater. Sci. Eng. A. 243 (1998) 244–249. https://doi.org/10.1016/s0921-5093(97)00808-3.

[16] A. T. Sidambe, Biocompatibility of advanced manufactured titanium implants-A review, Materials (Basel) 7 (2014) 8168–8188. https://doi.org/10.3390/ma7128168

[17] D. J. Lin, C. C. Chuang, J. H. Chern Lin, J. W. Lee, C. P. Ju, H. S. Yin, Bone formation at the surface of low modulus Ti–7.5Mo implants in rabbit femur Biomaterials, 28 (2007) 2582-2589. https://doi.org/10.1016/j.biomaterials.2007.02.005

[18] A. Almeida, D. Gupta, C. Loable, R. Vilar, Laser-assisted synthesis of Ti–Mo alloys for biomedical applications, Mater. Sci. Eng. C 32 (2012) 1190-1195. https://doi.org/10.1016/j.msec.2012.03.007

[19] C. H. Wang, M. Liu, P. F. Hu, J. C. Peng, J. A. Wang, Z. M. Ren, G. H. Cao, The effects of a″ and ω phases on the superelasticity and shape memory effect of binary Ti-Mo alloys, J. Alloys Compd. 720 (2017) 488-496. https://doi.org/10.1016/j.jallcom.2017.05.299

[20] F. F. Cardoso, P. L. Ferrandini, E. S. N. Lopes, A. Cremasco, R. Caram, Ti–Mo alloys employed as biomaterials: effects of composition and aging heat treatment on microstructure and mechanical behawior, J. Mech. Behav. Biomed. Mater. 32 (2014) 31-38. https://doi.org/10.1016/j.jmbbm.2013.11.021

[21] R. Z. Valiev, I. P. Semenova, E. Jakushina, V. V. Latysh, H. Rack, R. C. Lowe, J. Petruželka, L. Dluhoš, D. Hrušák, J. Sochová, Nanostructured SPD processed titanium for medical implants, Mater. Sci. Forum 584-6 (2008) 49-54. https://doi.org/10.4028/www.scientific.net/MSF.584-586.49

[22] K. Y. Xie, Y. B. Wang, Y. H Zhao, L. Chang, G. C. Wang, Z. B. Chen, Y. Cao, X. Z. Liao, E. J. Lavernia, R. Z. Valiev, B. Sarrafpour, H. Zoellner, S. P. Ringer, Nanocrystalline beta-Ti alloy with high hardness, low Young's modulus and excellent in vitro biocompatibility for biomedical applications, Mater. Sci. Eng. C-Mater. Biol. Appl. 33 (2013) 3530-3536. https://doi.org/10.1016/j.msec.2013.04.044

[23] L. Zhang, T. J. Webster, Nanotechnology and nanomaterials: promises for improved tissue regeneration, Nano Today 4 (2009) 66-80. https://doi.org/10.1016/j.nantod.2008.10.014

[24] K. Niespodziana, K. Jurczyk, J. Jakubowicz, M. Jurczyk, Fabrication and properties of titanium – hydroxyapatite nanocomposites, Mater. Chem. Phys 123 (2010) 160-165. https://doi.org/10.1016/j.matchemphys.2010.03.076

[25] M. U. Jurczyk, K. Jurczyk, A. Miklaszewski, M. Jurczyk, Nanostructured titanium-45S5 Bioglass scaffold composites for medical applications, Mater. Des. 32 (2011) 4882-4889. https://doi.org/10.1016/j.matdes.2011.06.005

[26] M. Tulinski, M. Jurczyk, Nanostructured nickel-free austenitic stainless steel composites with different content of hydroxyapatite, Appl. Surf. Sci. 260 (2012) 80-83. https://doi.org/10.1016/j.apsusc.2012.07.071

[27] Z. Xue, Z. Wang, A. Sun, J. Huang, W. Wu, M. Chen, X. Hao, Z. Huang, X. Lin, S. Weng, Rapid construction of polyetheretherketone (PEEK) biological implants incorporated with brushite (CaHPO4·2H2O) and antibiotics for anti-infection and enhanced osseointegration, Mater Sci Eng C 111 (2020) 110782. https://doi.org/10.1016/j.msec.2020.110782.

[28] M. Chen, Q. Yu, H. Sun, Novel strategies for the prevention and treatment of biofilm related infections, Int. J. Mol. Sci. 14(2013) 18488–18501. https://doi.org/10.3390/ijms140918488

[29] M. Zaborowska, J. Tillander, R. Branemark, L. Hagberg, P. Thomsen, M. Trobos, Biofilm formation and antimicrobial susceptibility of staphylococci and enterococci from osteomyelitis associated with percutaneous orthopaedic implants. J. Biomed. Mater. Res. B. 105 (2017) 2630–2640. https://doi.org/10.1002/jbm.b.33803

[30] W. F. Oliveira, P. M. S. Silva, R. C. S.Silva, G. M. M.Silva, G. Machado, L. Coelho, M. T. S. Correia, Staphylococcus aureus and Staphylococcus epidermidis infections on implants, J. Hosp. Infect. 98 (2018) 111–117. https://doi.org/10.1016/j.jhin.2017.11.008

[31] Y. Zheng, L. He, T. K. Asiamah, M. Otto, Colonization of medical devices by staphylococci, J. Appl. Environ. Microbiol. 20 (2018) 3141–3153. https://doi.org/10.1111/1462-2920.14129

[32] R. O. Darouiche, Treatment of infections associated with surgical implants. N. Engl. J. Med. 350 (2004) 1422–1429. https://doi.org/10.1056/NEJMra035415

[33] M. Ribeiro, F. J. Monteiro, M. P. Ferraz, Infection of orthopedic implants with emphasis on bacterial adhesion process and techniques used in studying bacterial-material interactions. Biomatter. 2 (2012) 176–194. https://doi.org/10.4161/biom.22905

[34] M. Riaz, R. Zia, F. Saleemi, T. Hussain, In vitro antibacterial activity of that Ta2O5 doped glass-ceramic against pathogenic bacteria, J. Alloy. Comp. 764 (2018), 10-16. https://doi.org/10.1016/j.jallcom.2018.06.053

[35] D. A. Pelletier, A. K. Suresh, G. A. Holton, et al., Effects of engineered cerium oxide nanoparticles on bacterial growth and viability, Appl. Environ. Microbiol. 76 (2010) 7981-7989. https://doi.org/10.1128/AEM.00650-10

[36] A. Thill, O. Zeyons, O. Spalla, et al., Cytotoxicity of CeO2 nanoparticles for Escherichia coli. physico-chemical insight of the cytotoxicity mechanism, Environ. Sci. Technol. 40 (2006) 6151-6156. https://doi.org/10.1021/es060999b

[37] B. Joshi, C. Regmi, D. Dhakal, G. Gyawali, S.W. Lee, Efficient inactivation of Staphylococcus aureus by silver and copper loaded photocatalytic titanate nanotubes, Pro Nat Sci-Mater 28 (2018) 15-23. https://doi.org/10.1016/j.pnsc.2018.01.004

[38] T. J. Webster, J. U. Ejiofor Increased osteoblast adhesion on nanophase metals: Ti, Ti6Al4V, and CoCrMo, Biomaterials, 25 (2004), 4731-4739. https://doi.org/10.1016/j.biomaterials.2003.12.002

[39] A. Jemat, M. J. Ghazali, M. Razali, Y. Otsuka, Surface Modifications and Their Effects on Titanium Dental Implants, Biomed Res. Int. 2015 (2015) 791725. https://doi.org/10.1155/2015/791725

[40] S. Abbasi, M. R. Bilesan, F. Golestani-Fard, In vitro evaluation of the biocompatibility and bioactivity of plasma electrolyte oxidized titania/calcium phosphate nanocoatings on Ti, J. Mater. Sci. 54 (2019) 4277–4286. https://doi.org/10.1007/s10853-018-3147-x

[41] Y. Li, I. S. Lee, F. Z. Cui, S. H. Choi, The biocompatibility of nanostructured calcium phosphate coated on micro-arc oxidized titanium, Biomaterials. 29 (2008) 2025–2032. https://doi.org/10.1016/j.biomaterials.2008.01.009

[42] S Overgaard, M Lind, H Glerup, S Grundvig, C. Bünger, K Søballe, Hydroxyapatite and fluorapatite coatings for fixation of weight loaded implants, Clin Orthop Relat Res 336 (1997) 286-96. https://doi.org/10.1097/00003086-199703000-00037

2. Cel i zakres pracy

Celem pracy było zaprojektowanie właściwości stopów tytanu o strukturze β oraz pseudo β zawierających molibden (Ti-Mo). Materiały wytworzono metodami mechanicznej syntezy oraz metalurgii proszków. Następnie modyfikowano ich skład, dodając hydroksyapatyt i wybrane dodatki antybakteryjne, tworząc układy kompozytowe, a także zastosowano metody obróbki powierzchniowej. Powzięte kroki przeprowadzono w celu poprawy biokompatybilności stopów tytanu wykorzystywanych w medycynie, szczególnie poprzez eliminację szkodliwych dla zdrowia dodatków stopowych, takich jak aluminium i wanad o działaniu neurotoksycznym. Wytworzenie układów tytan-molibden oraz kompozytów miało także polepszyć właściwości użytkowe materiałów do zastosowań medycznych. Przeprowadzono modyfikację mikrostruktury otrzymanych stopów Ti-Mo, aby zredukować moduły Younga materiałów, poprawić ich odporność korozyjną w środowisku płynów ustrojowych, zwiększyć biozgodność oraz aktywność antybakteryjną względem szczepu *Staphylococcus aureus* (gronkowca złocistego). Natomiast zastosowane metody obórki powierzchniowej przeprowadzono w celu poprawy biokompatybilności oraz odporności korozyjnej.

Zrealizowano szczegółowe zadania w ramach cyklu monotematycznych publikacji, do których należały:

a) wytworzenie stopów tytan-molibden Ti-x at. % Mo (x=10, 23, 27, 31 i 35) o drobnoziarnistej strukturze, wykorzystując metodę mechanicznej syntezy przy czasie mielenia 48 h oraz procesy metalurgii proszków. Otrzymane proszki były prasowane jednoosiowo na zimno pod ciśnieniem 600 MPa, a następnie spiekane w temperaturach 600-1000°C przez 30 min lub indukcyjnie prasowane na gorąco w temperaturze 800°C pod ciśnieniem 60 MPa przez 5 min. Zbadano wpływ składu chemicznego i metody obróbki na mikrostrukturę oraz właściwości mechaniczne stopów. Zmiany składu fazowego scharakteryzowano metodą dyfrakcji rentgenowskiej podczas mielenia oraz po konsolidacji. Na podstawie otrzymanych dyfraktogramów rentgenowskich wyznaczono wielkość krystalitów i odkształcenia sieci po procesie mechanicznej syntezy metodą Williamsona-Halla oraz przeprowadzono jakościową oraz ilościową (metoda Rietvielda) analizę fazową stopów. Do scharakteryzowania mikrostruktury, składu chemicznego i rozkładu poszczególnych pierwiastków wykorzystano skaningowy mikroskop elektronowy (ang. *scanning electron microscope* SEM) ze spektrometrem dyspersji energii (ang. *energy dispersive spectometry* EDS). Do analizy mikrostrukturalnej

próbki zostały wypolerowane i następnie wytrawione w odczynniku Krolla. Obserwacji z wykorzystaniem skaningowej mikroskopii elektronowej poddano również proszki przed i po mechanicznej syntezie. Natomiast wysokorozdzielcza mikroskopia elektronowa (HRTEM) umożliwiła dokładniejszą analizę mikrostruktury, wraz z wyznaczeniem wzorców krystalograficznych. Ponadto oceniono na podstawie histogramów obrazów z mikroskopu optycznego porowatość stopów, a wykorzystując wagę hydrostatyczną wyznaczono gęstości spieków. Charakterystyka otrzymanych stopów obejmowała również badania mechaniczne. Wyznaczono moduły Younga metodą nanoindentacji oraz twardości stopów metodą Martensa oraz Vickersa.

b) wytworzenie dwuskładnikowych stopów Ti-23 at. % Mo (Ti23Mo) metodami topienia łukowego lub mechanicznej syntezy oraz metalurgii proszków. Mikrokrystaliczny stop Ti23Mo otrzymano przez trzykrotne topienie łukowe proszków przy ciągłym przepływie argonu, poprzednio sprasowanych na zimno pod ciśnieniem 600 MPa. Dodatkowo stop był wyżarzany w temperaturze 800°C przez 24 h. Kolejne stopy Ti23Mo wytworzono, jak poprzednio, wykorzystując metodę mechanicznej syntezy oraz procesy metalurgii proszków. Otrzymane proszki były prasowane jednoosiowo na zimno pod ciśnieniem 600 MPa i spiekane w temperaturze 800°C przez 30 min lub indukcyjnie prasowane na gorąco w temperaturze 800°C pod ciśnieniem 60 MPa przez 5 min. Ponadto wytworzono porowaty stop (ang. *scaffold*) poprzez dodanie do proszku, po procesie mechanicznej syntezy, środka porotwórczego wodorowęglanu amonu (NH_4HCO_3). Otrzymaną wypraskę podczas prasowania na zimno spiekano w próżni 10^{-2} Pa w dwóch etapach: 175°C przez 2 h w celu usunięcia cząsteczek środka porotwórczego oraz w temperaturze 1150°C przez 10 h. Charakterystyka otrzymanych stopów obejmowała analizę strukturalną pod względem jakościowym i ilościowym, a także obserwację mikrostruktury z wykorzystaniem mikroskopu optycznego oraz skaningowego mikroskopu elektronowego. Określono skład chemiczny stopów metodą EDS. Wyznaczono także gęstość, porowatość oraz właściwości mechaniczne, takie jak moduł Younga metodą nanoindetnacji, twardość Martenssa, czy mikrotwardość metodą Vickersa. Oceniono również odporność korozyjną stopów w roztworze Ringera. Na podstawie krzywych polaryzacji obliczono ubytek masy zgodnie z prawem Faradaya oraz poprzez pomiar masy próbek przed i po zanurzeniu w roztworze Ringera przez 14 dni. Kolejnym zadaniem zrealizowanym w tej pracy była modyfikacja powierzchni wybranych stopów poprzez utlenianie mikro-łukowe (ang. *micro-arc oxidation* MAO) przy stałym napięciu 250 V przez 3 min w roztworze 0,01 M fosforanu

wapnia i 0,5 M kwasu cytrynowego oraz osadzanie elektroforetyczne (ang. *electrophoretic deposition* EPD) fluoroapatytu przy napięciu -200 V przez 1 min w etanolu. Dla stopu Ti23Mo po każdym etapie modyfikacji powierzchni wyznaczono skład fazowy z użyciem dyfraktometru rentgenowskiego, oceniono morfologię z wykorzystaniem SEM, zbadano odporność korozyjną oraz dokonano pomiarów zwilżalności powierzchni.

c) wytworzenie kompozytów na bazie stopu Ti-31 at. % Mo (Ti31Mo) zawierających hydroksyapatyt (HA) 2,5-10 wag. % oraz dla zawartości 5 wag. % HA dodatki antybakteryjne takie jak: srebro Ag (1 wag. %), tlenek tantalu (V) Ta_2O_5 (2 wag. %) lub tlenek ceru CeO_2 (IV) (2 wag. %). Czas procesu wynosił 39 h. Otrzymane materiały poddano jednoosiowemu prasowaniu na zimno pod ciśnieniem 600 MPa i spiekaniu w temperaturze 800°C przez 30 min. Charakterystyka obejmowała, podobnie jak przy stopach niemodyfikowanych, analizę strukturalną podczas mielenia i po konsolidacji. Wyznaczono wielkość krystalitów metodą Williamsona-Halla oraz określono zawartość poszczególnych faz w kompozytach metodą Rietvelda. Dokonano obserwacji mikrostruktury otrzymanych materiałów za pomocą mikroskopii SEM, przeanalizowano skład chemiczny oraz rozkład pierwiastków metodą EDS. Wyznaczano także gęstość i porowatość kompozytów oraz właściwości mechaniczne (moduł Younga, mikrotwardość), zwilżalność powierzchni i odporność korozyjną w roztworze Ringera. Ponadto dla kompozytów Ti31Mo5HA oraz zawierających srebro, tlenek tantalu (V) lub tlenek ceru (IV) zbadano właściwości przeciwbakteryjne w stosunku do szczepu *Staphylococcus aureus*.

d) modyfikacja powierzchni stopu Ti31Mo metodą hydrotermalną. W pierwszym etapie materiały zanurzano w 5 M roztworze wodorotlenku sodu przez 24 h w temperaturze 60°C. Następnie na powierzchni stopu osadzono warstwę Ca/P składającą się głównie z hydroksyapatytu przez zanurzenie próbek w temperaturze 120°C przez 2 h w elektrolicie zawierającym 0,25 M wersenianu wapniowo-disodowego oraz 0,25 M fosforanu dipotasu rozpuszczonych w 1 M roztworze wodorotlenku sodu. Dla materiałów po modyfikacji powierzchniowej przeprowadzono analizę strukturalną z wykorzystaniem dyfraktometru rentgenowskiego. Dokonano obserwacji morfologii i przekroju poprzecznego otrzymanej powłoki wykorzystując skaningową mikroskopię elektronową, a także wyznaczono skład chemiczny oraz rozkład pierwiastków metodą EDS. Za pomocą profilometru optycznego oszacowano parametry chropowatości powierzchni po każdym etapie wytwarzania powłoki. Oceniono także zwilżalność powierzchni i odporność korozyjną stopu Ti31Mo po obróbce powierzchniowej. Zbadano również

cytokompatybilność *in vitro* stopów Ti31Mo przed i po modyfikacji powierzchni oraz kompozytów Ti31Mo5HA, Ti31Mo5HA-Ag(lub Ta_2O_5, CeO_2) względem tytanu mikrokrystalicznego z wykorzystaniem osteoblastów (NHost) i fibroblastów więzadeł ozębnej (HpdLF).

3. Wyniki badań

3.1.Stopy dwuskładnikowe Ti-Mo

Dwuskładnikowe stopy Ti-Mo zawierające 10, 23, 27, 31 oraz 37 at. % molibdenu zostały wytworzone metodami mechanicznej syntezy i metalurgii proszków. Otrzymane proszki skonsolidowano przez jednoosiowe prasowanie na zimno pod ciśnieniem 600 MPa i spiekanie w temperaturach: 600, 700, 800 i 1000ºC przez 30 min w atmosferze argonu [1, 2].

Dla wszystkich koncentracji molibdenu w stopach Ti-Mo przeprowadzono analizę zmiany struktury krystalicznej podczas procesu mechanicznej syntezy (Rysunek 1 [1]). Dla zawartości powyżej 10 at. % molibdenu w czasie od 15 min do 48 h zachodziła przemiana fazowa Ti(α)→Ti(β). Mielenie mikrokrystalicznych proszków przez 48 h prowadziło do powstania dwufazowej struktury Ti(β)+TiMo. Dyfraktogramy stopów Ti23Mo oraz Ti31Mo przedstawiono na **Rysunku 1**. Jednofazowy stop Ti(β) otrzymano już po 15 h procesu mechanicznej syntezy dla koncentracji 35 at. % molibdenu. Wydłużenie czasu mielenia do 48 h spowodowało przemianę Ti(β)→TiMo. Natomiast dla niskiej koncentracji molibdenu, tzn. 10 at. %, otrzymano dwufazową strukturę Ti(α)+TiMo niezależnie od czasu trwania mielenia. Po zakończonym procesie mechanicznej syntezy otrzymano prawie amorficzne proszki charakteryzujące się wysokim stopniem rozdrobnienia. Wielkość krystalitów wyznaczona metodą Williamsona-Halla wynosiła 5,5-19 nm (Rysunek 2 [1], Tabela 1 [1]).

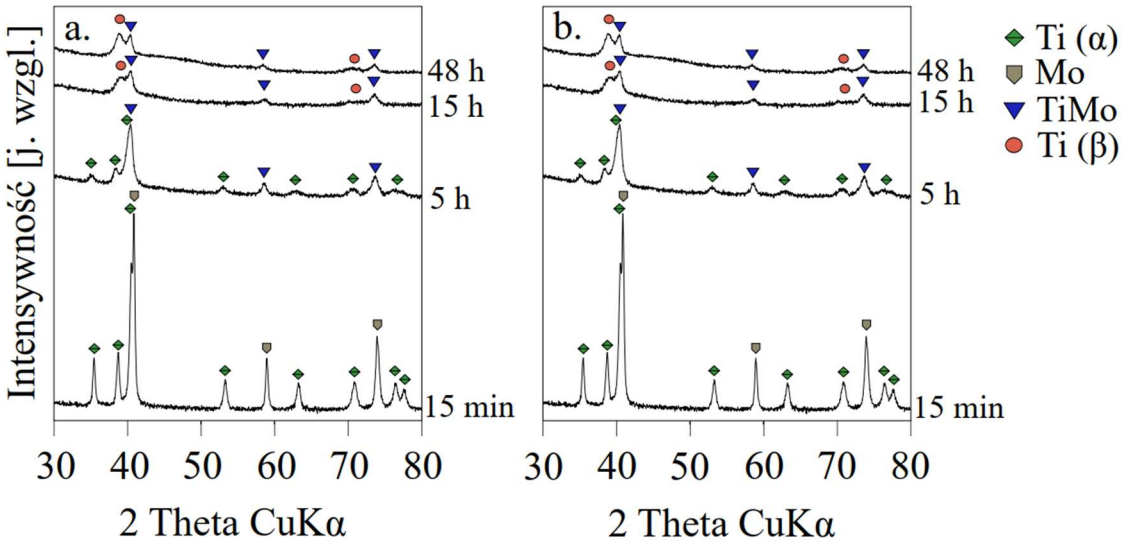

Rysunek 1. Dyfraktogramy rentgenowskie stopów Ti23Mo (a) oraz Ti31Mo (b) podczas procesu mechanicznej syntezy [1]

Temperatura spiekania, a także zawartość molibdenu w istotny sposób wpływały na strukturę krystaliczną stopów. Metodą prasowania na zimno i spiekania w temperaturach od 600 do 1000°C otrzymano porowate (25-28%) stopy zawierające głównie fazę Ti(β) oraz fazę Ti(α). Większa zawartość molibdenu powodowała powstawanie dodatkowej fazy przejściowej TiMo o strukturze regularnej przestrzennie centrowanej, wykazującej tendencję do krystalizacji w kierunku molibdenu. Występowała ona w stopach o zawartości od 23 at. % molibdenu spiekanych w temperaturze 600°C oraz dla 31 at. % w temperaturze 700ºC. W przypadku stopu Ti35Mo we wszystkich analizowanych temperaturach spiekania widoczne były trzy fazy: Ti(β), Ti(α) i TiMo. Natomiast zawartość fazy Ti(β) we wszystkich syntetyzowanych stopach wzrastała wraz ze wzrostem temperatury spiekania. Finalną strukturę stopów Ti-Mo można kształtować przez odpowiednio dobraną temperaturę spiekania. Wzrost zawartości molibdenu powodował zmniejszenie rozmiaru regularnej komórki tytanu. Udziały fazowe oraz parametry sieci krystalograficznych badanych stopów określono metodą Rietvelda (Tabele 2-3 [1])

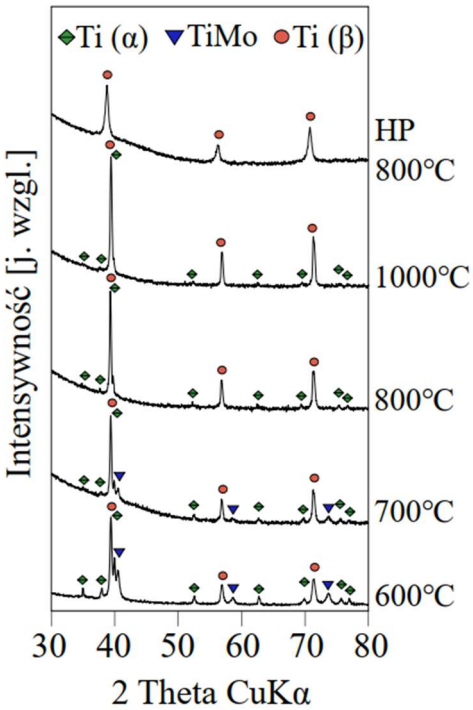

Rysunek 2. Dyfraktogramy rentgenowskie stopów Ti31Mo prasowanych na zimno i spiekanych w temperaturach 600-1000ºC oraz prasowanego na gorąco w temperaturze 800ºC [1]

Lite stopy typu Ti(β) otrzymano w wyniku zastosowania indukcyjnego prasowania na gorąco w temperaturze 800ºC przez 5 min dla zawartości molibdenu 23-31 at. %. Dla najniższej i najwyższej analizowanej koncentracji otrzymano materiał o strukturze dwufazowej. Poza dominującą fazą regularną tytanu występowało ok. 27% fazy Ti(α') w stopie

Ti10Mo lub ok. 16% fazy TiMo w stopie Ti35Mo. W wyniku oddziaływania wysokiej temperatury oraz ciśnienia porowatość tych materiałów nie przekraczała 0,25%. Dyfraktogramy stopów spiekanych w temperaturach 600-1000ºC oraz prasowanych na gorąco przedstawiono na Rysunku 4 [1]. Na **Rysunku 2** zestawiono widma rentgenowskie stopu Ti31Mo.

Wytworzone stopy charakteryzowały się drobnoziarnistą strukturą (Rysunek 7 [1]). Dla stopu Ti27Mo prasowanego na gorąco w celu potwierdzenia uzyskanej mikrostruktury przeprowadzono obserwacje przy użyciu transmisyjnego mikroskopu elektronowego. Sprawdzono strukturę krystalograficzną stopu za pomocą dyfrakcji elektronów. Analizowany wzór dyfrakcyjny potwierdza strukturę regularnie przestrzennie centrowaną odpowiadającą odmianie alotropowej Ti(β) (**Rysunek 3**, Rysunek 8 [1])

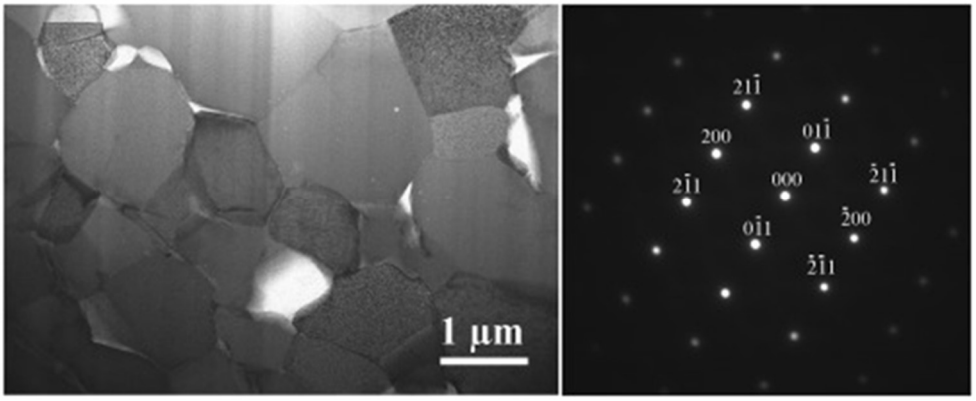

Rysunek 3. Obraz TEM dla stopu Ti-27 at.% Mo po prasowaniu na gorąco w temperaturze 800°C z dyfrakcją elektronów dla jednego z ziaren [1]

Sposób wytwarzania stopów Ti-Mo ma istotny wpływ na strukturę fazową, mikrostrukturę oraz właściwości. Dla wybranej koncentracji molibdenu – 23 at. % – zastosowano także inne metody otrzymywania [2]. Proszki tytanu i molibdenu wymieszano, sprasowano na zimno, a następnie trzykrotnie przetapiano metodą topienia łukowego przy ciągłym przepływie argonu. W wyniku zastosowanego procesu otrzymano jednofazowy stop Ti(β). W kolejnym etapie mikrokrystaliczny materiał został wyżarzony w temperaturze 800ºC przez 24 h. Zastosowana obróbka cieplna spowodowała wydzielenie ok. 17% fazy Ti(α') oraz spadek porowatości z 0,31% do 0,06%. Ponadto otrzymano jednofazowy stop podczas wytwarzania materiału porowatego poprzez dodanie środka porotwórczego do proszku otrzymanego w procesie mechanicznej syntezy i poddanego dwuetapowemu spiekaniu. Materiał ten charakteryzował się porowatością rzędu 55%. Powierzchnie stopów Ti23Mo otrzymanych różnymi metodami konsolidacji przedstawiono na **Rysunku 4** (Rysunek 2 [2])

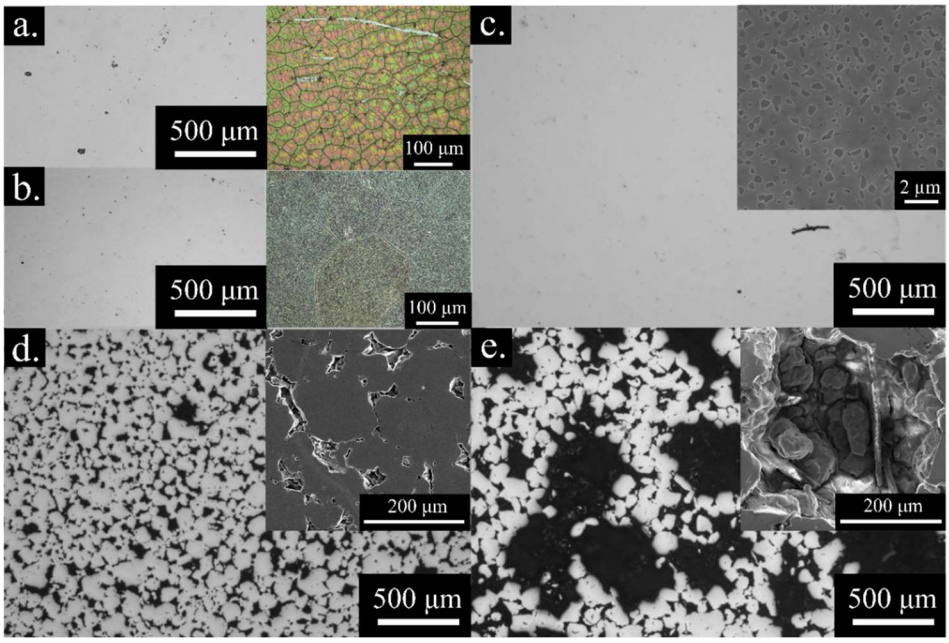

Rysunek 4. Powierzchnia stopówTi23Po otrzymanych różnymi metodami otrzymywania: topionie łukowe (a), i wyżarzanie w temperaturze 800ºC/24 h (b), mechaniczna synteza przez 48 h oraz: prasowanie na gorąco w 800ºC/5 min (c), prasowanie na zimno i spiekanie w 800°C/0,5 h (d) i prasowanie na zimno z NH_4HCO_3 i spiekanie w 1150ºC/10 h [2]

Dla wszystkich stopów Ti-Mo prasowanych na zimno oraz spiekanych w temperaturze 800ºC, a także prasowanych indukcyjnie na gorąco wyznaczono moduły Younga metodą nanoindentacji. Lite materiały charakteryzowały się modułami rzędu 124-140 GPa w zależności od zawartości molibdenu (10-31 at. %). Dla stopu wielofazowego Ti35Mo moduł Younga był znacząco wyższy (158 GPa). Natomiast stopy Ti-Mo spiekane w dwuetapowym procesie wykazywały znacznie mniejszą sztywność, co wynikało z ich dużej porowatości (Rysunek 9 [1], Tabela 5 [1]) . Najniższy moduł Younga wynosił ok. 55 GPa dla stopu Ti31Mo przy porowatości ok. 29%. Dla stopów Ti23Mo przeanalizowano także wpływ metody otrzymywania. Najniższą wartością 69,5 GPa charakteryzował się materiał o porowatości 55%, a najwyższą uzyskano w przypadku stopu topionego łukowo i wyżarzanego - 143 GPa (Rysunek 4 [2], Tabela 3 [2]). Prawie wszystkie stopy otrzymane w procesach metalurgii proszków charakteryzowały się modułami niższymi niż komercyjny tytan Grade 2 (141 GPa), natomiast mikrotwardość badanych stopów była znacznie wyższa od mikrokrystalicznego tytanu (180 $HV_{0,3}$). Dla stopów litych typu Ti(β) wynosiła 454-494 $HV_{0,3}$. Stopy pseudo β po spiekaniu swobodnym charakteryzowały się zbliżonymi wartościami w zakresie 337-366 $HV_{0,3}$. Mikrotwardość materiałów wykazywała zróżnicowany rozkład, który był związany ze zmianami mikrostrukturalnymi. **Tabela 1** przedstawia stopień porowatości, wartości modułów Younga oraz mikrotwardości Vickersa dla wybranych stopów.

Tabela 1. Porowatość (P), mikrotwardość Vickersa ($HVo_{,3}$) i moduły Younga (E) dla stopów Ti-Mo [1,2]

stop	Metoda otrzymywania	P [%]	$HV_{0,3}$	E [GPa]
Ti23Mo	topienie łukowe	0,31±0,06	547±7	141,2±2,6
	topienie łukowe i wyżarzanie	0,06±0,01	366±6	142,8±4,3
	prasowanie na gorąco	0,24±0,08	454±6	127,3±1,2
	prasowanie na zimno i spiekanie	24,64±0,45	366±19	104,9±10,5
	prasowanie na zimno i spiekanie z NH_4HCO_3	54,47±0,67	397±17	69,5±8,9
Ti31Mo	prasowanie na gorąco	0,21±0,02	494±8	136,8±1,8
	prasowanie na zimno i spiekanie	28,70±0,19	337±14	54,8±16,7

Porowatość stopów wpływa nie tylko na ich właściwości mechaniczne, ale także odgrywa istotną rolę w zachowaniu korozyjnym. Przeanalizowano odporność korozyjną stopów Ti23Mo w roztworze Ringera. (Rysunek 5 [2], Tabela 4 [2]). Uzyskane wyniki wykazują najlepszą odporność dla materiałów prasowanych na gorąco oraz topionych łukowo po obróbce cieplnej. Ponadto podatność na procesy korozyjne analizowanych stopów zależy od ich składu fazowego. Materiały jednofazowe charakteryzują się lepszymi właściwościami w porównaniu do dwufazowych. Wyniki testów zanurzeniowych potwierdziły, że ubytek masy zależy od struktury i porowatości stopu.

Przeprowadzono analizę właściwości powierzchniowych otrzymanych stopów wykonując pomiary kąta zwilżalności wybranych materiałów. Badane stopy Ti23Mo otrzymane różnymi metodami, a także stop Ti31Mo są materiałami hydrofilowymi. Kąty zwilżalności miały wartość mniejszą niż 90º dla cieczy pomiarowych: dijodometanu oraz gliceryny. Metodą OWRK (Owens, Wendt, Rabel oraz Kaelble) wyznaczono swobodną energię powierzchniową, której wartość dla stopów Ti23Mo była zawarta w zakresie 35-56 mN/m, natomiast dla stopu Ti31Mo wynosiła 43 mN/m (Tabela 6 [2], Tabela 10 [3]).

3.2.Kompozyty na bazie stopu Ti31Mo

W celu poprawy właściwości stopu Ti31Mo wytworzono układy kompozytowe zawierające 2,5-10 wag. % hydroksyapatytu oraz dodatki antybakteryjne: 1 wag. % Ag, 2 wag. % Ta_2O_5 lub CeO_2 [3]. Konsolidację proszków po 39 h mechanicznej syntezy przeprowadzono analogicznie do stopów prasowanych na zimno pod ciśnieniem 600 MPa i spiekanych w temperaturze 800ºC przez 30 min.

Dla wszystkich koncentracji hydroksyapatytu w kompozytach na bazie stopu Ti31Mo przeprowadzono analizę zmiany struktury krystalicznej podczas procesu mechanicznej syntezy (39 h). Po 15 min trwania mielenia dla wszystkich układów, w przeciwieństwie do stopu Ti31Mo, pojawiły się linie charakterystyczne dla fazy Ti(β), poza współistniejącą fazą Ti(α). Dodatkowo dla Ti31Mo10HA widoczne były refleksy pochodzące od hydroksyapatytu. Po 39 h tylko dla koncentracji 2,5 wag. % HA otrzymano materiał jednofazowy Ti(β). Dla pozostałych kompozytów proszek miał strukturę dwufazową Ti(α)+Ti(β). Dla żadnej koncentracji hydroksyapatytu nie zaobserwowano obecności fazy TiMo, jak w przypadku stopu Ti31Mo (Rysunek 1 [3]). Wielkość krystalitów wyznaczona metodą Williamsona-Halla wynosiła 9-27 nm (Rysunek 2, Tabela 1 [3].

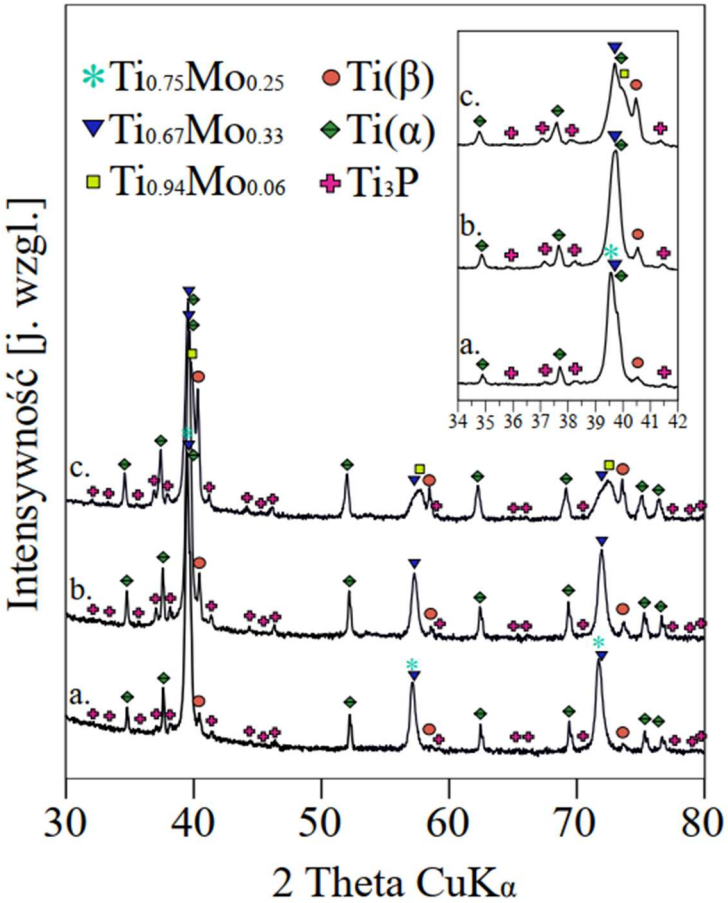

Rysunek 5. Dyfraktogramy rentgenowskie kompozytów Ti31MoxHA, x: 2,5 (a), 5 (b) i 10(c) prasowanych na zimno i spiekanych w temperaturze 800°C [3]

W wyniku konsolidacji proszków otrzymanych w procesie mechanicznej syntezy otrzymano materiały wielofazowe. Analiza strukturalna wykazała, że we wszystkich kompozytach występowały fazy typu β. Ich udział objętościowy malał wraz ze wzrostem

zawartości hydroksyapatytu z 70,3% do 57,5%. Udział 10 wag. % bioceramiki spowodował powstawanie regularnej fazy tytanowej (bcc) $Ti_{0,94}Mo_{0,06}$ oraz wzrost udziału fazy Ti(β) do 10%. Natomiast w kompozycie Ti31Mo2,5HA dominowała regularna faza (bcc) $Ti_{0,75}Mo_{0,25}$. We wszystkich kompozytach występowała również faza przejściowa $Ti_{0,67}Mo_{0,33}$ o strukturze regularnie przestrzennie centrowanej (bcc) oraz Ti_3P o strukturze heksagonalnej pochodząca z rozkładu hydroksyapatytu. Ponadto tlen dyfundujący do sieci osnowy stabilizował fazę Ti(α) powodując wzrost jej ilości z 18% (Ti31Mo2,5HA) do 29% (Ti31Mo10HA). Na **Rysunku 5** przedstawiono widma rentgenowskie kompozytów Ti31MoxHA (Rysunek 3 [3]). Udziały fazowe oraz parametry sieci krystalograficznych badanych kompozytów określono metodą Rietvelda (Tabela 2 [3]). Obserwacje mikroskopowe powierzchni kompozytów Ti31MoxHA z uwzględnieniem rozkładu poszczególnych pierwiastków potwierdziły otrzymanie struktury wielofazowej oraz ultradrobnoziarnistej struktury (ok. 1 μm) (Rysunek 4 [3]).

Przeanalizowano także wpływ dodatków antybakteryjnych 1 wag. % Ag, 2 wag. % Ta_2O_5 lub CeO_2 na strukturę kompozytu Ti31Mo5HA (Rysunek 5 [3]). Wprowadzenie do układu srebra lub tlenków bakteriobójczych spowodowało zmianę relacji między fazami typu β. W otrzymanych materiałach dominuje faza $Ti_{0,75}Mo_{0,25}$, która nie występowała w kompozycie Ti31Mo5HA. Natomiast ilość dominującej dla niego fazy $Ti_{0,67}Mo_{0,33}$ zmalała z ok. 57% do 9-19% w zależności od wprowadzonego dodatku antybakteryjnego. Wzrósł także udział objętościowy fazy Ti(β). Łączna ilość faz $Ti_{0,67}Mo_{0,33}$, $Ti_{0,75}Mo_{0,25}$ i Ti(β) wynosiła 65,4, 54,6 i 74,5% odpowiednio dla kompozytów o zawartości 1 wag. % Ag, 2 wag. % Ta_2O_5 i 2 wag. % CeO_2. Zawartość fazy Ti(α) dla wszystkich materiałów, niezależnie od wprowadzonego dodatku antybakteryjnego, wynosiła około 21%. We wszystkich kompozytach występowała także faza Ti_3P, oraz Ti_4P_3 dla kompozytu zawierającego tlenek ceru (IV) (Tabela 4 [3]).

Kompozyty Ti31MoxHA oraz Ti31Mo5HA-Ag (Ta_2O_5 lub CeO_2) charakteryzowały się znacznie mniejszą porowatością (2-8%) w stosunku do stopu Ti31Mo (29%) (Tabela 3, 5 [3]). Moduły Younga dla otrzymanych materiałów wielofazowych wynosiły od ok. 95 GPa do ok. 116 GPa (Rysuenk 7, 8 [3]). Najniższą wartość ok. 95 GPa uzyskano dla kompozytów Ti31Mo5HA1Ag i Ti31Mo5HA2CeO_2 przy porowatości ok. 4% oraz najniższych twardościach wynoszących odpowiednio 253 i 315 $HV_{0,3}$. W **Tabeli 2** (Tabela 6, 7 [3]) zestawiono stopień porowatości, wartości modułów Younga oraz mikrotwardości Vickersa dla analizowanych kompozytów.

Tabela 2. Porowatość (P), mikrotwardość Vickersa ($HVo_{,3}$) i moduły Younga (E) kompozytów [1, 3]

materiał	P [%]	$HV_{0,3}$	E [GPa]
Ti31Mo	28,70±0,19	377±14	54,80±16,68
Ti31Mo2,5HA	2,10±0,10	396±24	115,83±11,71
Ti31Mo5HA	3,72±0,27	347±30	100,91±13,19
Ti31Mo10HA	7,45±0,15	363±25	101,69±13,01
Ti31Mo5HA1Ag	3,83±0,54	253±11	94,94±6,64
Ti31Mo5HA2Ta_2O_5	4,97±0,39	379±29	102,45±30,00
Ti31Mo5HACeO_2	4,02±0,87	315±10	95,06±19,38

Ultradrobnoziarnisty kompozyt Ti31Mo5HA charakteryzował się znacznie lepszą odpornością korozyjną w roztworze Ringera niż stop Ti31Mo oraz kompozyty z zawartością 2,5 i 10 wag. % hydroksyapatytu. Dodatek 5 wag % hydroksyapatytu spowodował znaczące obniżenie prądu korozyjnego do 3,332 $\mu A \cdot cm^{-2}$ oraz wzrost wartości potencjału korozyjnego do −0,562 V. Wprowadzenie dodatków antybakteryjnych do kompozytu Ti31Mo5HA, szczególnie tlenku ceru (IV), pogorszyło jego odporność korozyjną (Rysunek 9-10, Tabela 8-9 [3]).

Analiza właściwości powierzchniowych wszystkich kompozytów potwierdziła ich hydrofilowy charakter. Kąty zwilżalności dla cieczy pomiarowych miały wartość mniejszą niż 90º. Swobodna energia powierzchniowa wynosiła od 43 mN/m dla kompozytu Ti31Mo5HA do 49 mN/m dla Ti31Mo10HA (Tabela 10 [3]). Najniższą energią 42 mN/m charakteryzował się materiał zawierający 2 wag. % Ta_2O_5 (Tabela 11 [3]).

3.3.Modyfikacja powierzchni

3.3.1. Modyfikacja powierzchni stopu Ti23Mo

Stop Ti23Mo prasowany na zimno i spiekany w temperaturze 800ºC przez 30 min poddano dwuetapowej modyfikacji powierzchni. Proces utleniania przeprowadzono metodą MAO przy stałym napięciu 250 V vs. potencjału obwodu otwartego (ang. *open circuit potential* OCP) przez 3 min w roztworze 0,01 M fosforanu wapnia $Ca_3(PO_4)_2$ i 0,5 M kwasu cytrynowego. W drugim etapie cząstki fluoroapatytu, otrzymane metodą hydrotermalną, osadzano na utlenionym podłożu poprzez nanoszenie elektroforetyczne przy napięciu wynoszącym -200 V przez 1 min w zawiesinie fluoroapatytu w etalolu [2].

W wyniku zastosowania procesu MAO powierzchnia stopu Ti23Mo charakteryzowała się wysokim rozwinięciem. Analiza rentgenowska wykazała, że utleniona warstwa wierzchnia składała się z tlenków ($T_{i6}O$, $CaTiO_3$), wodorotlenku wapnia ($Ca(OH)_2$) oraz apatytu ($Ca_3(PO_4)_2$). Morfologia powierzchni po procesie MAO ułatwia zakotwiczenie osadzanych cząsteki zwiększa adhezję powłoki do podłoża. Badania strukturalne potwierdziły otrzymanie powłoki floroapatytu (Rysunek 6 [2]) charakteryzującej się rozwiniętą topografią i porowatością, ułatwiającą proces osteointegracji. Na **Rysunku 6** (Rysunek 7 [2]) przedstawiono morfologię powierzchni stopu Ti23Mo po kolejnych etapach modyfikacji powierzchni.

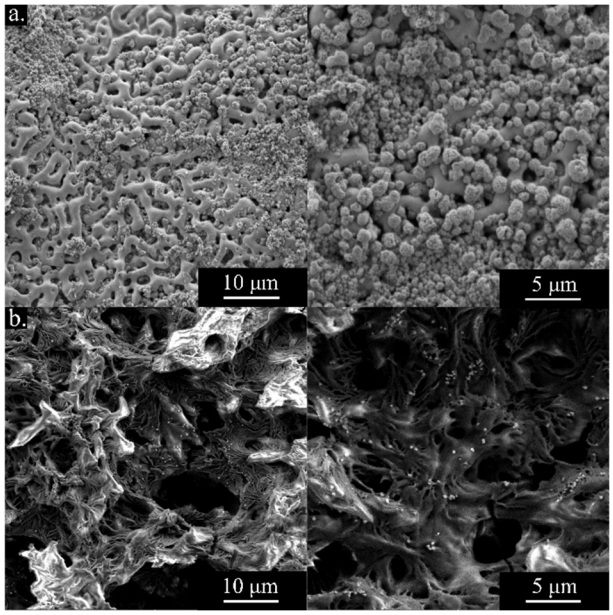

Rysunek 6. Powierzchnia stopu Ti23Mo po utlenianiu MAO (a) i osadzaniu elektroforetycznym fluoroapatytu (b) [2]

Obróbka powierzchniowa stopu Ti23Mo prasowanego na zimno i spiekanego swobodnie spowodowała poprawę odporności korozyjnej w roztworze Ringera (Rysunek 8 [2], Tabela [5]). Najlepszą odporność korozyjną dla analizowanego stopu uzyskano po procesie MAO. Jednak była ona gorsza od stopów litych otrzymanych w procesach prasowania na gorąco, czy topienia łukowego.

W efekcie modyfikacji powierzchni stopu Ti23Mo kąty zwilżalności wzrosły, szczególnie dla utlenionej powierzchni. Jednak ich wartości dla dwóch cieczy pomiarowych nie przekraczały 90º, co oznaczało zachowanie hydrofilorego charakteru. Swobodna energia powierzchniowa po osadzeniu fluoroapatytu zmalała z 56 mN/m do 49 mN/m. Najniższą wartość ok. 43 mN/m uzyskano dla powierzchni po procesie utleniania (Tabla 6 [2]).

3.3.2. Modyfikacja powierzchni stopu Ti31Mo

Zastosowano procesy modyfikacji powierzchni dla stopu Ti31Mo otrzymanego w procesie prasowania na zimno i spiekania w temperaturze 800ºC. W pierwszym etapie biomateriały zanurzono w 5 M roztworze NaOH na 24 godziny w temperaturze 60°C. W drugim kroku na powierzchni osadzono powłokę Ca/P metodą hydrotermalną. Zastosowano elektrolit 1 M NaOH z 0,25 M $CaNa_2$-EDTA oraz 0,25 M K_2HPO_4. Proces przeprowadzono w temperaturze 120°C przez 2 h [4].

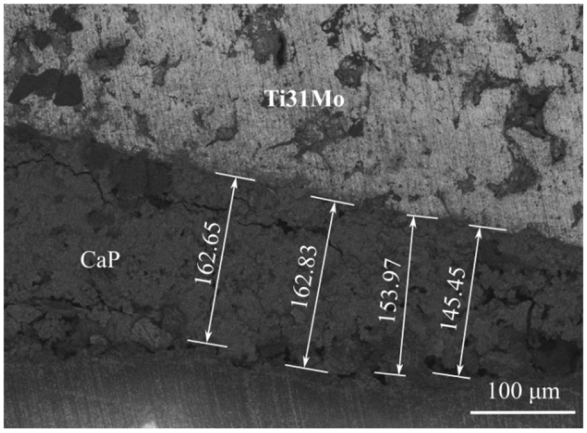

Rysunek 7. Przekrój poprzeczny warstwy CaP na stopie Ti31Mo [4]

Zanurzenie jednofazowego stopu Ti31Mo w roztworze NaOH spowodowało utlenienie oraz rozwinięcie powierzchni stopu, co ułatwiło osadzanie i kotwiczenie powłoki w kolejnym etapie obróbki powierzchniowej. Otrzymana powłoka o grubości ok. 155 µm składała się głównie z hydroksyapatytu $Ca_{10}(PO_4)_6(OH)_2$ oraz 19% wodorofosforanu wapnia $CaHPO_4 \cdot 2H_2O$ (Rysunek 2 [4], Tabela 1 [4]). Przekrój poprzeczny powłoki zaprezentowano na **Rysunku 7** (Rysunek 4 [4]). Analiza EDS potwierdziła obecność jonów wapnia i fosforu po zastosowanej obróbce hydrotermalnej oraz ich równomierny rozkład (Rysuenk 5 [4], Tabela [2]).

Znaczne rozwinięcie powierzchni po procesie utleniania oraz osadzania powłoki Ca/P potwierdziły badania chropowatości. Dla stopu Ti31Mo parametry Ra, Rt i Rz wynosiły odpowiednio około 1, 15 i 11 µm. Natomiast po zanurzeniu w roztworze NaOH wzrosły do wartości 2, 22 i 16 µm. Po obróbce hydrotermalnej wartości parametrów chropowatości były najwyższe: Ra ≈9 µm, Rt ≈ 62 µm, i Rz ≈ 45 µm (Rysunek 6 [4], Tabela 3 [4]).

Zastosowana obróbka powierzchniowa dla stopu Ti31Mo spowodowała poprawę jego odporności korozyjnej oraz hydrofilowości . Ubytek masy po 14 dniach zanurzenia w roztworze Ringera spadł z 49,6 µg/dzień dla stopu przed modyfikacją powierzchni do 15 µg/dzień

dla stopu po obróbce hydrotermalnej. Jednak najlepszą odpornością korozyjną charakteryzował się kompozyt Ti31Mo5HA, dla którego ubytek masy wynosił zaledwie 3 µg/dzień. Dla innych zawartości hydroksyapatytu (2,5 i 10 wag. %) odporność korozyjna była zbliżona lub gorsza w porównaniu do stopu modyfikowanego powierzchniowo. Kąty zwilżalności powierzchni dla gliceryny po obróbce powierzchniowej odpowiednio zmniejszyły się z ok. 50º do 31º (Tabela 4 [4]).

3.4.Badania aktywności przeciwbakteryjnej i biozgodności

3.4.1. Badania aktywności przeciwbakteryjnej

Przeprowadzono ocenę aktywności antybakteryjnej dla stopu Ti31Mo oraz kompozytów Ti31Mo5HA, Ti31Mo5HA-Ag (Ta_2O_5 lub CeO_2) względem szczepu bakterii *Staphylococcus aureus* (ATCC 6538) [3].

W porównaniu do mikrokrystalicznego tytanu na powierzchni kompozytów zawierających dodatki antybakteryjne, takie jak srebro czy tlenek ceru (IV) adhezja bakterii była znacząco mniejsza. Kompozyty Ti31Mo5HA1Ag i Ti31Mo5HA2CeO_2 hamowały tworzenie biofilmu. Współczynnik redukcji (ang. *reduction factor* RF), który został odniesiony do liczby jednostek tworzących kolonie bakteryjne na mikrokrystalicznym tytanie, wynosił odpowiednio 97,5 oraz 98,9% (**Tabela 3**, Tabela 12 [3]). Wysoka aktywność przeciwbakteryjną tych kompozytów wobec *S. aureus* widoczna jest także na zdjęciach przedstawiających hodowle bakteryjne po 24 h inkubacji (Rysunek 11 [3]).

Tabela 3, Aktywność antybakteryjna materiałów względem S. aurerus [3]

materiał	**CFU/mL**		**RF %**
	Po 4 h inkubacji	**Po 20 h inkubacji**	
Tytan mikrokrystaliczny (kontrolny)	$<1{,}0\cdot10^3$	$2{,}0\cdot10^5$	-
Ti31Mo	$<1{,}0\cdot10^3$	$3{,}5\cdot10^4$	82,5
Ti31Mo5HA	$<1{,}0\cdot10^3$	$4{,}0\cdot10^4$	80,0
Ti31Mo5HA1Ag	$<1{,}0\cdot10^3$	$5{,}0\cdot10^3$	97,5
Ti31Mo5HA2Ta_2O_5	$<1{,}0\cdot10^3$	$3{,}5\cdot10^4$	82,5
Ti31Mo5HA2CeO_2	$<1{,}0\cdot10^3$	$2{,}2\cdot10^3$	98,9

3.4.2. Badania biozgodności

Zbadano intensywność wzrostu komórek kostnych na powierzchniach stopu Ti31Mo, Ti31Mo modyfikowanego powierzchniowo oraz kompozytów Ti31Mo5HA, Ti31Mo5HA-Ag (Ta_2O_5 lub CeO_2), Do badań *in vitro* wykorzystano linię komórkową Normalnych Ludzkich Osteoblastów (NHost, CC-2538) i Ludzkich Fibroblastów Więzadła Przyzębia (HPdLF, CC-7049), które hodowano na badanych materiałach przez 24, 72 i 120 h [4],

Topografia powierzchni i skład chemiczny biomateriału wpływały na intensywność wzrostu komórek kostnych, Komórki NHost i HPdLF wykazywały bardzo dobrą proliferację, kolonizację i wielowarstwowość, Po 72 h hodowli względna żywotność fibroblastów względem tytanu mikrokrystalicznego (ang, *Relative Viability of the Cells* RVC) dla wszystkich badanych materiałów była wyższa od 100%, Proliferacja osteoblastów dla kompozytów Ti31Mo5HA, Ti31Mo5HA-Ag (Ta_2O_5 lub CeO_2) oraz stopu Ti31Mo modyfikowanego powierzchniowo po 120 h hodowli była intensywniejsza lub zbliżona, tak jak w przypadku fibroblastów, do tytanu mikrokrystalicznego [**Rysunek 8,** Rysunek 9, 10 [4]),

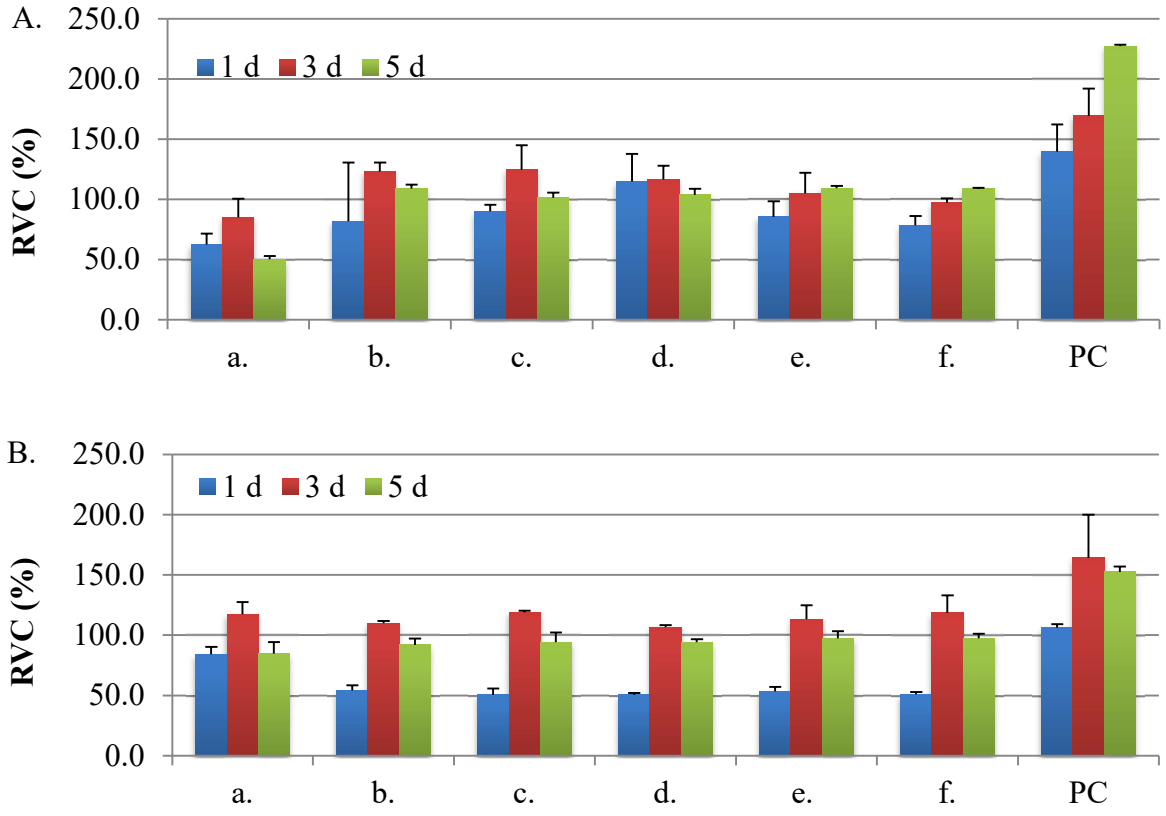

Rysunek 8, Wyniki testu MTS po 1, 3 i 4 dobach dotyczących żywotności komórek NHost (A) i HPdLF (B) dla stopu Ti31Mo (a), Ti31Mo po obróbce hydrotermalnej (b), kompozytu Ti31Mo5HA (c), Ti31Mo5HA1Ag (d), Ti31Mo5HA2CeO_2 (e), Ti31Mo5HA2Ta_2O_5 (f), kontroli pozytywnej (PC)

4. Artykuły wchodzące w skład monotematycznego cyklu publikacji

[1] **P, Sochacka**, A, Miklaszewski, M, Jurczyk, Development of β-type Ti-x at, % Mo alloys by mechanical alloying and powder metallurgy: phase evolution and mechanical properties (10≤x≤35), J, Alloys Compd, 776 (2019) 370-378, doi,org/10,1016/j,jallcom,2018,10,217, **(IF 4,175; 100 pkt MNiSW)**

[2] **P, Sochacka**, A, Miklaszewski, K, Kowalski, M, Jurczyk, Influence of the Processing Method on the Properties of Ti-23 at,% Mo Alloy, Metals 9 (2019) 931, doi,org/10,3390/met9090931, **(IF 2,259; 70 pkt MNiSW)**

[3] **P, Sochacka**, A, Miklaszewski, M, Jurczyk, P, Pecyna, M, Ratajczak, M, Gajecka, M,U, Jurczyk, Effect of hydroxyapatite and Ag, Ta2O5 or CeO2 addition on the properties of ultrafine-grained Ti31Mo alloy, J, Alloys Compd 823 (2020) 153749, doi,org/10,1016/j,jallcom,2020,153749, **(IF 4,650; 100 pkt MNiSW)**

[4] **P, Sochacka**, M,U, Jurczyk, K, Kowalski, P,K, Wildstein, M, Jurczyk, Ultrafine-Grained Ti-31Mo-Type Composites with HA and Ag, Ta2O5 or CeO2 Addition for Implant Applications, Materials 14 (2021) 644, doi,org/10,3390/ma14030644, **(IF 3,057; 140 pkt MNiSW)**

5. Podsumowanie

W ramach realizowanych badań wytworzono dwuskładnikowe stopy na bazie tytanu zawierające molibden (10-35 at, %), Określono wpływ składu chemicznego, metody wytwarzania oraz modyfikacji powierzchni wybranych stopów na ich właściwości, Zestawione wyniki badań pozwoliły na sformułowanie następujących wniosków:

a. Głównymi parametrami kontrolującymi przemianę Ti(α)→Ti(β) w układach wytwarzanych metodami mechanicznej syntezy oraz metalurgii proszków są zawartość molibdenu oraz czas trwania procesu mechanicznej syntezy
b. W otrzymanych stopach Ti-Mo wraz ze wzrostem zawartości molibdenu oraz temperatury spiekania wzrasta udział fazy Ti(β)
c. W procesie indukcyjnego prasowania na gorąco otrzymano jednofazowe, lite stopy typu Ti(β) dla zawartości 23-31 at, % molibdenu z ultradrobnym ziarnem
d. Zawartość molibdenu oraz porowatość stopów wpływają na wartości modułów Younga (najniższa wartość 55 GPa przy porowatości 29% dla stopu Ti31Mo)
e. Metoda otrzymywania determinuje skład fazowy oraz porowatość otrzymanych materiałów, które wpływają na ich finalne właściwości mechaniczne i powierzchniowe

f. Modyfikacja składu chemicznego poprzez wprowadzenie do stopu Ti31Mo hydroksyapatytu oraz dodatków antybakteryjnych prowadzi do otrzymania materiałów wielofazowych, w których dominują fazy typu β
g. Wprowadzenie hydroksyapatytu oraz dodatków antybakeryjnych powoduje obniżenie modułów Younga (najniższa wartość ok, 95 GPa dla kompozytów Ti31Mo5HA1Ag i Ti31Mo5HA2CeO_2 przy porowatości ok, 4%)
h. kompozyty Ti31Mo5HA1Ag i Ti31Mo5HA2CeO_2 charakteryzują się znaczną aktywnością antybakteryjną względem szczepu bakterii *S, aureus*
i. Modyfikacja powierzchni stopów powoduje wzrost odporności korozyjnej stopów; w przypadku stopu Ti31Mo bardziej efektywną poprawę uzyskuję się przez modyfikację składu chemicznego wprowadzając 5 wag, % hydroksypapatytu do objętości materiału
j. Kompozyty Ti31Mo5HA, Ti31Mo5HA-Ag (Ta_2O_5 lub CeO_2) oraz stop Ti31Mo po modyfikacji powierzchniowej wykazują lepszą lub zbliżoną cytokompatybilność względem tytanu mikrokrystalicznego dla osteoblastów (NHost) i fibroblastów (HPdLF)

Publikacje

Artykuł nr 1:

P, Sochacka, A, Miklaszewski, M, Jurczyk,

Development of β-type Ti-x at, % Mo alloys by mechanical alloying and powder metallurgy: phase evolution and mechanical properties (10≤x≤35)

J, Alloys Compd, 776 (2019) 370-378

doi,org/10,1016/j,jallcom,2018,10,217

Journal of Alloys and Compounds 776 (2019) 370–378

Contents lists available at ScienceDirect

Journal of Alloys and Compounds

journal homepage: http://www.elsevier.com/locate/jalcom

Development of β-type Ti-x at. % Mo alloys by mechanical alloying and powder metallurgy: Phase evolution and mechanical properties ($10 \leq x \leq 35$)

P. Sochacka, A. Miklaszewski*, M. Jurczyk

Institute of Materials Science and Engineering, Poznan University of Technology, Jana Pawła II No 24, 61-138 Poznan, Poland

ARTICLE INFO

Article history:
Received 5 September 2018
Accepted 17 October 2018
Available online 21 October 2018

Keywords:
Metals and alloys
Mechanical alloying
Phase transitions
Powder metallurgy
X-ray diffraction
Elastic modulus

ABSTRACT

Titanium-based alloys with fine grain structure represent a class of engineering materials that can exhibit a unique combination of properties. This paper presents the structural evolution of the β phase in Ti-x at. % Mo (x = 10, 23, 27, 31 and 35) alloys synthesized by mechanical alloying with different milling times between 15 min and 48 h and powder metallurgical process with cold powder compaction and sintering or interchangeably hot pressing. The binary alloys were characterized by X-ray diffraction, scanning electron microscopy, chemical composition determination as well as density and porosity measurements. The influence of the chemical composition and method of processing on the final microstructure, and mechanical properties of bulk alloys were studied. The mechanically alloyed Ti23Mo, Ti27Mo and Ti31Mo materials upon sintering at 800 °C for 5 min led to the formation of single β type phase alloys. All these β-type alloys have elastic modulus lower than CP microcrystalline α-Ti, but their hardness is nearly 3 times higher (approx: 460 $HV_{0.3}$). The present study has demonstrated that these single phase β-type alloys with fine grain microstructure can be fabricated by the application of hot pressing of mechanically alloyed powders at the temperature below α→β transus (800 °C).

1. Introduction

Commercial purity titanium and Ti–6Al–4V alloy are the main materials in the medical applications [1–4]. However, they present important disadvantages such as high elastic modulus (E), relatively poor wear resistance, low hardness and in the case of Ti6Al4V alloy some toxicity due to the aluminium and vanadium contents [5,6]. Current research goals are: (i) to avoid potentially toxic elements to improve biocompatibility; (ii) to produce Ti-based alloys with a high fatigue strength. Above mentioned requirements partially fulfil β-titanium type alloys [1–4,7–12].

Alloying metals for Ti are arranged in three groups: i) α-stabilizers (C, N, O and Al), ii) neutral stabilizers (Zr) and iii) β-stabilizers: isomorphous (V, Nb, Mo, Ta) and eutectoid (Si, Cr, Mn, Fe, Co, Ni, W). For medical implant applications, Ti-based alloys with β-phase are desirable due to high fatigue resistance, low elastic modulus, high hardness and good corrosion resistance [2,5]. For example, till now Ti-Mo, Ti-Mo-Ta,Ti-5Al-5Mo-5V-3Cr, Ti-40Zr and Ti-5Al-13Ta alloys have been synthesized, and their properties studied [8,11,13,14].

Recently, many attempts were made to create low modulus β Ti biomaterials [12,13]. Molybdenum is less toxic than aluminium and vanadium. The solubility limits of alloying Mo metal in Ti is 8 wt% [15]. The phase constitutions, hardness and Young modulus are different for different contents of molybdenum in Ti–Mo system [13,14]. Latest research have shown that the addition of Mo form β-phase in Ti-base alloy, and finally increase the hardness, decrease the Young modulus as well as improve the corrosion resistance and the biocompatibility [16]. Zhang et al. synthesized a series of Ti–Mo alloys (3.2–12 at. %) with the application of arc melting process [13]. The phase constitutions and Young modulus are very sensitive to the Mo content. For example, Ti-3.2Mo and Ti-8Mo alloys contain only α and β phases and have low E modulus. On the other hand, Ti-4.5Mo, Ti-6Mo and Ti-7Mo biomaterials have a high E modulus due to some contents of ω phase in Ti-Mo alloys.

Additionally, Whang et al. studied the super elasticity and shape memory effect in water-quenched and air-cooled Ti-x Mo (x = 10, 11, 12 wt%) biomaterials [17]. The water-quenched alloys except the β phase contain the martensite α"phase and ω phase, but the air-

* Corresponding author.
E-mail address: andrzej.miklaszewski@put.poznan.pl (A. Miklaszewski).

https://doi.org/10.1016/j.jallcom.2018.10.217
0925-8388/

cooled alloys contain a large amount of ω phase. The increasing content of molybdenum decrease the amounts of α" and ω phases. Metastable materials are created from the nonequilibrium β (Im3*m*) phase retained during quenching [15]. The cph phase (α′, *P*6$_3$/*mmc*) can form martensitically in Ti-rich alloys. On the other hand, in alloys with slightly higher Mo content, an orthorhombic distortion of cph (α", *Cmcm*) is created. The ω (*P*6/*mmm*) phase is formed as an intermediate phase in the decomposition of metastable β to the equilibrium α (*P*6$_3$/*mmc*). At higher Mo concentrations, α′, α″, α″ +β + ω, β + ω and β phases can be observed after quenching from the β section.

The microstructure and grain growth kinetics of Ti–Mo alloys have been analysed, too [18]. The single phase β type materials were observed when Mo content increases to 10 wt % or higher. The plasticity and strength of these biomaterials increase with the increasing of Mo content and decreasing grain size. On the other hand, in the Ti–10, 20 and 30 Mo alloys (wt. %) α precipitates were detected in their β matrix [19]. Almeida et al. synthesized a series of Ti-Mo alloys (4–19 wt% Mo) by the application of laser alloying method [20]. For Mo concentration between 4 and 8 wt% 2-phase materials were produced (acicular martensite and β-phase) and alloys with Mo ≥ 10 wt% are β phase. For the Ti-13Mo alloy Young's modulus and hardness were 75 GPa and 240 VHN, respectively.

Ti–Mo alloys from 4 to 20 Mo wt. % were arc-melted [21]. The mixture of the hexagonal α′and orthorhombic α"phases were detected for the Ti-4Mo alloy, and the α"phase is visible for the concentration of Mo = 6 wt %. At higher concentrations of Mo (15 and 20 wt %) only β phase is observed. Electrochemical studies have indicated a good corrosion resistance in Ringer solution for all alloys.

The chemical composition and ageing heat treatments have a powerful influence on the microstructure, hardness and elastic modulus of Ti-Mo biomaterials [22]. The application of high cooling rate allows to produce the β phase biomaterials with the concentration of 10% of molybdenum. The phase composition has a strong influence on Young's modulus and the highest hardness was achieved by ageing at 450 °C, due to the precipitation of α and ω phases.

Generally, the mechanical performance and biocompatibility of Ti-based alloys can be improved by modification of its alloy composition and microstructure [23–29]. In the past years, application of materials with diminished grain scale has become very popular in implantology [23]. Improvement of the mechanical properties of Ti-type biomaterials can be achieved through microstructure control, the top-down approaches known as severe plastic deformation (SPD) and mechanical alloying (MA) [25–28,30–33]. These biomaterials exhibit an unusual combination of properties such as high strength, high fracture toughness, good corrosion resistance and good biocompatibility [23,27,31,34,35].

MA technique allows alloying elements that are difficult or impossible to combine by conventional melting methods [31,32]. Additionally, this process allows to improve material properties because of the nano-scale size objects formation and in some cases new phases creation. One of the examples could be hardness improvement due to the grain boundary strengthening mechanism. During the MA process the extreme grain refinement of the powdered metals down to nanoscale creates surface morphology that intensify growth and adhesion of living cells [35].

In this work the mechanical alloying with different milling times between 15 min and 45 h and powder metallurgical process with a cold powder compaction and sintering or interchangeably hot pressing (HP) was applied for the preparation of the β-type Ti-x at. % Mo (x = 10, 23, 27, 31 and 35) alloys. Structure, microstructure, composition, porosity and mechanical properties of bulk alloys were studied. Till now, no attention has been paid to the influence of Mo contents on the structure evolution in Ti-Mo alloys during mechanical alloying and its sintering at the different temperature regimes.

2. Materials and methods

2.1. Sample preparation

Mechanical alloying was performed at argon atmosphere by the application of SPEX 8000 Mixer Mill. Total milling time was 48 h. Powders of titanium (<45 μm, 99.9%, Alfa Aesar) and molybdenum (44 μm, 99.6%, Sigma Aldrich) were weighted, blended and poured into stainless steel vials in glove box (Labmaster 130). A weight ratio of hard steel balls to powder weight ratio equalled 10:1. In the next step, the produced powders were processed by powder metallurgy process by the application both cold and hot methods. In the cold method, the MA powders were placed into the matrix and uniaxially pressed at a pressure of 600 MPa. Finally, the green compacts were placed in argon filled quartz tubes and heated through 1 h to 600, 700, 800 and 1000 °C, and kept at high temperature for 30 min for sintering. The diameter and height of bulk samples were 8 mm and 4 mm, respectively. In the case of hot pressing, induction coil module was used for a conductive die heating which for the processing detailed were described in our previous work [36].

2.2. Materials characterization

For sample structure examination during different processing stages, a Panalytical Empyrean XRD equipment with CuKα radiation, λ = 1,54178 Å (Almelo, Netherlands) was used. For crystallite size and lattice strain estimation after mechanical alloying, the Williamson-Hall (W-H) method with assumed uniform deformation model (UDM) was used. Detailed description of crystallographic structure evaluation was included in our previous work [36].

The lattice parameter estimation and phase quantitative analysis was based on the Rietveld profile fitting realized on the Maud software. Apply approach involve the simulation of the diffraction pattern based on the analysed structural model for:

- Ti (α) (ref. code 01-071-4632),
- Ti (β) (ref. code 01-074-7075),
- Mo (ref. code 01-071-4645),
- MoTi (ref. code 01-071-9821).

The calculated pattern of the model structure was fitted to the observed spectra by minimization of the sum of the squares and after refinement using Levenberg-Marquardt least squares algorithm which achieves high goodness of fit ($\chi^2 < 2.5$). For clearance, residual pattern indicators of modelled data as:

- R_{wp} – weighted pattern residual indicator,
- R_{exp}– expected residual indicator,
- χ – goodness of fit were revealed.

For microstructural analysis, the samples were polished and next etched in Kroll reagent for a 50 min.

Scanning electron microscope (SEM, VEGA Tescan, Brno, Czech Republic) with energy dispersive spectrometer (EDS, PTG Prison Avalon, Princeton Gamma Tech. Princeton, NY, USA) was used to characterize the microstructure and chemical composition of the prepared sinters. For a high-resolution microstructure and crystallographic pattern analysis high-resolution transmission electron

microscope HITACHI HD-2300A was used.

For the obtained sinters porosity was evaluated. The calculation was based on the formula $P = (1 - \rho/\rho_{th}) \times 100\%$, where ρ and ρ_{th} are the density of the porous material and its corresponding theoretical density calculated from the rule of the mixtures, respectively. The density of the obtained sinters was determined by the Archimedes method.

Indentation Hardness (HV) and Young modulus (EIT) of the non-etched Ti-Mo alloys, was evaluated using a CSM Instruments nanoindenter with the Berkovich diamond tip [37] based on the Oliver and Pharr [38] approach and ISO 14577 standard for measurements. Detailed description of data evaluation was included in our previous work [27].

Additionally, the Vickers microhardness of the sinters was measured using a microhardness tester by applying a load of 300 g for 10 s on the polished surfaces of the samples. For each sample, 10 separate indents were created on the investigated surface.

3. Results and discussion

3.1. Mechanical alloying stage

The goal of our research was the synthesis of β type Ti-x at. % Mo (x = 10, 23, 27, 31 and 35) alloy powders by mechanical alloying. The crystal structure change during milling process was studied. Fig. 1 shows XRD patterns of MA materials in function of milling time. For x > 10 in Ti-x at. % Mo, the characteristic (hkl) lines of Ti and Mo are only visible after 15 min of MA, but after 5 h of MA the (110) plane from cubic Mo crystal structure disappeared, and new MoTi phase is formed. Additionally, after 15 h new phase Ti(β) (110) was detected. As it could be seen during synthesis, cold welding and alloying of substrates proceeds at the solid state. In the case of Ti-10 at. % Mo composition, the reflexes characteristic for TiMo phase is visible after 15 min of MA and any trace of Ti(β) phase is observed even after 48 h of MA.

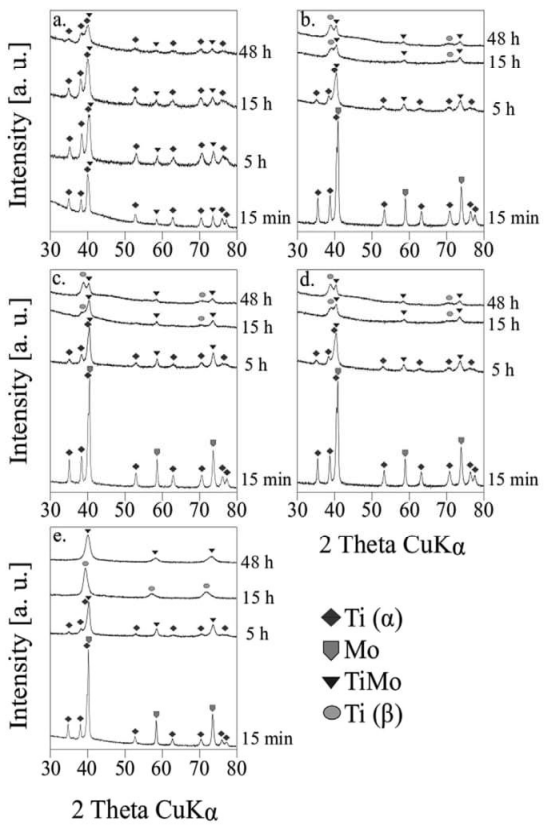

Fig. 1. XRD spectra of Ti-x at. % Mo powders mechanically alloyed for different times (15 min, 5 h, 15 h and 48 h): a) 10 at. %, b) 23 at. %, c) 27 at. %, d) 31 at. % and e) 35 at. %.

High energy transfer to the substrate powders during MA result in a high density of defects and dislocation. After 48 h of mechanical alloying the powders are almost amorphous and the crystallite sizes calculated by the application of W-H (UDM) approach were 5.5, 13.5, 16, 18 and 19 nm for 10, 23, 27, 31 and 35 at. % of Mo content in Ti-Mo alloy, respectively (Table 1). During the MA process the phase transition from Ti(α) to Ti(β) is observed for x > 10 in Ti-x at. % Mo. In the case of Ti35Mo, single β phase material was obtained after 15 h of MA. Longer milling time (48 h) has created the Mo-Ti phase, only (see Fig. 1). The molybdenum content and milling time are the main parameters which control this transformation.

The particle size and strain values evaluated by the Williamson–Hall approach from the plots slope and intercept depictured on Fig. 2 of TiMo samples after 48 h of MA, where gathered in Table 1. In the case of Ti-10 at. % Mo alloy a negative slope indicates compressive strain experienced by the particles. For growing in a starting powders (from 23 to 35 at. %) molybdenum content, calculated values of strain and crystallite size shows coincident relation. Above structural response stays firmly connected with obtained phase composition and its respective contributions. The material phase transformation fallowed in cold welding and fracturing stadium of powder processing shows different reliance for different starting substrate powders compositions.

Fig. 3 shows the SEM microphotographs of starting powders (Ti and Mo) and Ti27Mo agglomerates obtained after 48 h of MA. Presented microphotographs confirm continuing cold welding and fracturing stadium of starting substrate powders noticeable by the particle size scattering and agglomerate structure. Most of the agglomerated rounded particles have a size which varies from 50 to 150 μm.

3.2. Bulk alloy stage

All mechanically alloyed powder compositions were finally cold pressed and sintered at temperatures of 600, 700, 800 and 1000 °C for 0.5 h at argon atmosphere and also hot pressed in 800 °C in vacuum conditions. Fig. 4 shows XRD spectra of synthesized bulk alloys. The sintering at temperatures of 600, 700, 800 and 1000 °C results in bulk materials formation. Additionally to the main Ti(β) phase; Ti(α) and MoTi phases could also be observed. It is important to note that except the value of the sintering temperature, the amount of molybdenum in the Ti-Mo system is sensitive on the final phases content of so produced bulk materials what also earlier

Table 1
Structure size and strain factors determined by the Williamson-Hall method based on XRD spectra of Ti-x at. % Mo powders after 48 h of MA.

alloys	D [nm]	ε –
Ti-10 at. % Mo	5.48	$-3.93 \cdot 10^{-3}$
Ti-23 at. % Mo	13.46	$5.60 \cdot 10^{-3}$
Ti-27 at. % Mo	15.94	$5.60 \cdot 10^{-3}$
Ti-31 at. % Mo	18.01	$7.88 \cdot 10^{-3}$
Ti-35 at. % Mo	18.74	$8.25 \cdot 10^{-3}$

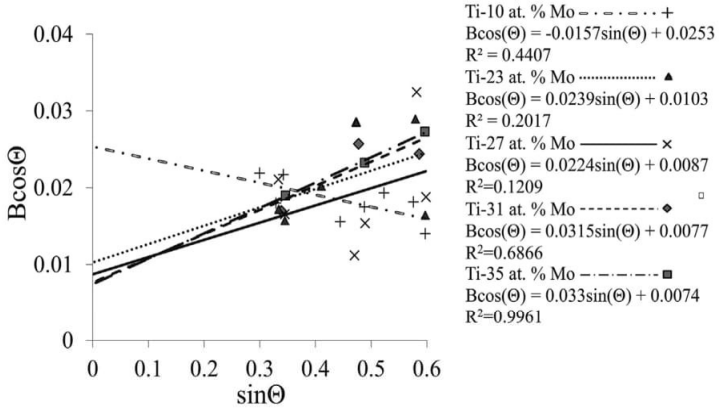

Fig. 2. Linear Williamson-Hall plots based on the XRD spectra of studies Ti-x at. % Mo powder materials after 48 h of mechanical alloying.

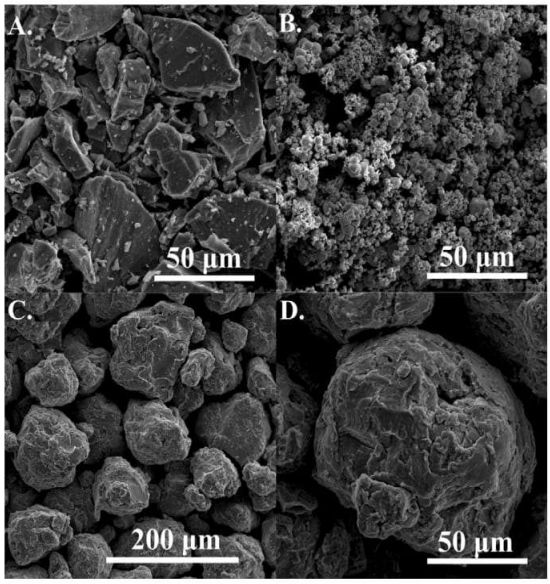

Fig. 3. SEM micrographs of titanium (a), molybdenum (b) and Ti-27 at. % Mo powders after 48 h of MA (c, d).

research confirms [39]. The most intense peaks on all patterns are related to Ti(β) phase. No single phase β-type Ti-Mo alloys were produced during cold pressing and sintered approach in the temperatures range between 600 and 1000 °C. The content of Ti(α) phase in the all synthesized TiMo alloys is decreasing with increasing sintering temperature (see Table 2). For example in Ti27Mo alloy, the content of the main Ti(β) phase was increased from 88.90 to 97.61% if sintering temperature increase from 600 to 1000 °C. In bulk alloys with $x \geq 23$ at. % Mo sintered at 600 °C a small content of MoTi phase is detected. In the case of Ti35Mo alloy, three phases are visible in all analysed sintering temperature regimes: Ti(β), Ti(α) and MoTi. Additional TiMo cubic phase preserved from the powder stage based on molybdenum, as presented data shows, stays as a source of Mo for Ti(β) phase due to its decomposition. Growing molybdenum content influence as Fig. 4 and Table 2 confirmed, the additional cubic TiMo phase appearance, that volumetric amount could be shaped by a proper sintering temperature treatment.

On the other hand, the Ti-x Mo alloys produced by the application of hot pressing at 800 °C in vacuum approach, allow to form the single β phase bulk materials, formed for x = 23, 27 and 31 at. % (Table 2). For the Ti10Mo and Ti35Mo compositions, additionally to the main Ti(β) phase, the second Ti(α′) and MoTi phases are detected and its contents determined by Rietveld analysis were 26.75 and 16.01% for x = 10 and 35 at. %, respectively. The hexagonal martensitic Ti(α′) phase appearance for the lowest analysed molybdenum content Ti10Mo, also observed in other works [40,41], evidence stable transformation. For the highest Ti35Mo composition additional TiMo phase appearance translate to preserved after MA phase that full decomposition do not take place. The structural parameters of synthesized bulk TiMo alloys are summarized in Table 3.

Hot pressing method allows to synthesize bulk TiMo alloys with very low porosities (Table 4). On the other hand, the bulk TiMo samples produced by cold pressing and sintering at different temperatures for 0.5 h, were composed of irregular particles and show porous microstructure (Fig. 5). Porosity depends strongly on the chemical composition of synthesized alloys (Table 4). The application of HP method can obtain single beta phase type materials for Ti23Mo, Ti27Mo and Ti31Mo. The smooth bulk Ti27Mo alloy surface was also presented in Fig. 6 with their EDS analysis and elements mapping (Fig. 6 b, c, d), for example. The obtained results confirmed the chemical composition of HP sample with its uniform distribution. The presence of small amount of iron atoms (0.24 at. %) in the synthesized Ti27Mo alloys could be explained by Fe impurities trapped in the MA powders from erosion of the milling media.

The microstructure analysis was conduct to confirm in obtained sinters, formed grain size scale structure. BSE view of HP samples presented in Fig. 7, shows independently phase contrast relation and microstructure size range. As it could be observed from the analysis, the etching agent reaction characterize different surface reaction due to starting compositional change. For the lowest analysed molybdenum content Ti10Mo sample, the microstructure consists of Ti(β) and Ti(α′) phases also confirmed structurally, which for the martensitic phase mostly place the boundary position. As for the single cubic Ti(β) phase Ti23Mo, Ti27Mo samples the etching agent shows a deep subsurface infiltration confirming simultaneously uniform grain size distribution in view. For a higher molybdenum content Ti31Mo and Ti35Mo, the etching agent reaction manifests by a weaker grain boundary and porosity impingement which for alone Ti(β), or Ti(β) and TiMo phase could

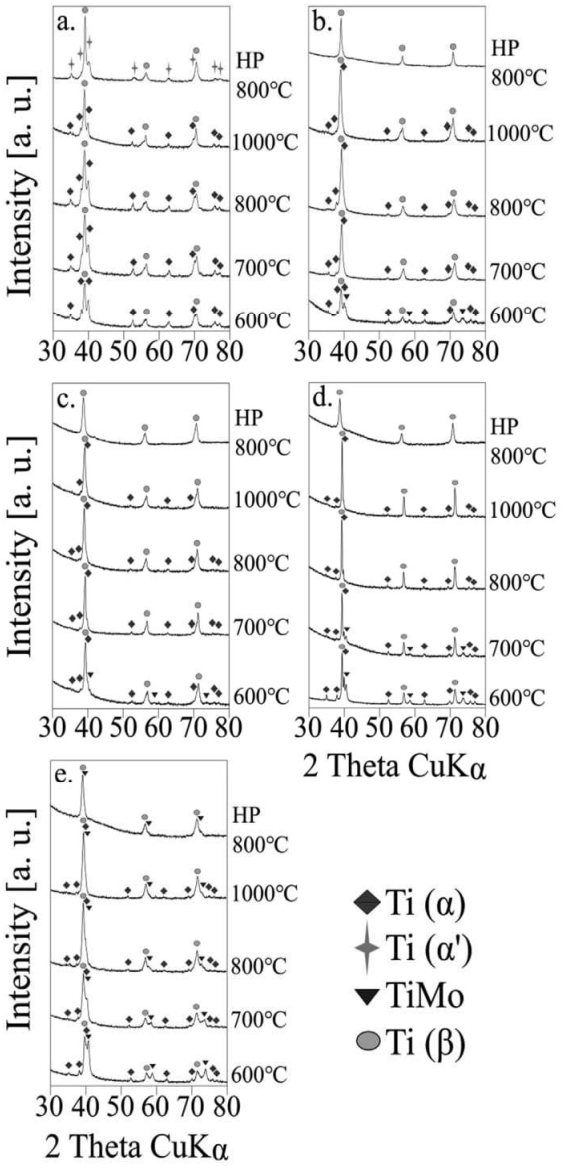

Fig. 4. XRD spectra of bulk Ti-x at. % Mo mechanically alloyed for 48 h and sintered at 600, 700, 800, 1000 °C and HP at 800 °C: a) 10 at. %, b) 23 at. %, c) 27 at. %, d) 31 at. % and e) 35 at %.

be distinguished.

Additional for Ti27Mo sample, transmission electron microscopy analysis was conduct to confirm the obtained microstructure and crystallographic order. Revelled for a Ti27Mo sample in Fig. 8 images, located the obtained grain size scale at the fine range. Analysed diffraction pattern confirms cubic Ti(β) phase structure.

Hardness and Young modulus of the Ti-Mo alloys was determined and the results were listed in Table 5. The indentation hardness (HIT), Vickers hardness ($HV_{0.3}$) and indentation modulus (EIT) were evaluated from the indentations plots which were shown in Fig. 9.

The room temperature load-displacement curves of synthesized Ti-Mo alloys confirmed in nearly all cases, lower than commercial pure Ti (α) modulus values (140 GPa) [36], interpreted from the line course. It was also noticed from Table 5, that the higher average value of EIT characterize the HP samples due to lower porosity values than for CP one. For example in the case of the bulk HP Ti27Mo alloy with porosity 0.04% and porous CP Ti27Mo alloy with porosity 24.74%, the Young modulus equals 139.5 and 91.2 GPa, respectively.

The microhardness of the sintered samples exhibited various distributions that were related to compositional changes. The Vickers hardness for all bulk HP Ti-Mo alloys reached 460 $HV_{0.3}$ and are almost triple as high as that of pure microcrystalline Ti-α (180 $HV_{0.3}$) [36].

Obtained results, stay in accordance to the solid solution and/or precipitation strengthening effect, which for the introduces stress and traps for dislocation movement as other phases, reduce the grain growth also at elevated temperature. For above-discussed effect not without meaning stays; starting powder material size relation and obtained homogeneous substrates distribution after MA. The mechanical alloying in the same results in structure refinement. Obtained after sintering smaller grains, increase the volume contribution of the grain boundaries in the whole volume of the material that finally corresponds to a higher strength. The grain boundaries act against dislocation movements, and this relation is explained by the Hall-Petch equation.

4. Discussion

Presented results clearly demonstrate that powder manufacturing route allows production of β Ti-based alloys. Our results show that the crystal structure of solution treated alloys are sensitive to Mo contents. When Mo content increases in Ti-Mo system the β phase becomes the only dominant phase. Mo stabilizes the β-Ti structure and promotes the spontaneous passivation of the alloys [21]. Additionally, Mo can help to suppress the ω-phase appearance and in many compositions may have a unique properties such as a shape memory effect [15,17,42,43]. The control of the crystalline phases is of great importance in the design of new alloys for biomedical applications.

The phase and crystal structures of Ti–Mo alloys synthesized in this work are summarized in Table 3. When the alloys contain 8 at. % Mo or more, β phase became the only dominant phase. It is well known that ω phase is formed in the metastable β type alloys, and the amount of ω phase depends significantly on the stability of the β phase [42]. With the increase of Mo content, the β phase is more stable.

The elastic modulus is sensitive to the phase/crystal structure of Ti alloys. β Ti alloys generally have a lower elastic modulus than that of the α or α + β type alloys [43,44]. According to the published data, the ω phase has the highest elastic modulus, and the martensitic α″ phase has a lower modulus than the martensitic α′ phase, and the β phase has the lowest modulus in Ti–Mo alloys. The result of some early studies shows that the elastic modulus can be controlled by the content of alloying elements in Ti alloys. Pure β phase or α″ single phase are always expected to be obtained in Ti–Mo alloys. The pure β phase can be obtained only if α′ phase and ω phase can be suppressed through increasing the content of the β-stabilizing element (e.g., Mo).

Fine and ultrafine-grained materials due to their size, may enhance physicochemical, mechanical and biological properties compared with the corresponding materials with microcrystalline grain size [23,34]. Valiev and co-workers apply a process known as equal channel angular pressing (ECAP), which is a viable processing route to grain refinement and property improvement [30]. Cytocompatibility tests utilizing fibroblast mice cells L929 were carried

Table 2
Phase amounts determined by the Rietveld method.

alloys	T [°C]	sig	R_{wp} [%]	R_{exp} [%]	Ti(β) [%]	Ti(α) [%]	Ti(α′) [%]	(MoTi) [%]
Ti-10 at. % Mo	600	1.3588959	7.26000317	5.342596	63.61	36.39	–	–
	700	1.7369086	7.231819	4.1636157	72.00	28.00	–	–
	800	1.828498	7.9643564	4.3556824	72.90	27.10	–	–
	1000	1.7364146	8.793383	5.0641036	84.18	15.82	–	–
	HP 800	**2.412863**	**10.728335**	**4.4463096**	**73.25**	**-**	**26.75**	**-**
Ti-23 at. % Mo	600	1.2343249	6.6812625	5.412888	72.22	16.72	–	11.06
	700	1.7970943	5.8089623	3.2324193	94.44	5.56	–	–
	800	1.7763894	5.885216	3.3130217	94.83	5.17	–	–
	1000	1.8122728	6.284918	3.4679756	95.27	4.73	–	–
	HP 800	**2.3671894**	**8.234684**	**3.4786754**	**100.00**	**-**	**-**	**-**
Ti-27 at. % Mo	600	1.3267181	5.3600826	4.040107	88.90	7.49	–	3.61
	700	1.7383119	7.440266	4.2933946	95.36	4.64	–	–
	800	1.593477	6.7736397	4.250855	95.93	4.07	–	–
	1000	1.4466127	6.01129	4.1554246	97.61	2.39	–	–
	HP 800	**2.7457373**	**11.205753**	**4.0811453**	**100.00**	**-**	**-**	**-**
Ti-31 at. % Mo	600	1.6264594	5.19341	3.193077	59.78	22.83	–	17.39
	700	1.4481523	6.1851983	4.271096	78.15	11.10	–	10.75
	800	1.317118	6.5026984	4.9370656	93.23	6.77	–	–
	1000	1.2014796	5.381764	4.4792805	94.98	5.02	–	–
	HP 800	**2.7709262**	**11.446373**	**4.130883**	**100.00**	**-**	**-**	**-**
Ti-35 at. % Mo	600	1.9581753	6.242858	3.1880996	42.94	11.96	–	45.10
	700	1.4797326	4.7622957	3.218349	72.80	6.74	–	20.46
	800	1.5083703	4.7301025	3.1359903	81.37	2.98	–	15.65
	1000	1.3265590	4.4007497	3.3174174	92.86	2.28	–	4.86
	HP 800	**2.239303**	**7.8918023**	**3.5242224**	**83.99**	**-**	**-**	**16.01**

Table 3
Structural phase parameters of analysed alloys.

alloys	T [°C]	Ti(β)		Ti(α)			Ti(α′)			(MoTi)	
		a	V	a	c	V	a	c	V	a	V
		[Å]	[Å^3]	[Å]	[Å]	[Å^3]	[Å]	[Å]	[Å^3]	[Å]	[Å^3]
Ti-10 at. % Mo	600	3.2723(2)	35.041(5)	2.9627(3)	4.7401(11)	36.033(16)	–	–	–	–	–
	700	3.2701(1)	34.970(3)	2.9579(4)	4.7378(13)	35.899(20)	–	–	–	–	–
	800	3.2758(2)	35.151(5)	2.9623(4)	4.7412(14)	36.032(21)	–	–	–	–	–
	1000	3.2759(2)	35.154(5)	2.9652(6)	4.7598(19)	26.244(28)	–	–	–	–	–
	HP 800	3.2577(1)	35.574(4)	–	–	–	2.9481(9)	4.7105(28)	35.456(42)	–	–
Ti-23 at. % Mo	600	3.2514(2)	34.374(7)	2.9595(6)	4.7278(17)	35.860(27)	–	–	–	3.1526(7)	31.335(20)
	700	3.2476(1)	34.252(3)	2.9665(10)	4.7682(30)	36.339(48)	–	–	–	–	–
	800	3.2453(0)	34.178(1)	2.9700(10)	4.7540(28)	36.316(45)	–	–	–	–	–
	1000	3.2600(3)	34.645(10)	2.9698(15)	4.7677(48)	36.416(73)	–	–	–	–	–
	HP 800	3.2570(0)	34.550(1)	–	–	–	–	–	–	–	–
Ti-27 at. % Mo	600	3.2461(1)	34.204(3)	2.9617(7)	4.7474(23)	36.063(35)	–	–	–	3.1469(17)	31.164(50)
	700	3.2477(1)	34.255(3)	2.9668(8)	4.7602(25)	36.286(38)	–	–	–	–	–
	800	3.2549(1)	34.483(4)	2.9695(12)	4.7675(38)	36.407(58)	–	–	–	–	–
	1000	3.2532(1)	34.42994)	2.9702(19	4.7737(61)	36.473(93)	–	–	–	–	–
	HP 800	3.2839(3)	35.415(9)	–	–	–	–	–	–	–	–
Ti-30 at. % Mo	600	3.2325(1)	33.776(2)	2.9596(2)	4.7399(5)	35.955(8)	–	–	–	3.1479(2)	31.195(7)
	700	3.2345(1)	33.840(2)	2.9616(5)	4.7508(15)	36.087(24)	–	–	–	3.1481(9)	31.198(26)
	800	3.2373(0)	33.926(1)	2.9704(4)	4.7716(12)	36.460(18)	–	–	–	–	–
	1000	3.2394(0)	33.995(1)	2.9731(10)	4.7729(31)	36.537(49)	–	–	–	–	–
	HP 800	3.2767(4)	35.180(13)	–	–	–	–	–	–	–	–
Ti-35 at. % Mo	600	3.2132(3)	33.176(8)	2.9527(7)	4.7217(66)	35.651(66)	–	–	–	3.1401(3)	30.963(8)
	700	3.2329(2)	33.789(5)	2.9659(11)	4.7573(26)	36.242(46)	–	–	–	3.1595(3)	31.539(10)
	800	3.2271(1)	33.607(4)	2.9978(35)	4.7751(72)	37.164(143)	–	–	–	3.1735(5)	31.960(15)
	1000	3.2171(1)	33.977(4)	2.9777(10)	4.7842(22)	36.737(41)	–	–	–	3.1709(6)	31.883(17)
	HP 800	3.2389(2)	33.957(7)	–	–	–	–	–	–	3.0647(19)	28.785(55)

Table 4
Theoretical density (ρ_{th}), calculated density of the porous materials (ρ_{cal}) and porosity (P) of bulk Ti-x at. % Mo alloys.

alloys	T [°C]	ρ_{th} [g/cm^3]	P [%]	ρ_{cal} [g/cm^3]
Ti-10 at. % Mo	800	5.605 ± 0.126	25.60 ± 0.36	4.171 ± 0.368
	HP 800		0.05 ± 0.02	5.603 ± 0.129
Ti-23 at. % Mo	800	6.700 ± 0.177	24.64 ± 0.45	5.049 ± 0.560
	HP 800		0.24 ± 0.08	6.684 ± 0.195
Ti-27 at. % Mo	800	6.953 ± 0.112	24.74 ± 0.14	5.233 ± 0.334
	HP 800		0.04 ± 0.01	6.950 ± 0.115
Ti-31 at. % Mo	800	7.226 ± 0.193	28.70 ± 0.19	5.153 ± 0.633
	HP 800		0.21 ± 0.02	7.211 ± 0.201
Ti-35 at. % Mo	800	7.658 ± 0.230	27.60 ± 1.77	5.544 ± 1.122
	HP 800		0.16 ± 0.03	7.645 ± 0.239

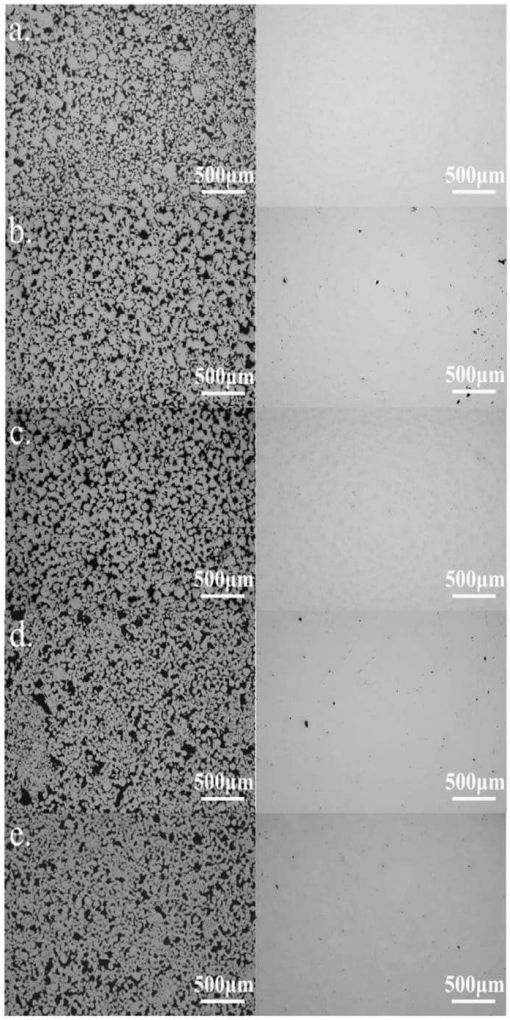

Fig. 5. Optical micrographs of bulk Ti-x at. % Mo sinters obtained after cold pressing and sintering at 800 °C (left) and HP at 800 °C (right): a) 10 at. %, b) 23 at. %, c) 27. at %, d) 31. at % and e) 35 at. % mechanically alloyed powders.

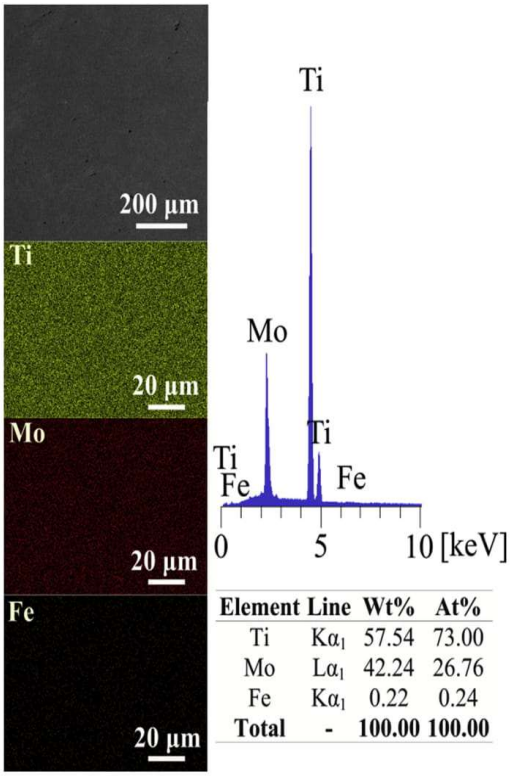

Fig. 6. SEM micrograph, EDS mapping of the Ti, Mo and Fe distribution and EDS spectra of bulk Ti-27 at. % Mo alloy mechanically alloyed for 48 h and sintered at 800 °C for 5 min (HP approach).

out. After nanostructuring, fibroblast colonization of the cp Grade 4 titanium surface increases.

A porosity after powder compaction has also played a role in the cell adhesion. It was proposed that an increased area of the surface defects exposed to the cell culture and to a larger degree of surface electron delocalization caused enhanced cell adhesion.

The variation of elastic modulus in the Ti–Mo alloys shows a trend similar to the microhardness. The elastic modulus firstly increases slightly until 140 GPa at 27 at. % Mo, which is also due to solid solution strengthening [44]. A further increase in the Mo content causes a slight decrease of the Young's modulus to values up to 137 GPa (for x = 31 at %) and these values are considerably lower than that of Co-Cr-Mo (210 GPa) or 316L stainless steel (200 GPa) [43].

5. Conclusions

The aim of this research was synthesis of titanium-molybdenum (Ti-x at. % Mo; x = 10, 23, 27, 31 and 35) alloys. The influence of Mo content and processing method on phase transitions (Ti(α)-Ti(β)) were studied. The results can be summarized as follows:

- longer MA time increase the content of Ti(β)-phase in Ti-x at. % Mo system,
- sintering of the obtained powder material led to the formation of a Ti(β) type alloys,

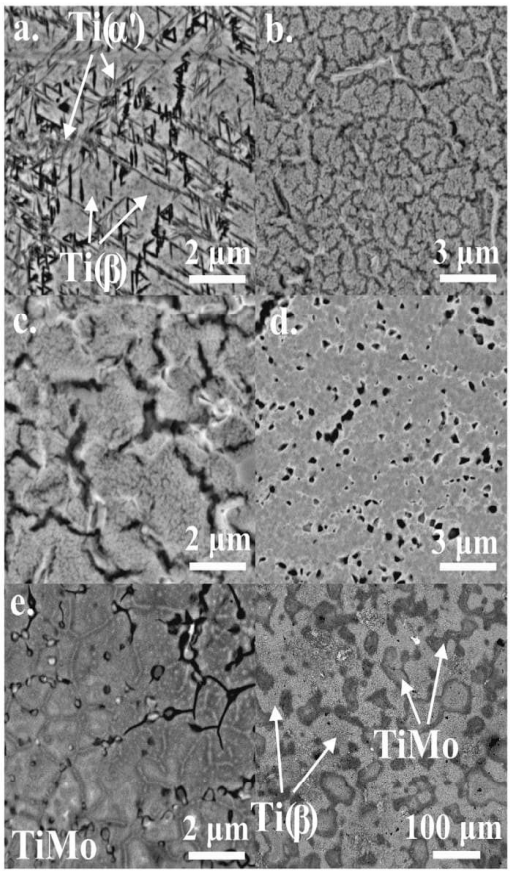

Fig. 7. SEM microphotographs of Ti-x at. % Mo alloys mechanically alloyed for 48 h and HP at 800 °C for 5 min - BSE mode: a) 10 at. %, b) 23 at. %, c) 27 at. %, d) 31 at. % and e) 35 at. %.

Table 5
Vickers hardness ($HV_{0.3}$), Martens hardness (HM) and Young modulus (E) of Ti-x at. % Mo alloys.

alloys	$HV_{0.3} \pm \sigma$	$HM \pm \sigma$ [N/mm^2]	$E \pm \sigma$ [GPa]
Ti-10 at. % Mo HP	499 ± 6	3875.65 ± 41.32	124.20 ± 4.78
Ti-23 at. % Mo HP	454 ± 6	3531.23 ± 32.71	127.29 ± 1.21
Ti-27 at. % Mo HP	495 ± 8	3779.15 ± 44.43	139.51 ± 1.88
Ti-31 at. % Mo HP	494 ± 8	3744.54 ± 28.89	136.76 ± 1.80
Ti-35 at. % Mo HP	540 ± 9	4194.43 ± 73.33	158.38 ± 1.28
Ti-10 at. % Mo CP	363 ± 10	2919.15 ± 72.24	93.83 ± 8.24
Ti-23 at. % Mo CP	366 ± 19	3093.14 ± 111.42	104.87 ± 10.53
Ti-27 at. % Mo CP	351 ± 16	2931.10 ± 34.52	91.20 ± 6.12
Ti-31 at. % Mo CP	337 ± 14	1617.07 ± 673.15	54.80 ± 16.68
Ti-35 at. % Mo CP	357 ± 15	2918.78 ± 1201.74	78.07 ± 33.35

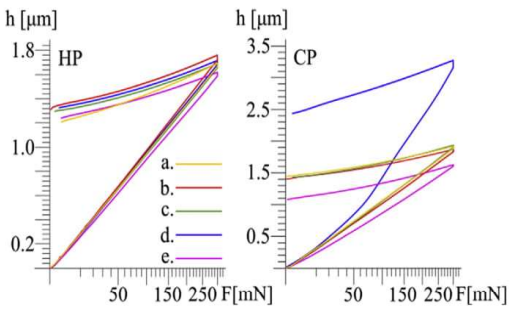

Fig. 9. Load-depth curves of bulk Ti-x at. % Mo samples prepared by the hot pressing and cold pressing with additional sintering at the same processing temperature 800 °C: a) 10 at. %, b) 23 at. %, c) 27 at. %, d) 31 at. % and e) 35 at. %.

- with the increase of Mo contents in Ti-x at. % Mo system an increase of β-phase is noticeable in the obtained sinters,
- with the increase of sintering temperature more Ti(β)-phase in Ti-x at. % Mo system is detected,
- with the increase of Mo contents in Ti-x at. % Mo system an increase of E modulus is noticeable.
- the hot pressing processed samples at low temperature (800 °C) for Ti-Mo system characterizes with increase content of Ti(β) phase in comparison to the cold pressing approach.

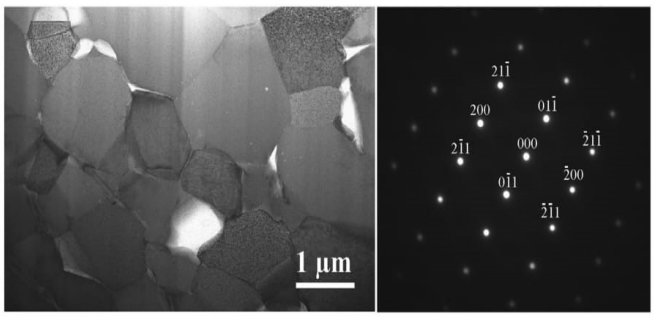

Fig. 8. TEM image of Ti-27 at. % Mo alloy mechanically alloyed for 48 h and sintered at 800 °C for 5 min (HP approach) with electron diffraction pattern taken from one of the grains.

Acknowledgements

The work has been financed by Narodowe Centrum Nauki, National Science Centre Poland under the decision no.: DEC-2017/25/B/ST8/02494.

References

[1] C. Leyens, M. Peters, Titanium and Titanium Alloys: Fundamentals and Applications, Wiley-VCH Verlag GmbH & Co., 2005.
[2] H.J. Rack, J.J. Qazi, Titanium alloys for biomedical applications, Mater. Sci. Eng. C 26 (2006) 1269–1277.
[3] M. Navarro, A. Michiardi, O. Castaño, J.A. Planell, Biomaterials in orthopaedics, J. R. Soc. Interface 5 (2008) 1137–1158.
[4] M. Geetha, A.K. Singh, R. Asokamani, A.K. Gogia, Ti based biomaterials, the ultimate choice for orthopedic implants – a review, Prog. Mater. Sci. 54 (2009) 397–425.
[5] J.Y. Rho, R.B. Ashman, C.H. Turner, Youngs modulus of trabecular and cortical bone material - ultrasonic and microtensile measurements, J. Biomech. 26 (1993) 111–119.
[6] M. Valko, H. Morris, M.T.D. Cronin, Metals, toxicity and oxidative stress, Curr. Med. Chem. 12 (2005) 1161–1208.
[7] E. Kobayashi, H. Doi, M. Takahashi, T. Nakano, T. Yoneyama, H. Hamanaka, Castability and mechanical properties of Ti–6Al–7Nb alloy dental-cast, J. Jpn. Soc. Dent. Mater. Dev. 14 (1995) 406–413.
[8] E. Kobayashi, H. Doi, T. Yoneyama, H. Hamanaka, S. Matsumoto, K. Kudaka, Evaluation of mechanical properties of dental casting Ti–Zr based alloys, J. Jpn. Soc. Dent. Mater. Dev. 14 (1995) 321–328.
[9] O. Okuno, Titanium alloys for dental applications, J. Jpn. Soc. Biomater. 14 (1996) 267–273.
[10] D. Kuroda, M. Niinomi, M. Morinaga, Y. Kato, T. Yashiro, Design and mechanical properties of new beta type titanium alloys for implant materials, Mater. Sci. Eng. A 243 (1998) 244–249.
[11] H. Doi, T. Yoneyama, E. Kobayashi, H. Hamanaka, Mechanical properties and corrosion resistance of Ti–5Al–13Ta alloy castings, J. Jpn. Soc. Dent. Mater. Dev. 17 (1998) 247–252.
[12] W.F. Ho, C.P. Ju, J.H. Chern Lin, Structure and properties of cast binary Ti–Mo alloys, Biomaterials 20 (1999) 2115–2122.
[13] W.-D. Zhang, Y. Liu, H. Wu, M. Song, T.-Y. Zhang, X.-D. Lan, T.-H. Yao, Elastic modulus of phases in Ti–Mo alloys, Mater. Char. 106 (2015) 302–307.
[14] N.G. Jones, R.J. Dashwood, M. Jackson, D. Dye, β phase decomposition in Ti5Al5Mo5V3Cr, Acta Mater. 57 (2009) 3830–3839.
[15] J.L. Murray, The Mo-Ti (Molybdenum-Titanium) system, Bull. Alloy Phase Diagr. 2 (1981) 185–192.
[16] D.J. Lin, C.C. Chuang, J.H. Chern Lin, J.W. Lee, C.P. Ju, H.S. Yin, Bone formation at the surface of low modulus Ti–7.5Mo implants in rabbit femur, Biomaterials 28 (2007) 2582–2589.
[17] C.H. Wang, M. Liu, P.F. Hu, J.C. Peng, J.A. Wang, Z.M. Ren, G.H. Cao, The effects of α″ and ω phases on the superelasticity and shape memory effect of binary Ti-Mo alloys, J. Alloys Compd. 720 (2017) 488–496.
[18] J.-W. Lu, Y.-Q. Zhao, P. Ge, H.-Z. Niu, Microstructure and beta grain growth behavior of Ti–Mo alloys solution treated, Mater. Char. 84 (2013) 105–111.
[19] T. Furuhara, T. Makino, Y. Idei, H. Ishigaki, A. Takada, T. Maki, Morphology and crystallography of α precipitation in βTi–Mo binary alloys, Mater. Trans. 39 (1998) 31–39.
[20] A. Almeida, D. Gupta, C. Loable, R. Vilar, Laser-assisted synthesis of Ti–Mo alloys for biomedical applications, Mater. Sci. Eng. C 32 (2012) 1190–1195.
[21] N.T.C. Oliveira, G. Aleixo, R. Caram, A.C. Guastaldi, Development of Ti–Mo alloys for biomedical applications: microstructure and electrochemical characterization, Mater. Sci. Eng. A 452–453 (2007) 727–731.
[22] F.F. Cardoso, P.L. Ferrandini, E.S.N. Lopes, A. Cremasco, R. Caram, Ti–Mo alloys employed as biomaterials: effects of composition and aging heat treatment on microstructure and mechanical behavior, J. Mech. Behav. Biomed. Mater. 32 (2014) 31–38.
[23] T.J. Webster, J.U. Ejiofor, Increased osteoblast adhesion on nanophase metals: Ti, Ti6Al4V, and CoCrMo, Biomaterials 25 (2004) 4731–4739.
[24] G. Adamek, J. Jakubowicz, Mechanoelectrochemical synthesis and properties of porous nano Ti-6Al-4V alloy with hydroxyapatite layer for biomedical applications, Electrochem. Commun. 12 (2010) 653–656.
[25] M.U. Jurczyk, K. Jurczyk, A. Miklaszewski, M. Jurczyk, Nanostructured titanium-45S5 Bioglass scaffold composites for medical applications, Mater. Des. 32 (2011) 4882–4889.
[26] M.U. Jurczyk, K. Jurczyk, K. Niespodziana, A. Miklaszewski, M. Jurczyk, Titanium-SiO_2 nanocomposites and their scaffolds for dental applications, Mater. Char. 77 (2013) 99–108.
[27] A. Miklaszewski, M.U. Jurczyk, M. Kaczmarek, A. Paszel-Jaworska, A. Romaniuk, N. Lipinska, J. Zurawski, P. Urbaniak, M. Jurczyk, Nanoscale size effect in in situ titanium based composites with cell viability and cytocompatibility studies, Mater. Sci. Eng. C 73 (2017) 525–536.
[28] M. Jurczyk (Ed.), Bionanomaterials for Dental Applications, Pan Stanford Publishing, 2012.
[29] D.S. Pathan, S.B. Doshi, S.D. Muglikar, Nanotechnology in implants: the future is mall, Univ. Res. J. Dent. 5 (2015) 8–13.
[30] R.Z. Valiev, I.P. Semenova, E. Jakushina, V.V. Latysh, H. Rack, R.C. Lowe, J. Petrużelka, L. Dluhoš, D. Hrušák, J. Sochová, Nanostructured SPD processed titanium for medical implants, Mater. Sci. Forum 584–586 (2008) 49–54.
[31] K.Y. Xie, Y.B. Wang, Y.H. Zhao, L. Chang, G.C. Wang, Z.B. Chen, Y. Cao, X.Z. Liao, E.J. Lavernia, R.Z. Valiev, B. Sarrafpour, H. Zoellner, S.P. Ringer, Nanocrystalline beta-Ti alloy with high hardness, low Young's modulus and excellent in vitro biocompatibility for biomedical applications, Mater. Sci. Eng. C-Mater. Biol. Appl. 33 (2013) 3530–3536.
[32] C. Suryanarayana, Mechanical alloying and milling, Prog. Mater. Sci. 46 (2001) 1–184.
[33] M. Tulinski, M. Jurczyk, Nanomaterials synthesis methods, in: E. Mansfield, D. Kaiser, D. Fujita, M. Van de Voorde (Eds.), Metrology and Standardization of Nanomaterials: Protocols and Industrial Innovations, Wiley-VCH, 2017, pp. 75–98.
[34] J.W. Park, Y.J. Kim, C.H. Park, D.H. Lee, Y.G. Ko, J.H. Jang, C.S. Lee, Enhanced osteoblast response to an equal channel angular pressing-processed pure titanium substrate with microrough surface topography, Acta Biomater. 5 (2009) 3272–3280.
[35] L. Zhang, T.J. Webster, Nanotechnology and nanomaterials: promises for improved tissue regeneration, Nano Today 4 (2009) 66–80.
[36] M. Marczewski, A. Miklaszewski, M. Jurczyk, Structure evolution analysis in nanocrystalline Zr and Nb-based beta titanium alloys, J. Alloys Compd. 765 (15) (2018) 459–469.
[37] A.C. Fischer-Cripps, Nanoindentation, third ed., Springer-Verlag, New York, 2011.
[38] W.C. Oliver, G.M. Pharr, An improved technique for determining hardness and elastic modulus using load and displacement sensing indentation experiments, J. Mater. Res. 7 (1992) 1564–1583.
[39] P. Sochacka, A. Miklaszewski, M. Jurczyk, The influence of Mo content on phase transformation in Ti-Mo alloys, Arch. Metall. Mater. 62 (2017) 2051–2056.
[40] Y. Mantani, Y. Takemoto, M. Hida, A. Sakakibara, M. Tajima, Phase transformation of α" martensite structure by aging in Ti-8 mass%Mo alloy, Mater. Trans. 45 (No. 5) (2004) 1629–1634.
[41] L. Zhang, H. Zhang, X. Ren, J. Eckert, Y. Wang, Z. Zhu, T. Gemming, S. Pauly, Amorphous martensite in β -Ti alloys, Nat. Commun. 9 (2018) 506, https://doi.org/10.1038/s41467-018-02961-2.
[42] T. Maeshima, M. Nishida, Shape memory properties of biomedical Ti-Mo-Ag and Ti-Mo-Sn alloys, Mater. Trans. 45 (2004) 1096–1100.
[43] G. He, M. Hagiwara, Ti alloy design strategy for biomedical applications, Mater. Sci. Eng. C 26 (2006) 14–19.
[44] Q. Meng, S. Guo, Q. Liu, L. Hu, X. Zhao, A β-type TiNbZr alloy with low modulus and high strength for biomedical applications, Prog. Nat. Sci. Mater. Int. 24 (2014) 157–162.

Artykuł nr 2:

P, Sochacka, A, Miklaszewski, K, Kowalski, M, Jurczyk,

Influence of the Processing Method on the Properties of Ti-23 at,% Mo Alloy

Metals 9 (2019) 931

doi,org/10,3390/met9090931

metals

MDPI

Article

Influence of the Processing Method on the Properties of Ti-23 at.% Mo Alloy

Patrycja Sochacka, Andrzej Miklaszewski, Kamil Kowalski and Mieczyslaw Jurczyk *

Institute of Materials Science and Engineering, Poznan University of Technology, Jana Pawla II 24, 61-138 Poznan, Poland

* Correspondence: mieczyslaw.jurczyk@put.poznan.pl; Tel.: +48-61-665-3508

Received: 1 July 2019; Accepted: 23 August 2019; Published: 26 August 2019

check for updates

Abstract: In this paper, binary β type Ti-23 at.% Mo alloys were obtained by arc melting as well as by mechanical alloying and powder metallurgical process with cold powder compaction and sintering or, interchangeably, hot pressing. The influence of the synthesis method on the microstructure and properties of bulk alloys were studied. The produced materials were characterized by an X-ray diffraction technique, scanning electron microscopy and chemical composition determination. Young's modulus was evaluated with nanoindentation testing method based on the Oliver and Pharr approach. The mechanically alloyed Ti-23 at.% Mo powders, after inductively hot-pressed at 800 °C for 5 min, allowed the formation of single Ti(β) phase alloy. In this case, Young's modulus and Vickers hardness were 127 GPa and 454 $HV_{0.3}$, respectively. Among the examined materials, the porous (55%) single-phase scaffold showed the lowest indentation modulus (69.5 GPa). Analytical approach performed in this work focuses also on the surface properties. The estimation includes the corrosion resistance analyzed in the potentiodynamic test, and also some wettability properties as a contact angle, and surface free energy values measured in glycerol and diiodomethane testing fluids. Additionally, surface modification of processed material by micro-arc oxidation and electrophoretic deposition on the chosen samples was investigated. Proposed procedures led to the formation of apatite and fluorapatite layers, which influence both the corrosion resistance and surface wetting properties in comparison to unmodified samples. The realized research shows that a single-phase ultrafine-grained Ti-23 at.% Mo alloy for medical implant applications can be synthesized at a temperature lower than the transition point by the application of hot pressing of mechanically alloyed powders. The material processing, that includes starting powder preparation, bulk alloy transformation, and additional surface treatment functionalization, affect final properties by the obtained phase composition and internal structure.

Keywords: material processing; mechanical alloying; titanium β alloys; phase transformation; powder metallurgy; X-ray diffraction; fluoroapatite coating; corrosion resistance; contact angle measurements

1. Introduction

Titanium and the Ti-6Al-4V alloy remain the main metallic biomaterials for orthopaedic and dental applications [1–4]. Young's modulus of these biomaterials is, however, much higher than that of the human bone (20–27 GPa) [5]. In order to reduce the undesirable (SSE) stress shielding effect and the mismatch of Young's modulus, some metallic elements such as Zr, Nb, Mo, Ta have been proposed and added to titanium for new Ti(β) or near Ti(β) alloys, such as Ti5Al13Ta [6], Ti5Al5Mo5V3Cr [7,8], Ti5Al5Mo5V3Cr, Ti5Al5Mo5V3Cr1Zr [9], Ti14Zr16Nb [10], and Ti23Zr25Nb [10].

Recent reports have shown that Ti–Mo alloys have great potential for surgical applications [5,11,12]. The studies and evaluation of the phase transformations and mechanical properties of Ti–Mo alloys

have also concluded that the phase composition and mechanical properties remain different for these biomaterials with a changeable Mo content [5,12,13].

The phase diagram of Ti–Mo shows the molybdenum solubility limits in the titanium matrix drag by a temperature reliance [14]. The research confirms that the higher addition of Mo forms a stable Ti(β) phase in Ti-based alloys, and eventually also increases hardness and decreases the elasticity modulus [10]. The microcrystalline Ti–Mo alloys with molybdenum content from 3.2 to 12 at.% were synthesized by the arc melting method [13]. The 3.2 and 8 at.% additions allows only α and β phases to form and characterize with a low elasticity modulus; however, for 4.5, 6, and 7 at.% contents the same research report a high E modulus owing to some presence of the ω phase in the alloy structure.

Independently, the properties of Ti–Mo alloys (with 4–19 wt.%) synthesized by the laser alloying method were studied [15]. Two-phase biomaterials were obtained for the Mo content in a range 4 to 8 wt.% (martensite and Ti(β) phase). For a concentration higher ≥ 10 wt.%, the obtained alloys were a single β phase.

It has been indicated that the composition and heat treatment strongly influence the microstructure and mechanical properties of Ti–Mo alloys [8,9,16]. Additionally, a high cooling rate enables the production of Ti(β) phase materials for the concentration of 10% of Mo. A strong influence of the structure on the elasticity modulus and hardness were also confirmed for samples aged at 450 °C, following the α and ω phase composition.

It is well known that the properties of Ti-based alloys can be enhanced not only by a changeable composition but also by their microstructure modification [17–27]. For nearly a decade, the application of nano- or ultrafine-grained materials have become very popular in implantology [21,25,27]. The enhancement of properties of Ti-based biomaterials can be obtained by a microstructure control. For example, the top-down approach method can be used: severe plastic deformation (SPD) or mechanical alloying (MA) [21,27].

The MA technique allows the improvement of the material properties by the obtainment of the nanocrystalline or ultrafine structure. As the example, the hardness increase based on the mechanism of grain boundary strengthening [24] can be distinguished. The MA process by cold welding and fragmentation of powder materials leads finally to grain refinement. The additionally obtained nanoscale also creates an inherent morphological change and this, as reports confirm, may influence adhesion, proliferation, and growth cells activity [28].

Recently, Ti–xx at.% Mo (xx = 10–35) alloys have been prepared by mechanical alloying and the powder metallurgy approach [18,29]. The Mo addition to titanium and proper heat treatment of nearly amorphous powders allows the synthesizing of a Ti(β) alloys. In this work, the arc-melting, as well as mechanical alloying and powder metallurgical process based on cold powder compaction and sintering or, alternatively, hot pressing (HP), was applied for the obtainment of the Ti(β)–type (Ti-23 at.% Mo) alloy. For this study, this alloy was labelled Ti23Mo. Additionally, for the Ti23Mo alloy, the micro-arc oxidation (MAO) and electrophoretic deposition (EPD) approaches were applied and led to the formation of apatite and fluorapatite (FA) layers, which improved analyzed surface properties compared to the base sample. The crystal structure, microstructure, composition, porosity, corrosion resistance, mechanical, and surface wetting properties of the bulk synthesized alloy were studied. To date, no attention has been paid to the influence of the processing method on the evolution of the properties in the Ti23Mo biomaterial.

2. Materials and Methods

The present work concludes the research results carried out on the Ti-23 at.% Mo alloy synthesized by different methods. For clearance, obtained materials were marked as follows:

-AM—arc melted;

-AMA800—arc melted and annealed 800 °C/24 h;

-HP—hot-pressed at 800 °C/5 min;

-CP—cold-pressed and sintered at 800 °C/0.5 h;

-CP + NH_4HCO_3—cold-pressed with NH_4HCO_3 and sintered in a vacuum of 10^{-2} Pa in two steps: (i) Space-holder particles burn out at 175 °C for 2 h, (ii) heat-treatment at 1150 °C for 10 h [23];

-CP + MAO—cold-pressed and sintered at 800 °C/0.5 h, samples next treated by micro-arc oxidation;

-CP + MAO + EPD—cold-pressed and sintered at 800 °C/0.5 h, samples next treated by micro-arc oxidation and electrophoretic deposition.

2.1. Sample Preparation

Powders of titanium (<45 μm, 99.9%, Alfa Aesar, Karlsruhe, Germany) and molybdenum (44 μm, 99.6%, Sigma Aldrich, Karlsruhe, Germany) were used as primary materials. Binary β type Ti23Mo alloys were synthesized by arc melting as well as mechanical alloying and the powder metallurgical process with a CP and HP approach.

In the first approach, the microcrystalline Ti23Mo ingot was obtained by arc-melting of the powders on a water-cooled copper pot under Ar. The powders of Ti and Mo were weighed, mixed and placed into the die (8 mm in diameter), uniaxially pressed (600 MPa) and finally arc-melted. The obtained alloy was re-melted three times for homogeneity. Additionally, the arc melted alloy was annealed at 800 °C for 24 h.

In the second approach, the ultra-fine grained materials were synthesized by mechanical alloying and the powder metallurgical process. The MA was performed under Ar (99.999% putity) by the application of the SPEX 8000 Mixer Mill (SPEX SamplePrep, Metuchen, NJ, USA). The total milling time was 48 h. The Ti and Mo powders were weighed, blended, and insert into stainless steel vials in the glove box (LabMaster 130) filled with automatically controlled argon atmosphere (O_2 < 2 ppm and H_2O < 1 ppm).

A ball to powder ratio was set to 10:1. The size of the powders after 48 h of MA was 13.5 nm according to the Williamson–Hall approach calculation method and it was the subject of the detailed investigation with powder processing and preparation in our earlier research [18]. So prepared precursor powders were next processed by the powder metallurgy (CP and HP approach). In the CP approach, precursors were inserted into a die and uniaxially pressed at a pressure of 600 MPa. For sintering, the green compacts were placed in argon-filled quartz tubes and heated for 1 h to 800 °C and then kept at temperature for 30 min. Obtained sinters dimensions were 8 mm diameter and 4 mm height. For the HP samples, an induction module was used for a conductive die heating by the Joule's heat generated on its surface. The HP was carried out at 800 °C for 300 s within a heating step of 800 s in the vacuum (50 Pa) with acting pressure of 60 MPa. A detailed description of the hot pressing procedure was included in the authors' previous work [18].

Additionally, the mechanically alloyed Ti23Mo powders were mixed with ammonium hydrogen carbonate (AHC)-CH_4HCO_3 (500–800 μm, 98%, Alfa Aesar) used as the space-holder filler. The powder mixture prepared by the above-mentioned recipe was uniaxially pressed at the pressure of 400 MPa. Obtained samples dimensions were close to that one from the earlier procedure. The green compacts were next sintered in a vacuum of 10^{-2} Pa in two steps. Firstly, the space-holder particles were burned out at 175 °C for 2 h secondly, the compacts were heat-treated at 1150 °C for 10 h as was performed in the authors' previous research [23]. The porous (55%) Ti23Mo scaffold was obtained by the addition of 35 wt.% AHC to the powder mixture.

Additionally, the surface treatment functionalization based on MAO and EPD process was performed. The oxidation process [30–32] was realized under Atlas Sollich potentiostat (300 V/3 A) equipment control, at a constant voltage of 250 V vs. open circuit potential for 3 min. As the electrolyte, an aqueous solution of 0.01 M $Ca_3(PO_4)_2$, 0.5 M citric acid was chosen.

Fluorapatite particles were hydrothermally prepared by the recipe given in the [33]. Subsequently, the FA suspension in ethanol was magnetically stirred for 30 min followed by 15 min ultrasonic treatment. After the MAO process, electrophoretic deposition [34] of FA was accomplished at the negative voltage −200 V for 1 min in the fluoroapatite suspension in ethanol.

2.2. Materials Characterization

The crystallographic structure examination at the preparation and final processing stages was realized by the Panalytical Empyrean equipment with the copper anode 1.54Å (Almelo, The Netherlands). A detailed description of the structural analysis and evaluation methodology was included in the authors' previous work [17,23].

Additionally, for the lattice parameter estimation and phase quantitative analysis, the Rietveld approach was used. The applied estimation realized in the Maud software involved a simulation of the diffraction patterns based on the structural models for: Ti(α) and Ti(α′) (ref. code 01-071-4632), Ti(β) (ref. code 01-074-7075).

A scanning electron microscopy (SEM, VEGA 5135 Tescan, Brno, Czech Republic) was used to characterize obtained samples microstructure; additionally, for non-etched surfaces observation, optical microscopy was used (Olympus GX51, Shinjuku, Tokio, Japan). For chemical composition determination, the energy dispersive spectrometer adapter (EDS, PTG Prison Avalon, Princeton Gamma Tech., Princeton, NY, USA) was used, calibrated with a typical Cu calibration procedure.

The density of the obtained sinters was determined by the Archimedes drainage method. For the sample porosity measurement, formula $P = (1 - \rho/\rho_{th}) \times 100\%$ was used, where ρ is the density of the porous material and ρ_{th} is its corresponding theoretical density calculated based on the rule of mixtures. For the hardness measurement of the bulk samples, Vickers microhardness testing approach was used (HV). The average value was calculated from the 10 separate indents on each sample for the load of 300 g during 10 s.

Indentation Hardness (HM) and modulus (EIT) of the non-etched Ti23Mo samples, was evaluated by a CSM Instruments nanoindenter with the Berkovich diamond tip [35]. The Depth-sensing indentation technique was used for the measurements of:

-indentation Martens Hardness (HM)

-indentation Modulus (EIT) based on the Oliver and Pharr [36] approach.

A detailed description of the measurements realized at the room temperature based on the ISO 14577 standard for $F = 0.3$ N per 20 s and $C = 5.0$ s parameters was included in the authors' previous work [37].

Additionally, the corrosion resistance properties of the obtained samples were evaluated. The surface of the sample was prepared by grinding in water up to 600 grit. Next, the samples were cleaned ultrasonically with ethanol for 15 min and dried in a cold air stream. For the measurements, the samples were first immersed in the Ringer's solution for 1 h vs. open circuit potential (OCP). The Ag/AgCl electrode was used as the reference electrode in the electrochemical cell. Three measurements for each sample were carried out. The weight loss by polarization was calculated using Faraday's law:

$$W = \frac{EW \cdot I_{corr} \cdot A}{F} \quad (1)$$

W—weight loss [$g \cdot s^{-1}$];
I_{corr}—corrosion current [$\mu A \cdot cm^{-2}$];
EW—equivalent weight [$g \cdot mol^{-1}$];
A—surface [cm^2];
F—Faraday constant [$A \cdot s \cdot mol^{-1}$]

The samples were also immersed in the Ringer's solution for 14 days to measure the weight loss (W by weight loss). Then, they were ultrasonically cleaned for 3 min in a solution of 30 vol.% HNO_3 + 3 vol.% HF (ASTM B 600-91). The weight of the sample was evaluated before and after the immersion (Kern ABT 120-5DM).

The MAO and EPD modified sample surfaces were investigated after drying and 24 h desiccator storage. The XRD analysis was carried out after a single treatment. The obtained diffractograms were

processed by the background subtraction and peaks position determination. Additionally, for the obtained surface development the SEM imaging technique was also used.

For the surfaces wetting investigations the samples which for the additional MAO and EPD processes were not pursued the grinding (up to 400 grit) and ultrasonically rinsing in acetone for cleaning and preparation were followed. The contact angle (CA) of the obtained surfaces was analysed by the optical system with a digital camera (Kruss-DSA25, KRÜSS GmbH, Hamburg, Germany) and estimated by added software (Kruss-Advanced 1.5, KRÜSS GmbH, Hamburg, Germany). A static surface contact angle measurements were carried out with glycerol (99.9%, Chemland, Poland) and diiodomethane (99.9%, Chemland, Poland) testing fluids. The CA values were determined from the geometrical shape of the droplets using the Young–Laplace function and manual baseline correction. Surface free energy (SFE) of analysed samples was estimated from the Owens, Wendt, Rabel, and Kaelble (OWRK) model used today most frequently. It is based on Fowkes and uses contact angles of two liquids with known polar and disperse component of SFE. A detailed description of the surfaces wetting analysis was included in the authors' previous work [20,38].

3. Results and Discussion

The aim of the current study was the synthesis of the Ti23Mo alloy with a beta type structure by arc-melting as well as mechanical alloying and the powder metallurgical process with a CP or HP approach and the evaluation of the properties as a function of microstructure. Additionally, material volumetric and surface functionalization changes were also investigated.

The crystal structure changes during mechanical alloying of Ti23Mo were studied earlier [29]. The typical (hkl) indexes of the titanium and molybdenum remain visible after 15 min of MA. After 5 h of milling, the new MoTi phase is formed. 15 h of milling allows the formation of a new Ti(β) phase. During processing, an energy transfer to a powdered material results in an increase of defects density with a subsequent subgrains formation, which may eventually even lead to material amorphization [39]. Processed for 48 h, the powder mixture evinces a strongly amorphous character with a crystallite size value estimated by the Williamson–Hall UDM approach close to 13 nm with an increases microstrain level at the range of 5.6×10^{-3} [18]. The XRD analysis confirms for MA processed powder the phase transition possibility from (α) to (β) form during synthesis. What earlier research also shows is that the molybdenum content and the milling time remain crucial parameters responsible for transformation control [29].

The processed arc-melted, CP and HP sinters samples spectra were gathered in Figure 1. The XRD analysis that includes the microcrystalline arc melted (Figure 1a), arc melted and annealed (800 °C/24 h) (Figure 1b), hot-pressed and sintered (Figure 1c), cold-pressed and sintered (Figure 1d), as well as the scaffold samples with the porosity of 55% (Figure 1e), was revealed. The sintering results in the formation of bulk materials. A single-phase, β-type, Ti23Mo alloy and a Ti23Mo scaffold with the porosity of 54.7% were obtained by the HP approach and CP with the addition of ammonium hydrogen carbonate and sintering. The arc-melted sample is also a pure Ti(β) phase-type alloy. For the Ti-23Mo sample (arc-melted and annealed at 800 °C for 24 h), due to high saturation, another Ti(α')phase was detected in the β phase region (Figure 1b). Its content equals 17.0%. The obtained two-phase sample structure is characterized by a homogenous low porosity microstructure. On the other hand, the cold-pressed and sintered sample mostly remain a β-type one, with some (5.2%) content of the second Ti(α) phase. The structural parameters of the synthesized Ti23Mo alloys are summarized in Table 1. The porous and nearly fully light-reflective Ti23Mo alloy surfaces are shown in Figure 2 for which the EDS results have confirmed their chemical composition (Figure 3). The small content of an impurity (α-Fe) was detected in the MA sintered samples, due to the erosion of the milling media. The hot pressing method allows the synthesizing of a bulk Ti23Mo alloy of very low porosity (Table 2, Figure 2c). As can be seen, the porosity heavily depends on the processing method.

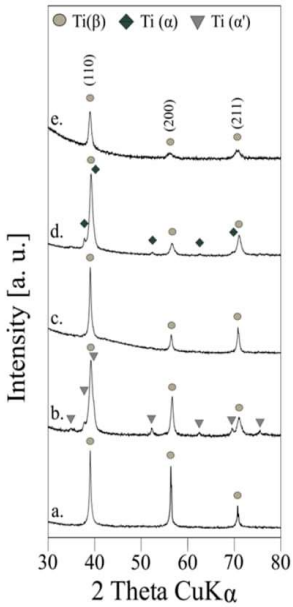

Figure 1. XRD spectra of Ti23Mo alloys obtained by different processing approaches: Arc melted (**a**), arc melted and annealed at 800 °C/24 h (**b**), MA for 48 h and: hot pressed at 800 °C/5 min (**c**), cold-pressed and sintered at 800 °C/0.5 h (**d**) and cold-pressed with NH_4HCO_3 and sintered at 1150 °C/10 h (**e**).

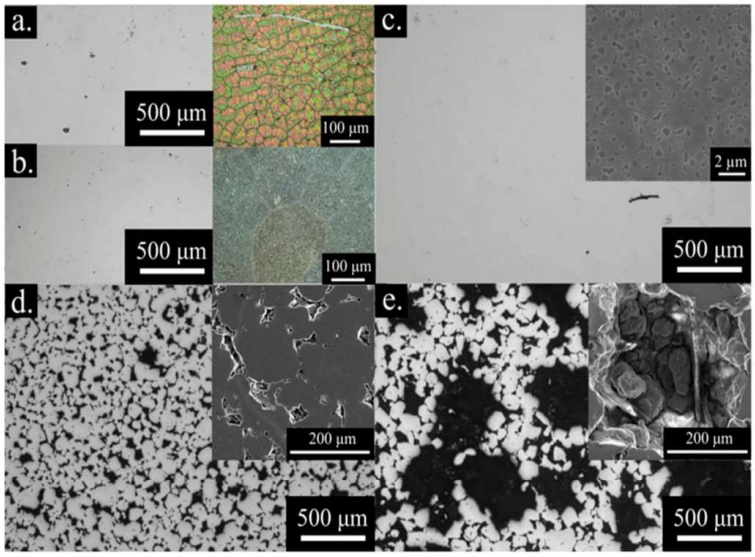

Figure 2. Optical and SEM microphotographs of Ti23Mo alloys obtained by different processing approaches: Arc melted (**a**), arc melted annealed at 800 °C/24 h (**b**), MA for 48 h and: hot pressed at 800 °C/5 min (**c**), cold-pressed and sintered at 800 °C/0.5 h (**d**) and cold-pressed with NH_4HCO_3 and sintered at 1150 °C/10 h (**e**).

Table 1. The structural parameters of Ti23Mo alloys synthesized by different processing approaches, estimation based on the Rietveld approach with phase amounts values (A%).

Material	Sig	R_{wp} (%)	R_{exp} (%)	Phase Type	A (%)	Structural Parameters		
						a (Å)	c (Å)	V (Å^3)
AM	2.666797	10.484024	3.9313207	Ti(β)	100.0	3.2619(1)	-	34.707(3)
AMA800	1.573098	6.3340626	4.0264897	Ti(β)	82.98	3.2475(1)	-	34.250(3)
				Ti(α′)	17.02	2.9712(11)	4.7592(18)	36.385(41)
HP	2.3671894	8.234684	3.4786754	Ti(β)	100.0	3.2570(0)	-	34.550(1)
CP	1.7763894	5.885216	3.3130217	Ti(β)	94.80	3.2453(0)	-	34.178(1)
				Ti(α)	5.20	2.9700(10)	4.7540(28)	36.316(45)
CP + NH_4HCO_3	1.1901675	5.851319	4.9163833	Ti(β)	100.0	3.2615(2)	-	34.659(7)

Table 2. Theoretical density (ρ_{th}), calculated density (ρ_{cal}), and porosity (P) of Ti23Mo alloy obtained by different processing approach.

Material	ρ_{th} (g/cm^3)	ρ_{cal} (g/cm^3)	P (%)
AM	6.695 ± 0.164	6.674 ± 0.180	0.31 ± 0.06
AMA800	6.695 ± 0.164	6.691 ± 0.167	0.06 ± 0.01
HP	6.700 ± 0.177	6.684 ± 0.195	0.24 ± 0.08
CP	6.688 ± 0.219	5.040 ± 0.671	24.64 ± 0.45
CP + NH_4HCO_3	6.690 ± 0.095	3.046 ± 0.578	54.47 ± 0.67

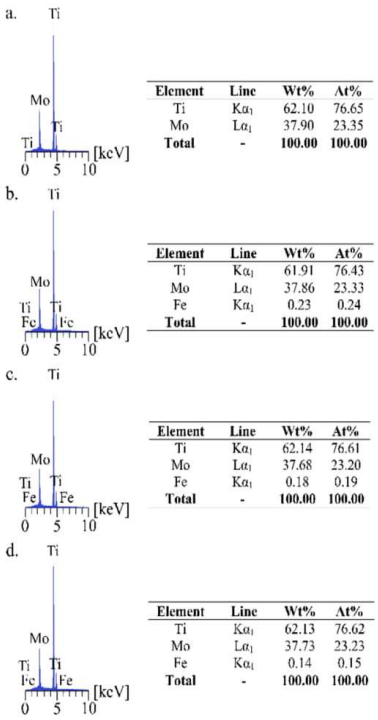

Figure 3. The amount of elements in Ti23Mo alloy: Arc melted (**a**), hot pressed (800 °C/5 min) (**b**), cold-pressed at 800 °C/0.5 h (**c**), cold-pressed with NH_4HCO_3 at 1150 °C/10 h (**d**) with their EDS spectra.

The SEM analysis was conducted to confirm the ultrafine-grained structure in the hot-pressed sinters. The highly magnified BSE mode microphotograph of the hot-pressed Ti23Mo sample presented in Figure 2c (top right-hand corner), confirmed the microstructure size range.

The Martens hardness (HM), Vickers microhardness ($HV_{0.3}$), and indentation modulus (E_{IT}) were shown for all the indentations selected (Table 3, Figure 4). The microhardness of the sintered samples shown a variety of distribution that was related to the microstructural changes. For example, the Vickers microhardness for the microcrystalline (arc-melted) and the cold-pressed and sintered (800 °C/0.5 h) alloys reached 547 and 366 $HV_{0.3}$, respectively. In the case of the hot-pressed Ti23Mo alloy, the Vickers microhardness increased to 454 $HV_{0.3}$ and it was almost three times higher compared to microcrystalline Ti (180 $HV_{0.3}$). A ten-times lesser force (300 mN), applied using the indentation depth-sensing technique, shows different results from those of the Vickers and Martens hardness measurements. A smaller examination area, resulting from the application of the Berkovich indenter, reflects more correctly the the material response by avoiding the porosity shear but suffers in the case of a multiphase material of higher scatter. The data shown in Table 3 for the above-mentioned relation, show very close results shared for higher data transparency, confirm sample homogeneousness, and the control of results for standard deviation. Alloying and reduction of structural objects following MA, strengthening of the solid solution as well as the grain refinement mechanism following sintering, allow an improvement of the analyzed material properties.

Table 3. Vickers hardness ($HV_{0.3}$), Martens hardness (HM), and Young's modulus (E_{IT}) of the Ti23Mo alloys obtained by different processing approaches.

Material	$HV_{0.3} \pm \sigma$	HM $\pm \sigma$ (N/mm^2)	$E_{IT} \pm \sigma$ (GPa)
AM	547 ± 7	4289.4 ± 28.2	141.2 ± 2.6
AMA800	366 ± 6	3270.7 ± 47.9	142.8 ± 4.3
HP	454 ± 6	3531.2 ± 32.7	127.3 ± 1.2
CP	366 ± 19	3093.1 ± 111.4	104.9 ± 10.5
CP + NH_4HCO_3	397 ± 17	2880.7 ± 184.3	69.5 ± 8.9

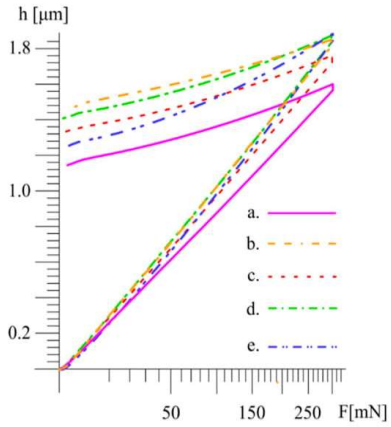

Figure 4. Depth-load (h-F) nanoindentation curves of Ti23Mo alloys obtained by different processing approaches: Arc melted (**a**), arc melted and annealed at 800 °C/24 h (**b**), MA for 48 h and hot pressed at 800 °C/5 min (**c**), cold-pressed and sintered at 800 °C/0.5 h (**d**) and cold-pressed with NH_4HCO_3 and sintered at 1150 °C/10 h (**e**).

The load-displacement curves of the synthesized Ti23Mo alloys and the scaffold are shown in Figure 4. In the case of the hot-pressed alloy (Table 3), the Young's modulus was 127.29 GPa, which was considerably lower than that of the Ti (140 GPa), Co–Cr–Mo alloy (210 GPa), and 316L stainless steel

(200 GPa) commonly used in orthopedic applications [3]. The obtained two-phase Ti23Mo structure in the case of the arc-melted and annealed (800 °C/24 h) alloy is characterized by the highest reported *E* modulus values (Figures 2 and 4). The lower average value of EIT characterizes the porous material of the porosity of 55% (69.5 GPa).

The mechanical properties of the Ti (α′) phase can be controlled by a process of cold working and subsequent low-temperature heat treatment. For example, an α′ martensite high strength alloy Ti-10Nb-2Mo-4Sn (wt.%) could be obtained [40].

The analyzed values of the modules for differently synthesized Ti23Mo alloys show a relation based on phase composition and shear of the microstructural elements. The first relation manifests with the modules drop, due to the appearance of a single beta phase or a diminishment of the second phase for the increased value of the stabilizing elements or different treatment approach. The second relation shows a direct connection to the microstructural features based on its internal structure. The material consistency analyzed in terms of porosity induced intentionally or being the effect of processing, through its volumetric amount influences the resultant value of the module. The above-mentioned relation corresponding with the obtained results indicates a possibility of module shaping.

The authors' earlier results have shown that the crystal structure of the solution treated alloys is sensitive to the Mo contents [18]. When it increases, the β phase becomes the only dominant one. Molybdenum stabilizes the β-Ti structure and may suppress the ω-phase transition, which, in many compositions, may exhibit unique properties such as the shape memory effect [41,42]. The presented results demonstrate that different synthesis methods of the β Ti-based alloys may influence the phase composition as well as the final sinters properties.

It is noteworthy that the elasticity modulus of the studied alloy can be significantly reduced by the introduction of a porous structure [43]. The interconnected porous structure may facilitate the transportation of body fluid and the attachment of the implant to the surrounding bone tissue. For example, the bulk Ti23Mo scaffold with the porosity of 55% has a lower Young's modulus (69.5 GPa) compared to microcrystalline titanium (Table 3). This scaffold exhibited wide cavities of 250–500 μm in diameter (Figure 2e). The optimal pore size for the cell attachment, differentiation, and ingrowth osteoblasts and vascularization is approximately 200–500 μm [44]. In general, great variations in the elastic modulus and the plateau stress of the scaffolds can be achieved by different chemical compositions, pore morphologies, pore sizes and their distributions, shape and thickness of the struts, different compressive strength test parameters employed (sample geometry, size, loading speed) as well as by different fabrication methods [45].

It is well known that the elastic modulus of materials remains sensitive to the phase/crystal structure as well as inherent system confirmation. It has been demonstrated that metastable phases such as α′, α″, ω and β can be formed during quenching from the high-temperature β field, depending on the content of the β-stabilizers (e.g., Zr, Nb, Mo, Ta, etc.) [17,18,46,47].

Due to extremely small grain sizes, ultrafine-grained metals enhance physicochemical, mechanical and biological properties compared with the corresponding materials of a microcrystalline grain size [19,40,48]. A small degree of residual porosity after powder compaction also plays a role in the cell adhesion.

Earlier, Collings, and Gebel studied the elastic modulus in Ti–Mo alloys [49]. Firstly, due to solid solution strengthening, the *E* modulus increased lightly until 120 GPa at 7.5 wt.% Mo. A further increase in the Mo content caused a decrease of Young's modulus corresponding to the transition to the β phase microstructure. A minimum value of 75 GPa was achieved for the Ti-13 wt.% Mo alloy. A further increase in the Mo content caused a slight increase in the elastic modulus to values up to 90 GPa. These results were in good agreement with those obtained on alloys prepared by casting [50].

The analyzed additional corrosion resistance behavior of the Ti–Mo samples (Table 4 and Figure 5) in the Ringer's solution, shows the relation resulting from the material's porosity and their chemical composition. The obtained corrosion resistance results show the best values for the hot-pressed, and arc-melted and annealed (800 °C/24 h) samples. The potential values, analyzed separately from the

corrosion curves, indicate a possible increase in the speed of the reactions that may take place on the surface, particularly the one with easier access of the liquid environment to the material substructure. The presence of porosity in the analyzed samples plays an essential role in the corrosion behavior of the material. Separate immersing test results confirmed that the weight loss analysis remains in close relation to the earlier discussion.

Table 4. Estimated from Tafel extrapolation corrosion potential (E_{corr}) and current (I_{corr}) with calculated weight loss from Faraday law (W by polarization) and after 14 days immersing in Ringer solution environment (W by weight loss) of Ti23Mo alloys obtained by different processing approaches.

Material	E_{corr} (V)	I_{corr} ($\mu A \cdot cm^{-2}$)	W by Polarization ($\mu g \cdot day^{-1}$)	W by Weight Loss ($\mu g \cdot day^{-1}$)
AMA800	−0.556(2)	0.3913(66)	4.7(1)	3.5(5)
HP	−0.276(6)	0.3333(355)	4.0(4)	1.7(2)
CP	−0.610(3)	4.506(705)	53.7(8)	73.3(6)
CP + NH_4HCO_3	−0.511(4)	1.139(313)	13.6(2)	42.3(8)

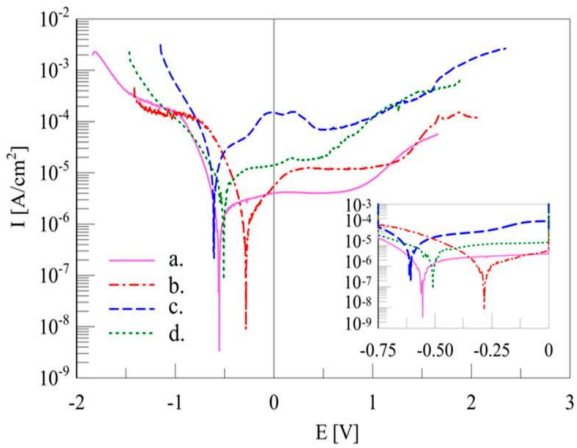

Figure 5. Potentiodynamic test result curves of Ti23Mo alloys obtained by different processing approaches in Ringer solution: Arc melted and annealed at 800 °C/24 h (**a**), MA for 48 h and hot pressed at 800 °C/5 min (**b**), cold-pressed and sintered at 800 °C/0.5 h (**c**) and cold-pressed with NH_4HCO_3 and sintered at 1150 °C/10 h (**d**).

Additionally, for the cold-pressed and sintered at 800 °C/0.5 h samples, surface functionalization by MAO and EPD was investigated. The structural analysis (Figure 6) of obtained modified surfaces confirms, beside strong Ti(β)substrate reflexes for MAO, a complex composition based on the oxides-Ti_6O (01-073-1118)/$CaTiO_3$ (01-075-0437), hydroxides-$Ca(OH)_2$ (04-014-7726), and apatite-$Ca_3(PO_4)_2$ (00-048-0488) mixture, as for EPD a fluorapatite layer (FA 01-071-0881). The morphological view of the samples revealed on SEM microphotographs (Figure 7), allows the characterization of the obtained surfaces as highly developed ones, with a specific formation. The EPD process fully obscures the MAO procedure, however, what remains important and confirmed in FA layer formation [51–53] is the influence of the substrate relation.

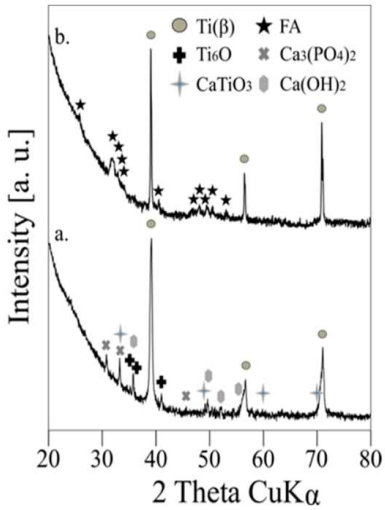

Figure 6. XRD spectra of Ti23Mo alloy MA for 48 h and cold-pressed and sintered at 800 °C/0.5 h and next surface-treated: MAO (**a**), MAO + EPD (**b**).

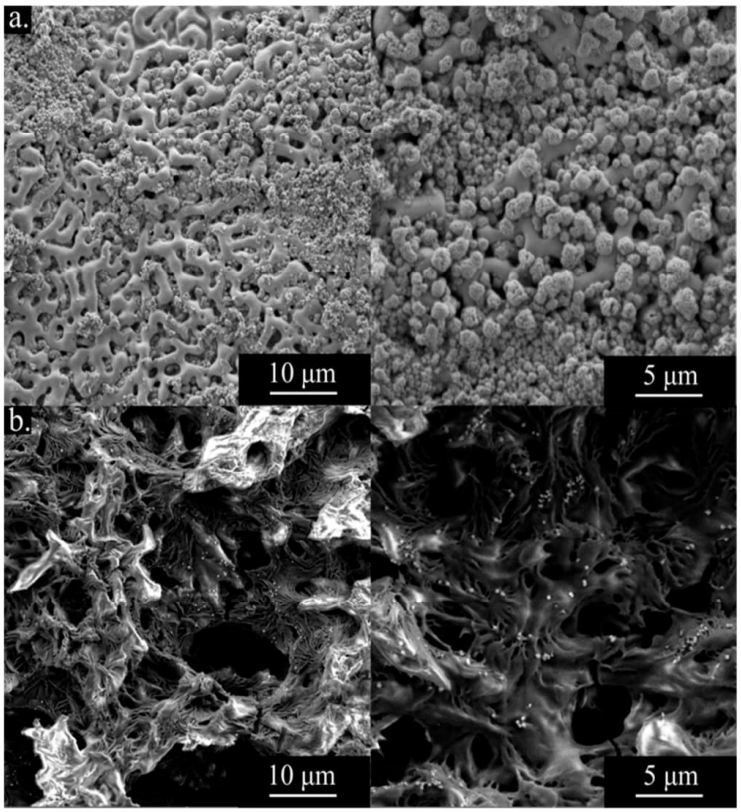

Figure 7. SEM micrographs of CP samples after surface treatment: MAO (**a**), MAO and EPD (**b**).

The evaluation of corrosion resistance in Ringer's solution (Table 5 and Figure 8) of modified layers shows visible improvement in accordance with the base sample. Also, what the collation of the potentiodynamic curves shows in Figure 8 is the specific sample behaviour in comparison to all analyzed processing examples.

Table 5. Estimated from Tafel extrapolation corrosion potential (E_{corr}) and current (I_{corr}) with calculated weight loss form Faraday law (W by polarization) and after 14-days immersing in Ringer solution environment (W by weight loss) of Ti23Mo alloys obtained by different processing approaches.

Material	E_{corr} (V)	I_{corr} (μA·cm^{-2})	W by Polarization (μg·day^{-1})	W by Weight Loss (μg·day^{-1})
CP	−0.610(3)	4.506(705)	53.7(8)	73.3(6)
CP + MAO	−0.194(2)	0.8367(376)	4.4(2)	2.8(5)
CP + MAO + EPD	−0.615(6)	7.519(725)	39.5(4)	6.9(3)

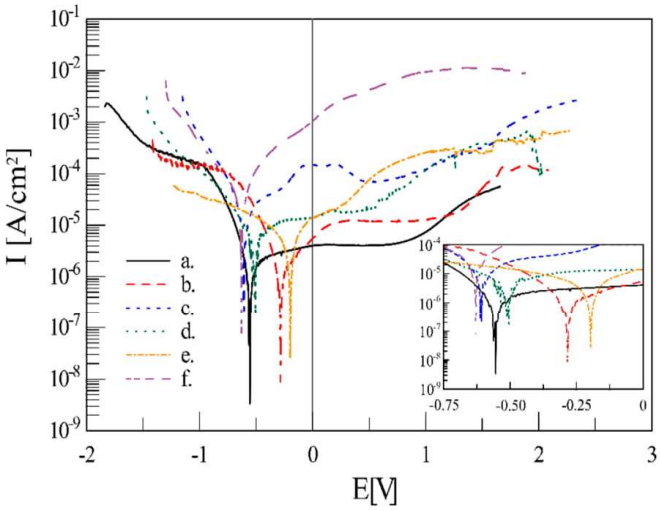

Figure 8. Potentiodynamic test result curves of Ti23Mo alloys obtained by different processing approaches in Ringer solution: Arc melted and annealed at 800 °C/24 h (**a**), MA for 48 h and hot pressed at 800 °C/5 min (**b**), cold-pressed and sintered at 800 °C/0.5 h (**c**), cold-pressed with NH_4HCO_3 and sintered at 1150 °C/10 h (**d**) and cold-pressed and sintered at 800 °C/0.5 h after surface treatment: MAO (**e**), MAO and EPD (**f**).

Finally, surface properties analysis based on the contact angle measurements in glycerol and diiodomethane testing fluids, and further estimation of the surface free energy with disperse and polar components, were performed on the prepared samples. Results (Table 6) confirmed that different processing approaches influence the SFE and it is dependent on structural and internal material characteristics. Secondly, for the additionally CP modified surfaces after MAO and MAO + EPD processes, we observed the decrease of SFE which for the proposed treatment justifies the investigated functionalization step. Low SFE corresponds to high wetting properties which for the hard tissue replacement application remain crucial, especially at the level of molecular activity at the interface region of the host.

Table 6. Contact angle (CA), surface free energy with disperse and polar components for Ti23Mo alloys obtained by different processing approaches.

Material	Diiodomethane CA (°)	Glycerol CA (°)	Surface Free Energy (mN/m)	Disperse (mN/m)	Polar (mN/m)
AMA800	63.62 ± 9.44	62.72 ± 11.30	35.56 ± 6.31	27.84 ± 1.71	7.56 ± 5.26
HP	60.47 ± 5.68	69.98 ± 6.78	31.91 ± 3.16	28.14 ± 3.42	3.61 ± 1.94
CP	53.43 ± 13.61	28.09 ± 4.38	56.34 ± 1.81	32.30 ± 7.75	27.37 ± 4.00
CP + NH_4HCO_3	-	54.34 ± 10.05	-	-	-
CP + MAO	64.64 ± 1.66	50.54 ± 14.46	42.56 ± 9.81	25.91 ± 0.94	16.65 ± 5.38
CP + MAO + EPD	54.93 ± 9.31	41.58 ± 3.35	48.84 ± 1.86	31.85 ± 5.31	16.99 ± 6.15

4. Conclusions

Conducted research allowed a synthesising of a new Ti23Mo alloy by the arc-melting, mechanical alloying, and powder metallurgy methods including cold and hot pressing approaches. Additionally, material volumetric and surface functionalization changes were also investigated. The influence of the processing approach on the phase transitions (α→β), microstructure, corrosion resistance, mechanical and surface wetting properties was studied. The following conclusions can be drawn:

(1) -sintering of MA powder leads to the formation of the Ti(β) based type alloys,
(2) -the HP process at a low temperature (800 °C/5 min) of the Ti23Mo alloy in comparison to the cold pressing and sintering (800 °C/0.5 h) approach allows an obtainment of a low porosity high compactness pure Ti(β) phase,
(3) -the low-temperature sintering (below α→β transus) allows the synthesizing of the bulk materials,
(4) -the obtained microhardness test results favoured the samples with high compactness and low porosity,
(5) -the indentation modulus and estimated sinters parameters obtained in this work confirm a relationship between the material phase and the internal structure,
(6) -the potentiodynamic corrosion resistance analysis indicates a heavy dependence of the obtained results on the material's porosity and their chemical composition,
(7) -the results obtained for surface modified MAO and MAO + EPD treatments confirms that the substrate has a crucial meaning for wetting and corrosion resistance characteristics
(8) -the SFE, as the analysis confirms, stays strongly dependent on structural and internal material characteristics as dictated by different processing approaches.

Author Contributions: P.S., A.M., K.K. and M.J. conducted the experimental and analytical works as well as wrote the manuscript, M.J. supervised the project. All the authors contributed to the critical reading, and editing of the final version of the manuscript.

Funding: The research was financially supported by the Polish National Science Center DEC- 2017/25/B/ST8/02494).

Conflicts of Interest: The authors declare no conflict of interest.

References

1. Okuno, O. Titanium alloys for dental applications. *Soc. Mater. Sci.* **1996**, *14*, 267–273.
2. Rack, H.J.; Qazi, J.I. Titanium alloys for biomedical applications. *Mater. Sci. Eng. C* **2006**, *26*, 1269–1277. [CrossRef]
3. Zhu, Y.C.; Huang, Q.X.; Shi, X.H.; Shuai, M.R.; Zeng, W.D.; Zhao, Y.Q.; Huang, Z.Q.; Ma, L.F. Precipitation location of secondary phase and microstructural evolution during static recrystallization of as-cast Ti-25V-15Cr-0.3Si titanium alloy. *Trans. Nonferrous Met. Soc. China* **2018**, *28*, 1521–1529. [CrossRef]
4. Di, W.U.; Zhang, L.G.; Liu, L.B.; Bai, W.M.; Zeng, L.J. Effect of Fe content on microstructures and properties of Ti6Al4V alloy with combinatorial approach. *Trans. Nonferrous Met. Soc. China* **2018**, *28*, 1714–1723.

5. Li, Y.H.; Wang, F.; Li, J.J. Current developments of biomedical porous Ti–Mo alloys. *Int. J. Mater. Res.* **2017**, *108*, 619–624. [CrossRef]
6. Doi, H.; Yoneyama, T.; Kobayashi, E.; Hamanaka, H. Mechanical properties and corrosion resistance of Ti–5Al–13Ta alloy castings. *J. Jpn. Soc. Dent. Mater. Devices* **1998**, *17*, 247–252.
7. Jones, N.G.; Dashwood, R.J.; Jackson, M.; Dye, D. β Phase decomposition in Ti-5Al-5Mo-5V-3Cr. *Acta Mater.* **2009**, *57*, 3830–3839. [CrossRef]
8. Sen, M.; Suman, S.; Kumar, M.; Banerjee, T.; Bhattacharjee, A.; Kar, S.K. Thermo-mechanical processing window for β phase recrystallization in Ti-5Al-5Mo-5V-3Cr alloy. *Mater. Charact.* **2018**, *146*, 55–70. [CrossRef]
9. Ren, L.; Xiao, W.; Han, W.; Ma, C.; Zhou, L. Influence of duplex ageing on secondary α precipitates and mechanical properties of the near β-Ti alloy Ti-55531. *Mater. Charact.* **2018**, *144*, 1–8. [CrossRef]
10. Lin, D.J.; Chuang, C.C.; Chern Lin, J.H.; Lee, J.W.; Ju, C.P.; Yin, H.S. Bone formation at the surface of low modulus Ti–7.5Mo implants in rabbit femur. *Biomaterials* **2007**, *28*, 2582–2589. [CrossRef]
11. Zhang, W.D.; Liu, Y.; Wu, H.; Song, M.; Zhang, T.Y.; Lan, X.D.; Yao, T.H. Elastic modulus of phases in Ti-Mo alloys. *Mater. Charact.* **2015**, *106*, 302–307. [CrossRef]
12. Ho, W.F.; Ju, C.P.; Chern Lin, J.H. Structure and properties of cast binary Ti–Mo alloys. *Biomaterials* **1999**, *20*, 2115–2122. [CrossRef]
13. Zhao, X.; Niinomi, M.; Nakai, M.; Hieda, J. Beta type Ti–Mo alloys with changeable Young's modulus for spinal fixation applications. *Acta Biomater.* **2012**, *8*, 1990–1997. [CrossRef]
14. Murray, J.L. The Mo-Ti (Molybdenum-Titanium) System. *Bull. Alloy Phase Diagrams* **1981**, *2*, 185–192. [CrossRef]
15. Almeida, A.; Gupta, D.; Loable, C.; Vilar, R. Laser-assisted synthesis of Ti–Mo alloys for biomedical applications. *Mater. Sci. Eng. C* **2012**, *32*, 1190–1195. [CrossRef]
16. Cardoso, F.F.; Ferrandini, P.L.; Lopes, E.S.N.; Cremasco, A.; Caram, R. Ti–Mo alloys employed as biomaterials: Effects of composition and aging heat treatment on microstructure and mechanical behavior. *J. Mech. Behav. Biomed. Mater.* **2014**, *32*, 31–38. [CrossRef]
17. Marczewski, M.; Miklaszewski, A.; Jurczyk, M. Structure evolution analysis in ultrafine-grained Zr and Nb-based beta titanium alloys. *J. Alloys Compd.* **2018**, *765*, 459–469. [CrossRef]
18. Sochacka, P.; Miklaszewski, A.; Jurczyk, M. Development of <beta> type Ti-x at. % Mo alloys by mechanical alloying and powder metallurgy: Phase evolution and mechanical properties ($10 \leq x \leq 35$). *J. Alloys Compd.* **2019**, *776*, 370–378. [CrossRef]
19. Webster, T.J.; Ejiofor, J.U. Increased osteoblast adhesion on nanophase metals: Ti, Ti6Al4V, and CoCrMo. *Biomaterials* **2014**, *25*, 4731–4739. [CrossRef]
20. Jurczyk, K.; Miklaszewski, A.; Jurczyk, M.U.; Jurczyk, M. Development of β type Ti23Mo-45S5 Bioglass nanocomposites for dental applications. *Materials* **2018**, *8*, 5441. [CrossRef]
21. Estrin, Y.; Kasper, C.; Diederichs, S.; Lapovok, R. Accelerated growth of preosteoblastic cells on ultrafine grained titanium. *J. Biomed. Mater. Res. Part A* **2008**, *90*, 1239–1242. [CrossRef]
22. Adamek, G.; Jakubowicz, J. Mechanoelectrochemical synthesis and properties of porous nano Ti-6Al-4V alloy with hydroxyapatite layer for biomedical applications. *Electrochem. Commun.* **2010**, *12*, 653–656. [CrossRef]
23. Jurczyk, M.U.; Jurczyk, K.; Miklaszewski, A.; Jurczyk, M. Nanostructured titanium-45S5 Bioglass scaffold composites for medical applications. *Mater. Des.* **2011**, *32*, 4882–4889. [CrossRef]
24. Miklaszewski, A.; Jurczyk, M.U.; Kaczmarek, M.; Paszel-Jaworska, A.; Romaniuk, A.; Llipinska, N.; Zurawski, J.; Urbaniak, P.; Jurczyk, M. Nanoscale size effect in in situ titanium based composites with cell viability and cytocompatibility studies. *Mater. Sci. Eng. C* **2017**, *73*, 525–536. [CrossRef]
25. Van De Voorde, M. *Nanoscience and Nanotechnology—Advances and Developments in Nano-sized Materials*; De Guyter: Berlin, Germany, 2018; pp. 57–74. ISBN 978-3-11-054722-1.
26. Pathan, D.S.; Doshi, S.B.; Muglikar, S.D. Nanotechnology in implants: The future is small. *Uni. Res. J. Dent.* **2015**, *5*, 8–13.
27. Valiev, R.Z.; Semenova, I.P.; Jakushina, E.; Latysh, V.V.; Rack, H.; Lowe, R.C.; Petruzelka, J.; Dluhos, L.; Hrusak, D.; Sochova, J. Nanostructured SPD processed titanium for medical implants. *Mater. Sci. Forum* **2008**, *584*, 49–54. [CrossRef]
28. Zhang, L.; Webster, T.J. Nanotechnology and nanomaterials: Promises for improved tissue regeneration. *Nano Today* **2009**, *4*, 66–80. [CrossRef]

29. Sochacka, P.; Miklaszewski, A.; Jurczyk, M. The influence of Mo content on phase transformation in Ti-Mo alloys. *Arch. Metall. Mater.* **2017**, *62*, 2051–2056. [CrossRef]
30. Chen, C.; Dong, Q.; Yu, H.; Wang, X.; Wang, D. Microstructure of porous TiO_2 coating on pure Ti by micro-arc oxidation. *Adv. Eng. Mater.* **2006**, *8*, 754–759. [CrossRef]
31. Wu, G.; Wang, Y.; Liu, J.; Yao, J. Influence of the Ti alloy substrate on the anodic oxidation in an environmentally-friendly electrolyte. *Surf. Coat. and Technol.* **2018**, *344*, 680–688. [CrossRef]
32. Babilas, D.; Służalska, K.; Krząkała, A.; Maciej, A.; Socha, R.; Dercz, G.; Tylko, G.; Michalska, J.; Osyczka, A.; Simka, W. Plasma electrolytic oxidation of a Ti–15Mo alloy in silicate solutions. *Mater. Lett.* **2013**, *100*, 252–256. [CrossRef]
33. Chen, M.; Jiang, D.; Li, D.; Zhu, J.; Li, G.; Xie, J. Controllable synthesis of fluorapatite nanocrystals with various morphologies: Effects of pH value and chelating reagent. *J. Alloys Compd.* **2009**, *485*, 396–401. [CrossRef]
34. Mudali, U.K.; Sridhar, T.M.; Rajendran, N. Electrophoretic deposition of TiO2 and TiO2 + CeO2 coatings on type 304L stainless steel. *Surf. Eng.* **2007**, *23*, 267–272. [CrossRef]
35. Fischer-Cripps, A.C. *Nanoindentation*, 3nd ed.; Springer: New York, NY, USA, 2011; ISBN 978-1-4757-5943-3.
36. Oliver, W.C.; Pharr, G.M. An improved technique for determining hardness and elastic-modulus using load and displacement sensing indentation experiments. *J. Mater. Res.* **1992**, *7*, 1564–1583. [CrossRef]
37. Kowalski, K.; Jurczyk, M.U.; Wirstlein, P.K.; Jakubowicz, J.; Jurczyk, M. Influence of 45S5 Bioglass addition on microstructure and properties of ultrafine grained (Mg-4Y-5.5Dy-0.5Zr) alloy. *Mater. Sci. Eng. B* **2017**, *219*, 28–36. [CrossRef]
38. Miklaszewski, A.; Kowalski, K.; Jurczyk, M. Hydrothermal Surface Treatment of Biodegradable Mg-Materials. *Metals* **2018**, *8*, 894. [CrossRef]
39. Suryanarayana, C. Mechanical alloying and milling. *Prog. Mater. Sci.* **2001**, *46*, 1–184. [CrossRef]
40. Guo, S.; Meng, Q.; Chenga, X.; Zhao, X. α′ martensite Ti–10Nb–2Mo–4Sn alloy with ultra low elastic modulus and high strength. *Mater. Lett.* **2014**, *133*, 236–239. [CrossRef]
41. Wang, C.H.; Liu, M.; Hu, P.F.; Peng, J.C.; Wang, J.A.; Ren, Z.M.; Cao, G.H. The effects of α″ and ω phases on the superelasticity and shape memory effect of binary Ti-Mo alloys. *J. of Alloys and Compd.* **2017**, *720*, 488–496. [CrossRef]
42. Grosdidier, T.; Philippe, M.J. Deformation induced martensite and superelasticity in a β-metastable titanium alloy. *Mater. Sci. Eng. A.* **2000**, *291*, 218–233. [CrossRef]
43. Lewis, G. Properties of open-cell porous metals and alloys for orthopaedic applications. *J. Mater. Sci. Mater. Med.* **2013**, *24*, 2293–2325. [CrossRef]
44. Yamamuro, T.; Hench, L.; Wilson, J. *Handbook of Bioactive Ceramics: Vol. 1 and Vol. 2*; CRC Press: Boca Raton, FL, USA, 1990.
45. Gerhardt, L.C.; Boccaccini, A.R. Bioactive glass and glass–ceramic scaffolds for bone tissue engineering. *Materials* **2010**, *3*, 3867–3910. [CrossRef]
46. He, G.; Hagiwara, M. Ti alloy design strategy for biomedical applications. *Mater. Sci. Eng. C* **2006**, *26*, 14–19. [CrossRef]
47. Zhao, X.; Niinomi, M.; Nakai, M. Relationship between various deformation-induced products and mechanical properties in metastable Ti–30Zr–Mo alloys for biomedical applications. *J. Mech. Behav. Biomed. Mater.* **2011**, *4*, 2009–2016. [CrossRef]
48. Wu, X.; Cai, C.; Yang, L.; Liu, W.; Li, W.; Li, M.; Liu, J.; Zhou, K.; Shi, Y. Enhanced mechanical properties of Ti-6Al-2Zr-1Mo-1V with ultrafine crystallites and nano-scale twins fabricated by selective laser melting. *Mater. Sci. Eng. A* **2018**, *738*, 10–14. [CrossRef]
49. Collings, E.; Gegel, H. A physical basis for solid solution strengthening and phase stability in alloys of titanium. *Scr. Metall.* **1973**, *7*, 437–443. [CrossRef]
50. NIiinomi, M. Mechanical properties of biomedical titanium alloys. *Mater. Sci. Eng. A* **1998**, *243*, 231–236. [CrossRef]
51. Kazek-Kęsik, A.; Dercz, G.; Kalemba, I.; Suchanek, K.; Kukharenko, A.; Korotin, D.; Michalska, J.; Krząkała, A.; Piotrowski, J.; Kurmaev, E.; et al. Surface characterisation of Ti–15Mo alloy modified by a PEO process in various suspensions. *Mater. Sci. Eng. C* **2014**, *39*, 259–272. [CrossRef]

52. Bai, Y.; Gao, J.; Wang, C.; Ma, W.; Lee, M.H. Effect of solvent composition on the bioactive coating fabricated by micro-arc oxidation combined with electrophoretic deposition. *Mater. Res. Innovations* **2016**, *20*, 451–457. [CrossRef]
53. Eraković, S.; Janković, A.; Veljović, D.; Palcevskis, E.; Mitrić, M.; Stevanović, T.; Janaćković, D.; Mišković-Stanković, V. Corrosion stability and bioactivity in Simulated Body Fluid of silver/hydroxyapatite and silver/hydroxyapatite/lignin coatings on titanium obtained by electrophoretic deposition. *J. Phys. Chem. B* **2013**, *117*, 1633–1643. [CrossRef]

Artykuł nr 3:

P, Sochacka, A, Miklaszewski, M, Jurczyk, P, Pecyna, M, Ratajczak, M, Gajecka, M,U, Jurczyk,

Effect of hydroxyapatite and Ag, Ta_2O_5 or CeO_2 addition on the properties of ultrafine-grained Ti31Mo alloy

J, Alloys Compd 823 (2020) 153749
doi,org/10,1016/j,jallcom,2020,153749

Journal of Alloys and Compounds 823 (2020) 153749

Contents lists available at ScienceDirect

Journal of Alloys and Compounds

journal homepage: http://www.elsevier.com/locate/jalcom

Effect of hydroxyapatite and Ag, Ta_2O_5 or CeO_2 addition on the properties of ultrafine-grained Ti31Mo alloy

P. Sochacka [a, *], A. Miklaszewski [a], M. Jurczyk [a], P. Pecyna [b], M. Ratajczak [b], M. Gajecka [b, c], M.U. Jurczyk [d]

[a] Poznan University of Technology, Institute of Materials Science and Engineering, Jana Pawla II 24, Poznan, 61-138, Poland
[b] Poznan University of Medical Sciences, Faculty of Pharmacy, Department of Genetics and Pharmaceutical Microbiology, Swiecickiego 4, Poznan, 60-781, Poland
[c] Institute of Human Genetics, Polish Academy of Sciences, Strzeszynska 32, Poznan, 60-479, Poland
[d] Poznan University of Medical Sciences, Division of Mother's and Child's Health, Polna 33, Poznan, 60-535, Poland

ARTICLE INFO

Article history:
Received 3 December 2019
Received in revised form
5 January 2020
Accepted 7 January 2020
Available online 10 January 2020

Keywords:
Titanium alloys
Mechanical alloying
Mechanical properties
Corrosion resistance
Surface free energy
Antibacterial activity

ABSTRACT

In the present study, the crystal structure, microstructure, mechanical and corrosion properties of bulk Ti31MoxHA composites (x = 0, 2.5, 5 and 10 wt %) were investigated. The sintering of Ti31MoxHA powders led to the formation of a bulk composite with grain size of approx. 1 μm. All these composites have elastic modulus lower than CP microcrystalline α-Ti, and their hardness is two times higher. The ultrafine Ti31Mo5HA composite was more corrosion resistant in Ringer solution than the bulk Ti31Mo alloy. Surface wettability measurements revealed the higher surface hydrophilicity of the bulk ultrafine-grained Ti31Mo10HA sample in comparison to microcrystalline Ti sample. Ti31Mo5HA composites with the addition of 1 wt % Ag, 2 wt % Ta_2O_5 or 2 wt % CeO_2 were synthesized, too. The antibacterial activity of Ti31Mo5HA composite containing silver (Ag), tantalum (V) oxide (Ta_2O_5) or cerium (IV) oxide (CeO_2) against *Staphylococcus aureus* was studied. *In vitro* bacterial adhesion, study indicated a significantly reduced number of *S. aureus* on the bulk ultrafine-grained Ti31Mo5HA-Ag (Ce_2O_3) plate surfaces in comparison to microcrystalline Ti plate surface. Ultrafine-grained Ti31Mo5HA - Ag or CeO_2 biomaterials can be considered to be the future generation of medical implants.

1. Introduction

Austenitic steels, Co–Cr alloys, Ni–Cr alloys, and titanium alloys are used to produce medical implants [1–5]. Recently a lot of attention is paid to enhance the biocompatibility of Ti-based alloys [6,7].

Ti–6Al–4V alloy is the main biomaterial for medical applications [5]. However, the Young modulus of this biomaterial is much higher than that of human cortical bone. To eliminate the stress shielding effect which originates from the mismatch of Young's modulus some metallic elements such as Zr, Nb, Mo, Ta, etc have been added to titanium to develop new low modulus β or near β Ti alloys [4,8–10]. By the elimination of toxic elements such as Al and V in Ti–6Al–4V, it is possible to prepare Ti-type alloys with excellent biocompatibility.

Recent studies have demonstrated that Ti–Mo alloys had great potential for surgical applications [5,11–15]. The solubility limits of molybdenum alloying in Ti is 8 wt% [16]. The research has shown that the addition of Mo forms β-phase in Ti-base alloy, and finally, increase the hardness and decrease the Young modulus [17]. The phase transformations and mechanical properties of different Ti–Mo alloys have been investigated and found that the phase constitutions, mechanical properties were different for these biomaterials with different Mo contents [12,14,17].

It has been pointed out, that the improvement of the mechanical properties and biocompatibility of Ti-type alloys can be achieved through microstructure control, the top-down approaches known as severe plastic deformation (SPD) and mechanical alloying (MA) [1,2,17–22]. These biomaterials with nano- or ultrafine-grained microstructure exhibit an interesting combination of mechanical properties. One of the examples could be hardness improvement

* Corresponding author.
E-mail addresses: patrycja.sochacka@doctorate.put.poznan.pl (P. Sochacka), andrzej.miklaszewski@put.poznan.pl (A. Miklaszewski), mieczyslaw.jurczyk@put.poznan.pl (M. Jurczyk), pa.pecyna@gmail.com (P. Pecyna), ratajczak.magdalena@wp.pl (M. Ratajczak), gamar@man.poznan.pl (M. Gajecka), mjur@poczta.onet.pl (M.U. Jurczyk).

https://doi.org/10.1016/j.jallcom.2020.153749

due to the grain boundary strengthening mechanism [23].

An alternative method for changing the properties of metal-based biomaterials is the production of a composite [18,20–22,24]. The hydroxyapatite (HA, $Ca_{10}(PO_4)_6(OH)_2$) and 45S5 Bioglass (44.8% SiO_2, 24.9% Na_2O, 24.5% CaO, 5.8% P_2O_5) [25] are the main ceramics used in medical applications. Composites containing titanium or Ti-based alloys and bioceramic as a reinforced phase are promising alternatives in comparison to conventional materials because they can match the properties of bone tissue in order to enhance bone healing.

Earlier, Ti23Mo–45S5 Bioglass composite was developed by the introduction of 45S5 Bioglass (BG) powders into the Ti23Mo matrix [26]. As a result, the corrosion resistance significantly changed after the electrochemical treatment and Ca–P deposition and the rough, electrochemically biofunctionalized surface (porous with Ca–P layer) supports osteoblast cell growth and proliferation.

Recently, Ti–x at.% Mo (x = 10–35) alloys have been synthesized by mechanical alloying and the powder metallurgy approach [17]. The Mo addition to titanium and proper heat treatment of nearly amorphous powders allow the synthesizing of a Ti (β) alloys. The mechanically alloyed Ti–Mo alloys upon sintering at 800 °C for 5 min led to the formation of single β type phase materials with low elastic modulus and ultrafine-grained microstructure. Additionally, for the Ti23Mo alloy, the micro-arc oxidation (MAO) and electrophoretic deposition (EPD) approaches were applied and led to the formation of apatite and fluorapatite (FA) layers, which improved the surface properties compared to the base sample [27,27].

In this study, the mechanical alloying and powder metallurgy process was applied for the synthesis of the ultrafine-grained Ti–31Mo-*x* wt. % HA composites (x = 0, 2.5, 5 and 10). Till now, no attention has been paid to the influence of HA addition on the crystal structure, mechanical and corrosion properties evolution in ultrafine-grained Ti31Mo alloy. Additionally, the antibacterial activity of Ti31Mo5HA composite containing silver (Ag), tantalum (V) oxide (Ta_2O_5) or cerium (IV) oxide (CeO_2) against *Staphylococcus aureus* was assessed. The influence of microstructure and chemical composition of Ti31Mo*x*HA and Ti31Mo5HA-Ag (or Ta_2O_5, CeO_2) composites on the crystal structure, microstructure, mechanical properties, corrosion behavior, surface wettability and antibacterial activity against *S. aureus* were investigated in details.

2. Materials and methods

The present work contains results of research carried out for Ti-31 at. % Mo - based composites. In this study, synthesized materials are denoted as follows:

- Ti31Mo – mechanically alloyed, cold-pressed and sintered at 800 °C/0.5 h Ti-31 at.% Mo alloy,
- Ti31Mo*x*HA (x = 2.5, 5 and 10 wt%) – mechanically alloyed, cold-pressed and sintered at 800 °C/0.5 h Ti-31 wt% Mo - *x* HA composites,
- Ti31Mo5HA1Ag – mechanically alloyed, cold-pressed and sintered at 800 °C/0.5 h Ti-31 wt% Mo - 5 wt% HA - 1 wt% Ag composite,
- Ti31Mo5HA2Ta_2O_5 – mechanically alloyed, cold-pressed and sintered at 800 °C/0.5 h Ti-31 wt% Mo - 5 wt% HA - 2 wt% Ta_2O_5 composite.
- Ti31Mo5HA2CeO_2 – mechanically alloyed, cold-pressed and sintered at 800 °C/0.5 h Ti-31 wt% Mo - 5 wt% HA - 2 wt% CeO_2 composite.

2.1. Sample preparation

Powders of Ti (<45 μm, 99.9%, Alfa Aesar), Mo (44 μm, 99.6%, Sigma Aldrich), HA (reagent grade, Sigma Aldrich), Ag (5–8 μm, ≥99.9%, Sigma Aldrich), Ta_2O_5 (250 μm, 99.5%, Sigma Aldrich) and CeO_2 (<5 μm, 99.9%, Sigma Aldrich) were used as primary materials.

The ultrafine-grained Ti31Mo alloy and their composites were synthesized by the application of mechanical alloying and powder metallurgical processes. MA was performed at argon atmosphere by the application of SPEX 8000 Mixer Mill. The total milling time was 39 h. Powders of Ti and Mo, Ti, Mo and HA, Ti, Mo, HA and Ag, Ti, Mo, HA and Ta_2O_5, Ti, Mo, HA, and CeO_2 were weighted, blended and poured into stainless steel vials in the glove box (Labmaster 130). The hard steel balls ratio to powder weight was 10:1. In the next step, the MA powders were placed into the matrix and uniaxially pressed at a pressure of 600 MPa. The sample diameter and height were 8 mm and 4 mm, respectively. Finally, the green compacts were sintered at 800 °C for 30 min in argon-filled quartz tubes.

2.2. Materials characterization

The crystal structure of the samples on each step of the processing was studied at room temperature using a Panalytical Empyrean XRD equipment with CuKα radiation. A detailed description of crystallographic structure evaluation was included in our previous work [17–20,22].

The lattice parameters estimation as also phases quantitative analysis were based on the Rietveld profile fitting method realized on the High Score software. The following structural models were used: Ti(α) (ref. code 04-008-4973, Ti(β) (ref. code 04-019-3251), Ag (ref. code 04-016-1388), Ce (ref. code 04-012-9496), $Ti_{0.75}Mo_{0.25}$ (ref. code 04-013-0263), $Ti_{0.67}Mo_{0.33}$ (ref. code 04-017-8941), $Ti_{0.94}Mo_{0.06}$ (ref. code 04-017-1340), Ti_4P_3 (ref. code 04-002-5387), Ti_3P (ref. code 07-007-1166 and 04-002-5385).

Scanning electron microscope (SEM, VEGA 5135 Tescan) with energy dispersive spectrometer (EDS, PTG Prison Avalon) was applied to calculate the chemical composition and microstructure of the synthesized alloy and composites.

The porosity of the synthesized alloy and composites was calculated by the formula $P=(1 - \rho/\rho_{th}) \times 100\%$ (ρ and ρ_{th} - the density of the porous material and its corresponding theoretical density calculated for the rule of the mixtures). Additionally, the density of the sinters was calculated by the Archimedes method.

The Vickers hardness ($HV_{0.3}$) was measured using a microhardness tester by applying a load of 300 g for 10 s on the polished surfaces of the samples. Ten separate indents were created on the investigated surface of each sample for the statistics.

Indentation Martens Hardness (HM) and Young modulus (E) of the non-etched Ti31Mo alloy and its composites, were evaluated using a CSM Instruments nanoindenter with the Berkovich diamond tip [28]. E Modulus testing calculated from the slope of the tangent for the calculation of indentation hardness following the method given by Oliver and Pharr [29], carried out on the samples by four-sided Vickers diamond indenter with an ISO 14577 standard for measurement parameters as follows F = 0.3 N/20 s and C = 5.0 s.

A detailed description of corrosion resistance measurements was previously described [27]. The surface of the sample was prepared by grinding in water up to 600 grit. The weight loss by

polarization was calculated using Faraday's law.

The contact angle (CA) of the synthesized materials was investigated by the optical system with a digital camera (Kruss-DSA25) and estimated by software (Kruss-Advanced 1.5). A static surface contact angle measurements were carried out with glycerol (99.9%, Chemland, Poland) and diiodomethane (99.9%, Chemland, Poland) testing fluids. A detailed description of measurements was included in our previous works [27,30].

2.3. Assessment of biofilm formation inhibition

In this study, the *Staphylococcus aureus* (ATCC 6538) strain was assessed. *S. aureus* was obtained from commercial sources (American Type Culture Collection). A detailed description of the assessment of biofilm formation inhibition was previously presented [31]. The surface spread method and quantitative dilutions were applied to asses bacterial adherence, after 4 h and 20 h, respectively to the experimental biomaterial surfaces. All experiments were repeated three times.

Statistical software R version 3.0.1 was applied to determine whether any significant difference existed in bacterial number in the antibacterial experiments. Analysis of variance (ANOVA) followed by Tukey's honest significant difference (HSD) test was performed on the bacterial counts. The statistical significance was defined as $p < 0.05$.

3. Results

In the present work, bulk ultrafine-grained Ti31MoxHA and Ti31Mo5HA with 1 wt % Ag, 2 wt % Ta_2O_5 or 2 wt % CeO_2 composites were synthesized by MA and powder metallurgy route. The influence of microstructure and chemical composition of Ti31MoHA based composite on the crystal structure, microstructure, mechanical properties, corrosion behavior, surface wettability and antibacterial activity against *S. aureus* was evaluated.

3.1. Structure properties

The crystal structure change of Ti31Mo alloy during mechanical alloying by XRD method was studied earlier [17]. The sintered Ti31Mo alloy (800 °C/0.5 h) showed only two phases: a major Ti(β) -type phase with the cell parameter a = 3.2373 Å and a minor Ti(α)-type phase with cell parameters a = 2.9704 Å and c = 4.7716 Å. The Ti31Mo alloy produced by the application of hot pressing at 800 °C in vacuum approach, allows forming the single β-type alloy [17].

The evolution of crystallographic structures of Ti31MoxHA composites during mechanical alloying was studied by the XRD method, too (Fig. 1). The characteristic (hkl) lines of Ti and Mo are not visible even after 15 min of MA, but in the case of Ti31Mo10HA only (hkl) lines of HA can be detected after 15 min of MA (see Fig. 1 c). After 5 h of MA, for all HA concentrations, except the α-type phase, the β-type phase was detected. Additionally, in the case of Ti31Mi2.5HA composite after 39 h of MA single Ti(β) (110) phase material was formed. During MA, cold welding and alloying of starting powder substrates proceed at the solid-state. High energy transfer to the substrate powders during MA results in a high density of defects and dislocation. The particle size and strain values evaluated by the Williamson–Hall Uniform Deformation Model (UDM) approach from the slope of the plots and intercept depictured on Fig. 2 of Ti31MoxHA samples after 39 h of MA, where gathered in Table 1. The negative slope indicates the compressive strain experienced by the particles in the case of Ti31Mo2.5HA composite.

Formation of the bulk ultrafine-grained composites was achieved by cold uniaxial pressing and sintering of the MA powders at a temperature of 800 °C for 0.5 h at argon atmosphere (see Fig. 3). XRD analysis of Ti31Mo2.5HA composite showed the presence of regular phases (total 70.3%): $Ti_{0.75}Mo_{0.25}$, (44.9%), $Ti_{0.67}Mo_{0.33}$ (24.3%), β-Ti (1.1%) with minor hexagonal α-Ti (17.8%) phase and Ti_3P (11.9%). In Ti31Mo5HA composite, except the major β-type phases (61.1%), the α-Ti (24.3%) and Ti_3P (14.6%) and for Ti31Mo10HA composite α-Ti (29.0%), $Ti_{0.67}Mo_{0.33}$ (13.8%), Ti_3P (13.5%), $Ti_{0.94}Mo_{0.06}$ (34.0%) and β-Ti (9.7%) were detected (see Table 2). As it could be seen from the structural data, the HA decomposition during MA process appears, its manifests in sinters as a Ti_3P phase presence, as also what was confirmed, an influence on a primary phase relation. Higher HA addition to the main composition influences the growing α-Ti phase volumetric amount and change the element relation in the bcc phase formation mechanism. For instance, a higher HA amount influence the beta type phase solution relation, which for a titanium base stays a dominant one alike in $Ti_{0.94}Mo_{0.06}$ or oppositely for $Ti_{0.75}Mo_{0.25}$ where a molybdenum amount arises in a cell volume with simultaneous rearrangement of the transition $Ti_{0.67}Mo_{0.33}$ phase.

The volume of the regular structure of Ti31Mo alloy decreases by the modification of its chemical composition by hydroxyapatite. The shift of the main diffraction peaks of the (hkl) crystal planes towards larger angles was observed in comparison with pure Ti31Mo alloy. The porosity of synthesized composites increases with an increase of *x* in Ti31MoxHA (Table 3, Fig. 4). It is important to note that the final phases content and porosity of so produced bulk materials remain sensitive to the amount of HA in the Ti31Mo alloy. The structural parameters of produced Ti31MoxHA composites are summarized in Table 2.

The bulk Ti31MoxHA composites produced by cold pressing and sintering were composed of irregular particles and show a porous microstructure (Fig. 4, Table 3). Porosity depends strongly on the chemical composition of synthesized composites. The composite surfaces were presented in Fig. 4 with their elements mapping (Fig. 4 a, b, c). The obtained results confirmed the chemical composition of synthesized composites.

The SEM view of composites presented in Fig. 4, shows independently phase-contrast relation and microstructure size range. As could be observed from the analysis, the etching agent reaction characterizes different surface respond due to a starting composition. The predominant effect that could be observed remains connected to the HA content that influences porosity and final phase relation. Visible aggregation, local interactions, and porosity appearance however homogenously distributed in the final microstructure corresponds to a changeable analyzed in the further steps surface properties relation.

Formation of the bulk ultrafine-grained of Ti31Mo5HA with 1 wt % Ag, 2 wt % Ta_2O_5 or 2 wt % CeO_2 composites were achieved by cold uniaxial pressing and sintering of the MA powders at a temperature of 800 °C for 0.5 h at argon atmosphere (Fig. 5). The XRD analysis of synthesized composite with 1 wt % Ag, 2 wt % Ta_2O_5 and 2 wt% CeO_2 confirm the phase presence composed from the titanium regular ($Ti_{0.67}Mo_{0.33}$, $Ti_{0.75}Mo_{0.25}$, β-Ti) and hexagonal α-Ti forms as also other ones like Ti_3P, Ti_4P_3 related to HA addition. The content of α-Ti phase was about 21%. On the other hand, in synthesized composites, the total amounts of $Ti_{0.67}Mo_{0.33}$, $Ti_{0.75}Mo_{0.25}$ and β-Ti phases was 65.4, 54.6 and 74.5 for composites with 1 wt % Ag, 2 wt % Ta_2O_5 and 2 wt% CeO_2 contents, respectively. The structural parameters of produced Ti31MoxHA composites are summarized in Table 4. The porosity of synthesized composites was below 5% (Fig. 6, Table 5).

3.2. Mechanical properties

In Table 6 the hardness and Young modulus of the Ti31MoxHA composites were presented. The indentation hardness (HIT) and

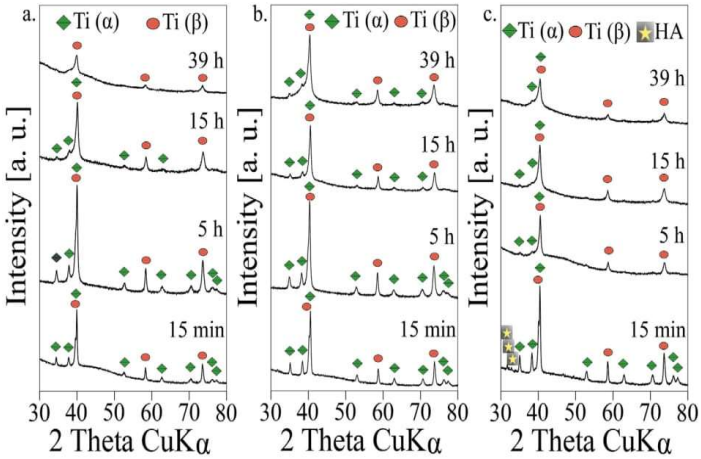

Fig. 1. XRD spectra of Ti31MoxHA: $x = 2.5$ (a), 5 (b), 10 (c) mechanically alloyed for different times.

indentation modulus (EIT) were evaluated from the indentations plots which were shown in Fig. 7. The room temperature load-displacement curves of synthesized composites confirmed in nearly all cases, lower than commercial pure Ti (α) modulus values (140 GPa), interpreted from the line course. For example in the case of the bulkTi31Mo5HA composite with the porosity 3.72% the Young modulus equals 100.91 GPa. The Vickers hardness for Ti31MoxHA composites reached 396, 347 and 363 $HV_{0.3}$ for x = 2.5, 5 and 10, respectively. These values are more than 2 times higher than that of pure microcrystalline Ti(α) (160 $HV_{0.3}$).

In the case of Ti31Mo5HA with 1 wt % Ag and 2 wt % CeO_2 composites Young's modulus (E) are around 95 GPa (Table 7, Fig. 8). For above the solid solution and/or precipitation strengthening mechanism remains involved with correspondence to introduced stress level and dislocations anchorage, which reduces grain growth at elevated temperatures. The mechanical alloying in the same results in structure refinement. Obtained after sintering smaller grains, increase the volume contribution of the grain boundaries in the whole volume of the material that finally corresponds to a higher strength.

Table 1
Particle size and strain factors determined by the Williamson-Hall UDM method based on the XRD spectra of Ti31MoxHA powders after 39 h of MA.

Ti31MoxHA	D [nm]	ε -
2.5	9.12	$-1.63 \cdot 10^{-3}$
5	26.66	$3.23 \cdot 10^{-3}$
10	23.11	$2.95 \cdot 10^{-3}$

3.3. Corrosion behavior

The examples of the polarization curves of Ti31MoxHA composites investigated in the Ringer solution at 37 °C are shown in Fig. 9 (Table 8). For the HA concentration x = 5 the corrosion current (I_{corr}) is $3.332 \cdot [\mu A \cdot cm^{-2}]$. The addition of 1 wt % Ag and 2 wt % CeO_2 to Ti31Mo5HA composite deteriorates the corrosion properties. On the other hand the addition of 2 wt % Ta_2O_5 has much more

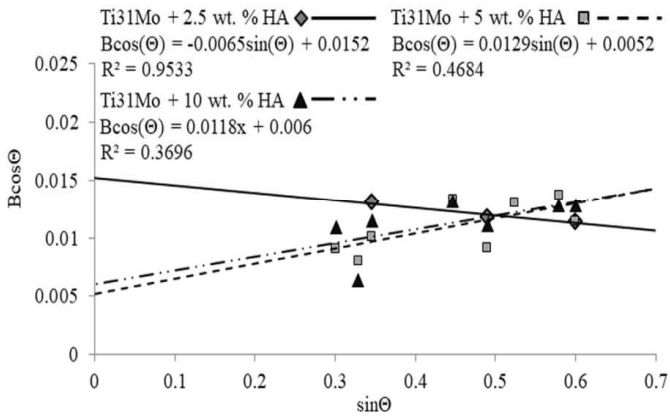

Fig. 2. The linear Williamson-Hall UDM plots based on the XRD spectra of Ti31MoxHA powder materials after 39 h of MA.

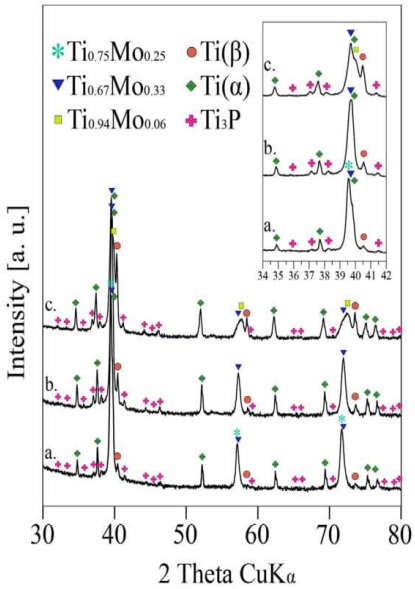

Fig. 3. XRD spectra of Ti31MoxHA: x = 2.5 (a), 5 (b), 10 (c) mechanically alloyed for 39 h and sintered at 800 °C/0.5 h.

better corrosion properties (I_{corr} = 6.293 [μA·cm^{-2}]); (Table 9, Fig. 10).

3.4. The surface wetting properties

The surface wetting properties such as the contact angles in diiodomethane and glycerol as well as estimated the surface free energy with its disperse and polar components of the synthesized Ti31MoxHA composites were presented in Table 10. Surface wettability assay recorded lower diiodomethane contact angles in the case of Ti31Mo5HA composite with 2 wt % CeO_2 (Table 11). For the hard tissue replacement applications, the high wetting properties remain crucial.

Table 3
Theoretical density (ρ_{th}), calculated density (ρ_{cal}) and porosity (P) of Ti31MoxHA composites.

Ti31MoxHA	ρ_{th} [g/cm^3]	ρ_{cal} [g/cm^3]	P [%]
2.5	7.142	6.992(21)	2.10(10)
5	7.048	6.785(57)	3.72(27)
10	6.871	6.359(32)	7.45(15)

3.5. Effect of Ag Ta_2O_5 or CeO_2 contents on the antibacterial activity of Ti31Mo5HA composite

Fig. 11 shows the results of viable bacteria adhered to the different experimental material surfaces when exposed to *S. aureus*. Bacterial adhesion was significantly reduced on the surface of Ti31Mo5HA1Ag and Ti31Mo5HA2CeO_2 composites compared to the microcrystalline titanium. These biomaterials were observed to have significantly lower adhesion levels ($p < 0.05$) of *S. aureus*, suggesting that these composites have inhibited biofilm formation. On the other hand, a lot of bacteria are found on the Ti31Mo, T31Mo5HA and Ti31Mo5HA2Ta_2O_5 composites, as shown in Fig. 11, displaying that these composites have low antibacterial activity against *S. aureus* (Table 12).

4. Discussion

Titanium-based composites have gained great scientific interest in their adjustable mechanical and corrosion properties. In consideration of biocompatibility, the reinforcement phases in Ti-based composites are usually hydroxyapatite, fluorapatite, resorbable calcium phosphates, silica, bioactive glasses and calcium [25].

Many different methods for producing ultrafine-grained structures are available. They are mainly based on the production of fine-grained powders (down the nanometer scale) and subsequent powder metallurgy for consolidation. In this work, the bulk ultrafine-grained Ti31MoxHA composites have been produced by consolidating the mechanically alloyed powders. The bulk Ti31Mo-type composites were produced by the application of cold uniaxial

Table 2
Phase amounts determined by the Rietveld method and structural parameters of Ti31MoxHA.

Ti31MoxHA			2.5	5	10
sig		–	2.56274	3.00599	3.2278
R_{wp}		[%]	6.68328	7.65377	7.97017
R_{exp}		[%]	2.60787	2.54617	2.46923
$Ti_{0.75}Mo_{0.25}$	A	[%]	**44.9**	**-**	**-**
	a	[Å]	3.223811	–	–
	V	[Å^3]	33.50494	–	–
Ti(α)	A	[%]	**17.8**	**24.3**	**29.0**
	a	[Å]	2.969040	2.97131	2.973551
	c	[Å]	4.769867	4.775368	4.780843
	V	[Å^3]	36.41405	36.51181	36.60885
$Ti_{0.67}Mo_{0.33}$	A	[%]	**24.3**	**57.4**	**13.8**
	a	[Å]	3.213758	3.214438	3.214171
	V	[Å^3]	33.19247	33.21353	33.20527
Ti(β)	A	[%]	**1.1**	**3.7**	**9.7**
	a	[Å]	3.144	3.146497	3.146145
	V	[Å^3]	31.07761	31.15173	31.14128
Ti_3P	A	[%]	**11.9**	**14.6**	**13.5**
	a	[Å]	9.954813	9.966627	9.99358
	c	[Å]	4.986428	4.992807	4.958161
	V	[Å^3]	494.14640	495.9537	495.1797
$Ti_{0.94}Mo_{0.06}$	A	[%]	–	–	**34.0**
	a	[Å]	–	–	3.187645
	V	[Å^3]	–	–	32.38992

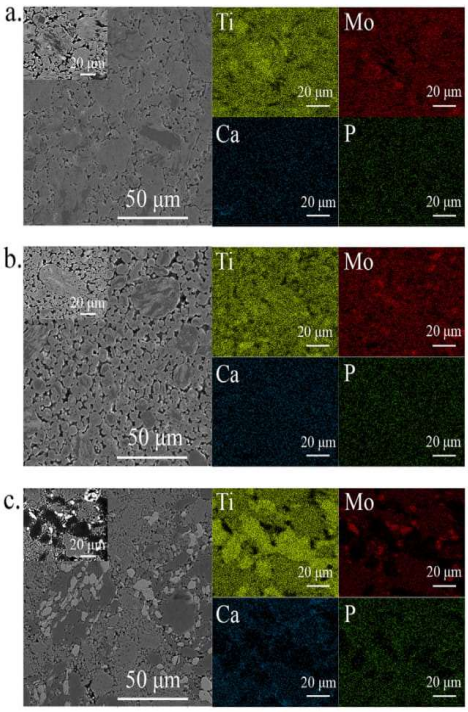

Fig. 4. SEM micrographs, EDS mapping of the Ti, Mo, Ca and P distribution of Ti31Mo with *x* HA: *x* = 2.5 (a), 5 (b), 10 (c) mechanically alloyed for 39 h and sintered at 800 °C/0.5 h.

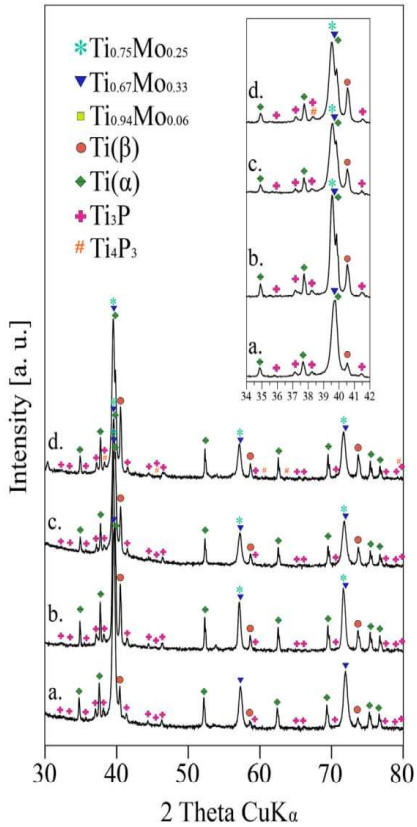

Fig. 5. XRD spectra of Ti31Mo5HA (a) with 1 wt % Ag (b), 2 wt % Ta_2O_5 (c), 2 wt % CeO_2 (d) mechanically alloyed for 39 h and sintered at 800 °C/0.5 h.

pressing and sintering of the MA powders.

The influence of chemical composition on the microstructure, mechanical properties and corrosion behavior of bulk Ti31MoxHA composites were discussed. Chemical modification of the Ti31Mo alloy by 5 wt% of HA led to the obtainment of a composite with a different properties relation. The higher average values of the Vickers hardness (396 $HV_{0.3}$) characterize the Ti31Mo2.5HA composite. The Young modulus and hardness of the ultrafine-grained Ti31Mo5HA composite were found to be 101 GPa and 347 $HV_{0.3}$, respectively.

The effect of the initial chemical composition on the microstructure and properties of Ti-HA composites was studied previously [20]. Due to the refinement of the microstructure, the hardness of titanium-reinforced with 10 vol % of HA reached 1500 $HV_{0.2}$; the hardness of microcrystalline Ti is 250 $HV_{0.2}$.

It is well known that the mechanical properties of Ti-based alloys can be enhanced by the refinement of microstructure to the ultrafine regime. In this case, enhanced strength and ductility and reduced tension-compression yield asymmetry can be measured [32,33].

Due to the corrosive environment of the body fluids, the synthesized composites may undergo unexpected corrosion and finally can lead to a release of the corrosion products to the tissue. The ultrafine-grained Ti31Mo alloy possesses a lower corrosion resistance and consequently a higher corrosion current density (I_{corr} = 14.40 [$\mu A \cdot cm^2$], E_{corr} = −0.94 [V]) in the Ringer solutions. The modification of the chemical composition of Ti31Mo alloy by HA addition for the x concentrations equals 2.5 and 5 improves corrosion resistance. Additionally, the bulk Ti31Mo5HA2Ta_2O_5 composite has also good corrosion properties (I_{corr} = 6.293 [$\mu A \cdot cm^{-2}$], E_{corr} = 0.687 [V])).

The surface wettability and by above surface free energy relations remain a key parameter for the osteoblastic proliferation activity [34,35] which for improved surface wettability enhanced the cellular adhesion.

In the present research, the ability of *S. aureus* to form biofilm on ultrafine-grained Ti31Mo alloy and subjected to the different types of chemical modifications, including Ag, Ta_2O_5 or CeO_2 was evaluated. *S. aureus* is a Gram-positive bacterium that is a member of the Firmicutes, and it is a usual member of the microbiota of the body. Additionally, this bacterium is the leading etiologic agent of limb and life-threatening biofilm-related infections in the patients following any implantations.

The obtained results indicate that the tested *S. aureus* strain is able to adhere to the Ti31Mo5HA composites produced by the powder metallurgical method. Additionally, the type of chemical modification (Ag, Ta_2O_5 or CeO_2) influences the ability of *S. aureus* to form biofilm on the tested biomaterial.

According to published research, when a Ti31Mo5HAAg composite stays immersed in body fluid, the silver could react with the environment and release ionized Ag into the surrounding [36]. A release of the silver biocide at a concentration level (0.1 ppb) is

Table 4
Phase amounts determined by the Rietveld method and structural parameters of Ti31Mo5HA with 1 wt % Ag, 2 wt % Ta_2O_5 and 2 wt % CeO_2 mechanically alloyed for 39 h and sintered at 800 °C/0.5 h.

sample			Ti31Mo5HA1Ag	Ti31Mo5HA2Ta_2O_5	Ti31Mo5HA2CeO_2
sig		–	2.95171	2.4587	3.79002
R_{wp}		[%]	7.45910	6.05492	9.80756
R_{exp}		[%]	2.52704	2.46265	2.58773
$Ti_{0.67}Mo_{0.33}$	A	[%]	**9.4**	**18.8**	**15.2**
	a	[Å]	3.213202	3.215359	3.217825
	V	[Å^3]	33.17525	33.2421	33.31864
Ti(α)	A	[%]	**21.5**	**20.3**	**20.7**
	a	[Å]	2.967743	2.967486	2.96785
	c	[Å]	4.767614	4.766392	4.767345
	V	[Å^3]	36.36505	36.34943	36.36562
$Ti_{0.75}Mo_{0.25}$	A	[%]	**46.8**	**36.3**	**45.6**
	a	[Å]	3.224589	3.225721	3.228327
	V	[Å^3]	33.52918	33.56452	33.64593
Ti(β)	A	[%]	**9.2**	**9.5**	**13.7**
	a	[Å]	3.146462	3.145521	3.145865
	V	[Å^3]	31.15068	31.12273	31.13294
Ti_3P	A	[%]	**13.1**	**15.1**	**4.5**
	a	[Å]	9.95885	9.965362	9.960789
	c	[Å]	4.997669	4.985011	4.995629
	V	[Å^3]	495.6658	495.0536	495.6529
Ti_4P_3	A	[%]	–	–	**0.3**
	a	[Å]	–	–	7.425
	V	[Å^3]	–	–	409.3449

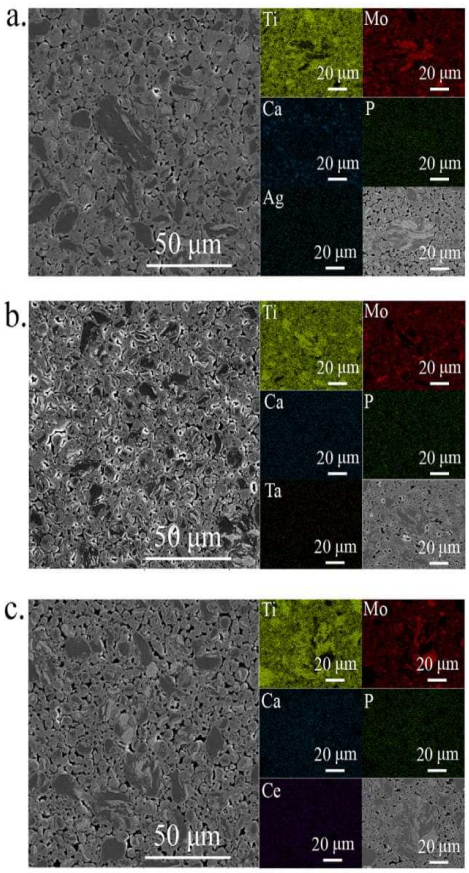

Fig. 6. SEM micrographs, EDS mapping of the Ti, Mo, Ca and P distribution of Ti31Mo5HA with 1 wt % Ag (a), 2 wt % Ta_2O_5 (b), 2 wt % CeO_2 (c) mechanically alloyed for 39 h and sintered at 800 °C/0.5 h.

Table 5
Theoretical density (ρ_{th}), calculated density of the porous material (ρ_{cal}) and porosity (P) of Ti31Mo5HA with 1 wt % Ag, 2 wt % Ta_2O_5, 2 wt % CeO_2.

sample	ρ_{th} [g/cm^3]	ρ_{cal} [g/cm^3]	P [%]
Ti31Mo5HA	7.048	6.79(57)	3.72(27)
Ti31Mo5HA1Ag	7.082	6.81(12)	3.83(54)
Ti31Mo5HA2Ta_2O_5	7.070	6.72(08)	4.97(39)
Ti31Mo5HA2CeO_2	7.051	6.77 (18)	4.02(87)

Table 6
Vickers hardness ($HV_{0.3}$), Martens hardness (HM) and Young's modulus (E) of Ti31MoxHA composites.

Ti31MoxHA	$HV_{0.3} \pm \sigma$	HM $\pm \sigma$ [N/mm^2]	E $\pm \sigma$ [GPa]
2.5	396 ± 24	3800.01 ± 600.50	115.83 ± 11.71
5	347 ± 30	3107.00 ± 635.33	100.91 ± 13.19
10	363 ± 25	3032.09 ± 469.41	101.69 ± 13.01

capable of rendering antibacterial efficacy [36,37].

The mechanism for bacterial toxicity of tested Ti31Mo5HAAg alloy may include free metal ion toxicity arising from the dissolution of metals from the surface of the silver particles (e.g., $Ag+$ from Ag) [37,38] or oxidative stress via the generation of reactive oxygen species (ROS) on crystal surfaces of some nanoparticles [39]. Other mechanisms, which mainly include changes in bacterial cell wall permeability, removal of antimicrobial agents through efflux pumps of the membrane, drug action site modification, antimicrobial agent's inactivation, etc., should be considered [40].

Titanium remain mostly neutral and for shore not poisonous for the human body environment which can tolerate this metal in large doses. Therefore, the composites based on the Ti containing hydroxyapatite and Ag additions have the potential to be used in medicine with the infection control. Information on the acute toxicity of molybdenum and molybdenum compounds to humans is not available [41].

The results of this research show that Ta_2O_5 fail to inhibit bacterial growth and biofilm formation of *S. aureus* studied on Ti31Mo5HA composite. Recently, *in vitro* antibacterial activity of

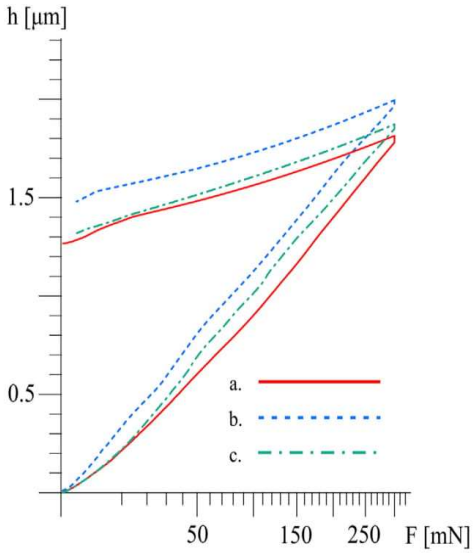

Fig. 7. Depth - load (h-F) nanoindentation curves of Ti31MoxHA: x = 2.5 (a), 5 (b), 10 (c) mechanically alloyed for 39 h and sintered at 800 °C/0.5 h.

Table 7
Vickers hardness ($HV_{0.3}$), Martens hardness (HM) and Young's modulus (E) of Ti31Mo5HA with 1 wt % Ag, 2 wt % Ta_2O_5, 2 wt % CeO_2.

sample	$HV_{0.3} \pm \sigma$	$HM \pm \sigma$ [N/mm^2]	$E \pm \sigma$ [GPa]
Ti31Mo5HA1Ag	253 ± 11	2337.92 ± 275.76	94.94 ± 6.64
Ti31Mo5HA2Ta_2O_5	379 ± 29	3264.73 ± 1252.12	102.45 ± 30.00
Ti31Mo5HA2CeO_2	315 ± 10	3125.84 ± 610.37	95.06 ± 19.38

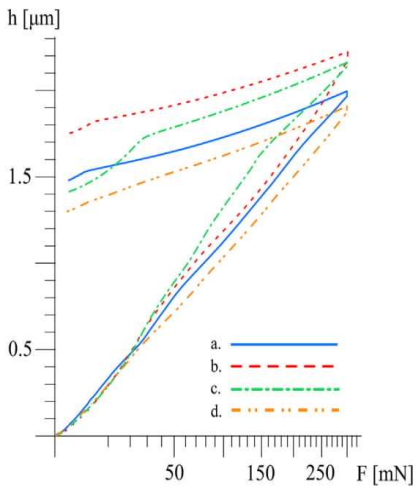

Fig. 8. Depth - load (h-F) nanoindentation curves of Ti31Mo5HA (a) with: 1 wt % Ag (b), 2 wt % Ta_2O_5 (c), 2 wt % CeO_2 (d).

that Ta_2O_5 doped glass-ceramic (40-x)SiO_2-24.4 Na_2O-26.9 CaO-6.1 CaF_2-2.6 P_2O_5—xTa_2O_5 against pathogenic bacteria was investigated [42]. It was found that ceramic samples showed statistically significant ($p < 0.05$) antibacterial activity against the following gram-positive bacteria: *Streptococcus pyogenes, Bacillus subtilis and*

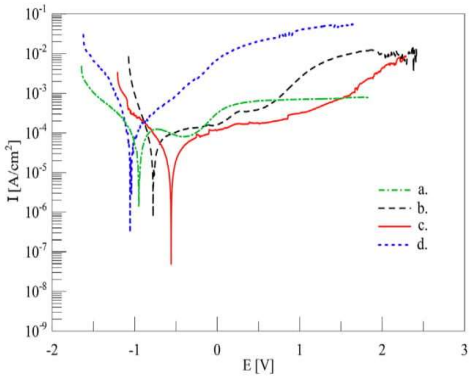

Fig. 9. Potentiodynamic polarization curves of Ti31Mo (a) and Ti31MoxHA composites: x = 2.5 (b), 5 (c), 10 (d).

Table 8
Corrosion potential (E_{corr}), current density (I_{corr}) of Ti31MoxHA composites.

Ti31MoxHA	E_{corr} [V]	I_{corr} [μA·cm^{-2}]
0	−0.940	14.40
2.5	−0.771	5.386
5	−0.562	3.332
10	−1.040	12.89

Table 9
Corrosion potential (E_{corr}) and current density (I_{corr}) of Ti31Mo5HA with 1 wt % Ag, 2 wt % Ta_2O_5, 2 wt % CeO_2.

sample	E_{corr} [V]	I_{corr} [μA·cm^{-2}]
Ti31Mo5HA	−0.562	3.332
Ti31Mo5HA1Ag	−0.834	13.17
Ti31Mo5HA2Ta_2O_5	−0.687	6.293
Ti31Mo5HA2CeO_2	−0,863	30.49

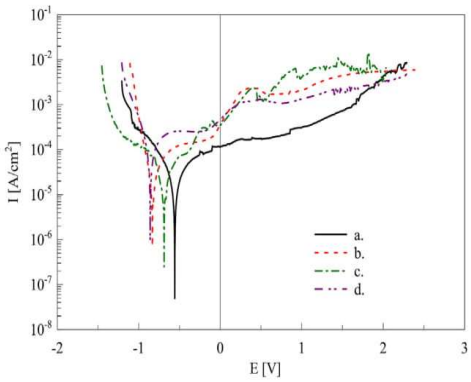

Fig. 10. Potentiodynamic polarization curves of Ti31Mo5HA (a) with 1 wt % Ag (b), 2 wt % Ta_2O_5 (c), 2 wt % CeO_2 (d).

Staphylococcus epidermidis.

The Ti31Mo5Ha2CeO_2 composite showed the highest antibacterial activity against *S. aureus*. The biofilm formation was reduced by RF 98.9% in comparison to microcrystalline titanium. Recent

Table 10
Contact angle (CA), surface free energy, disperse and polar for Ti31MoxHA.

Ti31MoxHA	Diiodomethane CA[°]	Glycerol CA[°]	Surface free energy [mN/m]	Disperse [mN/m]	Polar [mN/m]
0	58.76 ± 4.54	50.12 ± 1.39	43.16 ± 0.37	29.29 ± 2.61	13.87 ± 2.87
2.5	56.64 ± 12.12	46.41 ± 11.84	46.57 ± 5.97	30.49 ± 6.92	16.08 ± 10.48
5	53.55 ± 3.87	51.64 ± 6.82	42.98 ± 4.39	32.26 ± 2.20	10.71 ± 2.54
10	54.55 ± 1.18	40.73 ± 11.65	49.18 ± 6.60	33.70 ± 3.95	17.47 ± 6.99

studies showed that the cerium oxide nanoparticles with antimicrobial activity against *Escherichia coli* adsorb to the bacteria surface but do not penetrate the cell [43]. This research is in good agreement with Thill et al. [44], who suggested three types of interaction between bacteria and Ce nanoparticles: adsorption, oxi-reduction, and toxicity.

Ultrafine-grained Ti–31Mo5HA-based composites possess unique mechanical properties and are thus considered to represent the future generation of biomaterials. Additionally, the addition of the Ag or CeO_2 to Ti31Mo5HA composite has significantly lower adhesion of *S. aureus*, suggesting that these composites had antibacterial activity.

5. Conclusions

In this study, the influence of microstructure and chemical composition of ultrafine-grained Ti31MoxHA and Ti31Mo5HA/Ag (or Ta2O5, CeO2) composites on the phase transitions (α→β), microstructure, mechanical properties, corrosion behavior, surface wettability and antibacterial activity against *S. aureus* was investigated in detail. An improvement of the properties due to the ultrafine-grained composite structure was observed.

Summarizing, the following conclusions can be drawn:

- the XRD analysis of Ti31Mo2.5HA composite showed the presence of regular phases (total 70.3%): Ti0.75Mo0.25, (44.9%), Ti0.67Mo0.33 (24.3%), β-Ti (1.1%) with minor hexagonal α-Ti (17.8%) phase and Ti3P (11.9%). In Ti31Mo5HA composite, except the major β-type phases (61.1%), the α-Ti (24.3%) and Ti3P (14.6%) and for Ti31Mo10HA composite α-Ti (29.0%), Ti0.67Mo0.33 (13.8%), Ti3P (13.5%), Ti0.94Mo0.06 (34.0%) and β-Ti (9.7%) were detected (see Table 2).
- the XRD analysis of synthesized composite with 1 wt % Ag, 2 wt % Ta2O5 and 2 wt% CeO2 confirmed the phase presence composed from the titanium regular (Ti0.67Mo0.33, Ti0.75Mo0.25, β-Ti) and hexagonal α-Ti forms as also other ones like Ti3P, Ti4P3 related to HA addition. The content of α-Ti phase was about 21%. On the other hand, in synthesized composites, the total amounts of Ti0.67Mo0.33, Ti0.75Mo0.25 and β-Ti phases were 65.4, 54.6 and 74.5 for composites with 1 wt % Ag, 2 wt % Ta2O5 and 2 wt% CeO2 contents, respectively,
- the ultrafine-grained composites possessed higher Vickers hardness,
- in the case of Ti31Mo5HA with 1 wt % Ag and 2 wt % CeO2 composites Young's modulus was around 95 GPa,

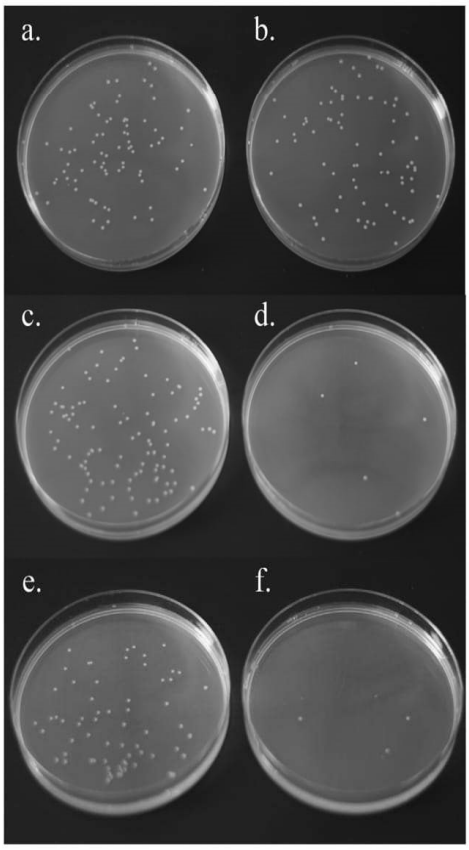

Fig. 11. Antibacterial activity against *S. aureus* (ATCC 6538) growth on agar plates after 24 h incubation on different composites: (a) control (Ti), (b) Ti31Mo, (c) Ti31Mo5HA, (d) Ti31Mo5HA1Ag, (e) Ti31Mo5HA2Ta_2O_5 (f) Ti31Mo5HA2CeO_2.

- the corrosion resistance analysis indicated a dependence of the obtained results on the material's chemical composition,
- surface wettability assay recorded lower diiodomethane contact angles in the case of Ti31Mo5HA composite with 2 wt % CeO2,
- the Ti31Mo5HA1Ag and Ti31Mo5HA2CeO2 composites have significantly lower adhesion levels of *S. aureus* ($p < 0.05$).

Table 11
Contact angle (CA), surface free energy, disperse and polar for Ti31Mo5HA with 1 wt % Ag, 2 wt % Ta_2O_5, 2 wt % CeO_2.

sample	Diiodomethane CA[°]	Glycerol CA[°]	Surface free energy [mN/m]	Disperse [mN/m]	Polar [mN/m]
Ti31Mo5HA1Ag	62.11 ± 5.28	49.12 ± 12.14	43.46 ± 8.19	27.37 ± 3.03	16.10 ± 5.17
Ti31Mo5HA2Ta_2O_5	48.27 ± 5.87	59.99 ± 20.29	42.01 ± 7.89	35.19 ± 3.18	2.29 ± 1.88
Ti31Mo5HA2CeO_2	47.39 ± 9.09	54.08 ± 5.08	43.35 ± 2.75	35.60 ± 4.93	7.75 ± 3.79

Table 12
Antibacterial activity evaluated using reduction factor (RF) of composites against *S. aureus*.

sample	CFU/mL		RF %
	after 4 h of incubation	after 20 h of incubation	
microcrystalline Ti (control)	$<1.0\cdot10^3$	$2.0\cdot10^5$	–
Ti31Mo	$<1.0\cdot10^3$	$3.5\cdot10^4$	82.5
Ti31Mo5HA	$<1.0\cdot10^3$	$4.0\cdot10^4$	80
Ti31Mo5HA1Ag	$<1.0\cdot10^3$	$5.0\cdot10^3$	97.5
Ti31Mo5HA2Ta_2O_5	$<1.0\cdot10^3$	$3.5\cdot10^4$	82.5
Ti31Mo5HA2CeO_2	$<1.0\cdot10^3$	$2.2\cdot10^3$	98.9

The ultrafine-grained Ti31Mo5HA - Ag or CeO2 biomaterials may offer new structural and functional properties for innovative medical implant applications.

Declaration of competing interest

The authors declare that they have no known competing financial interests or personal relationships that could have appeared to influence the work reported in this paper.

Acknowledgments

The work was financed by the National Science Centre Poland under the decision no.: DEC-2017/25/B/ST8/02494.

References

[1] M. Navarro, A. Michiardi, O. Castaño, J.A. Planell, Biomaterials in orthopedics, J. R. Soc. Interface 5 (2008) 1137–1158, https://doi.org/10.1098/rsif.2008.0151.
[2] J.W. Park, Y.J. Kim, C.H. Park, D.H. Lee, Y.G. Ko, J.H. Jang, C.S. Lee, Enhanced osteoblast response to an equal channel angular pressing-processed pure titanium substrate with microrough surface topography, Acta Biomater. 5 (2009) 3272–3280, https://doi.org/10.1016/j.actbio.2009.04.038.
[3] M. Niinomi, Recent research and development in titanium alloys for biomedical applications and healthcare goods, Sci. Technol. Adv. Mater. 4 (2003) 445–454, https://doi.org/10.1016/j.stam.2003.09.002.
[4] D. Kuroda, M. Niinomi, M. Morinaga, Y. Kato, T. Yashiro, Design and mechanical properties of new beta type titanium alloys for implant materials, Mater. Sci. Eng. A 243 (1998) 244–249, https://doi.org/10.1016/S0921-5093(97)00808-3.
[5] O. Okuno, Titanium alloys for dental applications, J. Jpn. Soc. Biomater. 14 (1996) 267–273.
[6] H. Matusiewicz, Potential release of in vivo trace metals from metallic medical implants in the human body: from ions to nanoparticles – a systematic analytical review, Acta Biomater. 10 (2014) 2379–2403, https://doi.org/10.1016/j.actbio.2014.02.027.
[7] A.D. Pye, D.E. Lockhart, M.P. Dawson, A.A. Murray, A.J. Smith, A review of dental implants and infection, J. Hosp. Infect. 72 (2009) 104–110, https://doi.org/10.1016/j.jhin.2009.02.010.
[8] I.H. Yang, S.Y. Kim, H.E. Rubash, A.S. Shanbhag, Fabrication of submicron titanium-alloy particles for biological response studies, J. Biomed. Mater. Res. 48 (1999) 220–223, https://doi.org/10.1002/(SICI)1097-4636(1999)48:3<220::AID-JBM4>3.0.CO;2-P.
[9] E. Kobayashi, H. Doi, M. Takahashi, T. Nakano, T. Yoneyama, H. Hamanaka, Castability and mechanical properties of Ti-6Al-7Nb alloy dental-cast, J. Jpn. Soc. Dent. Mater. Devices 14 (1995) 406–413.
[10] S. Ankem, C.A. Greene, Recent developments in microstructure/property relationships of beta titanium alloys, Mater. Sci. Eng. A 263 (1999) 127–131, https://doi.org/10.1016/S0921-5093(98)01170-8.
[11] D.J. Lin, C.C. Chuang, J.H. Chern Lin, J.W. Lee, C.P. Ju, H.S. Yin, Bone formation at the surface of low modulus Ti–7.5Mo implants in rabbit femur, Biomaterials 28 (2007) 2582–2589, https://doi.org/10.1016/j.biomaterials.2007.02.005.
[12] W.F. Ho, C.P. Ju, J.H. Chern Lin, Structure and properties of cast binary Ti–Mo alloys, Biomaterials 20 (1999) 2115–2122, https://doi.org/10.1016/S0142-9612(99)00114-3.
[13] X. Zhao, M. Niinomi, M. Nakai, J. Hieda, Beta type Ti–Mo alloys with changeable Young's modulus for spinal fixation applications, Acta Biomater. 8 (2012) 1990–1997, https://doi.org/10.1016/j.actbio.2012.02.004.
[14] W.D. Zhang, Y. Liu, H. Wu, M. Song, T.Y. Zhang, X.D. Lan, T.H. Yao, Elastic modulus of phases in Ti-Mo alloys, Mater. Char. 106 (2015) 302–307, https://doi.org/10.1016/j.matchar.2015.06.008.
[15] A. Almeida, D. Gupta, C. Loable, R. Vilar, Laser-assisted synthesis of Ti–Mo alloys for biomedical applications, Mater. Sci. Eng. C 32 (2012) 1190–1195, https://doi.org/10.1016/j.msec.2012.03.007.
[16] J.L. Murray, The Mo-Ti (Molybdenum-Titanium) system, Bull. Alloy Phase Diagrams 2 (1981) 185–192, https://doi.org/10.1007/BF02881476.
[17] P. Sochacka, A. Miklaszewski, M. Jurczyk, Development of <beta> type Ti-x at. % Mo alloys by mechanical alloying and powder metallurgy: phase evolution and mechanical properties ($10 \leq x \leq 35$), J. Alloy. Comp. 776 (2019) 370–378, https://doi.org/10.1016/j.jallcom.2018.10.217.
[18] M.U. Jurczyk, K. Jurczyk, A. Miklaszewski, M. Jurczyk, Nanostructured titanium-45S5 Bioglass scaffold composites for medical applications, Mater. Des. 32 (2011) 4882–4889, https://doi.org/10.1016/j.matdes.2011.06.005.
[19] A. Miklaszewski, M.U. Jurczyk, M. Kaczmarek, A. Paszel-Jaworska, A. Romaniuk, N. Lipinska, J. Zurawski, P. Urbaniak, M. Jurczyk, Nanoscale size effect in in situ titanium based composites with cell viability and cytocompatibility studies, Mater. Sci. Eng. C 73 (2017) 525–536, https://doi.org/10.1016/j.msec.2016.12.100.
[20] K. Niespodziana, K. Jurczyk, J. Jakubowicz, M. Jurczyk, Fabrication and properties of titanium – hydroxyapatite nanocomposites, Mater. Chem. Phys. 123 (2010) 160–165, https://doi.org/10.1016/j.matchemphys.2010.03.076.
[21] M. Jurczyk, Bionanomaterials for Dental Applications, Pan Stanford Publishing, Singapore, 2012.
[22] M. Tulinski, M. Jurczyk, Nanostructured nickel-free austenitic stainless steel composites with different content of hydroxyapatite, Appl. Surf. Sci. 260 (2012) 80–83, https://doi.org/10.1016/j.apsusc.2012.07.071.
[23] Q. Meng, S. Guo, Q. Liu, L. Hu, X. Zhao, A β-type TiNbZr alloy with low modulus and high strength for biomedical applications, Prog. Nat. Sci. Mater. Int. 24 (2014) 157–162, https://doi.org/10.1016/j.pnsc.2014.03.007.
[24] G. Adamek, M. Kozlowski, M.U. Jurczyk, P. Wirstlein, J. Zurawski, J. Jakubowicz, Formation and properties of biomedical Ti-Ta foams prepared from nanoprecursors by thermal dealloying process, Materials 12 (2019) 2668–2676, https://doi.org/10.3390/ma12172668.
[25] W. P Cao, L. Hench, Bioactive materials, Ceram. Int. 22 (1996) 493–507.
[26] K. Jurczyk, A. Miklaszewski, M.U. Jurczyk, M. Jurczyk, Development of β type Ti23Mo-45S5 Bioglass nanocomposites for dental applications, Materials 8 (2015) 8032–8046, https://doi.org/10.3390/ma8125441.
[27] P. Sochacka, A. Miklaszewski, K. Kowalski, M. Jurczyk, Influence of the processing method on the properties of Ti-23 at.% Mo alloy, Metals 9 (2019) 931–947, https://doi.org/10.3390/met9090931.
[28] A.C. Fischer-Cripps, Nanoindentation, third ed., Springer-Verlag, New York, 2011.
[29] W.C. Oliver, G.M. Pharr, An improved technique for determining hardness and elastic-modulus using load and displacement sensing indentation experiments, J. Mater. Res. 7 (1992) 1564–1583, https://doi.org/10.1557/JMR.1992.1564.
[30] A. Miklaszewski, K. Kowalski, M. Jurczyk, Hydrothermal surface treatment of biodegradable Mg-materials, Metals 8 (2018) 894–907, https://doi.org/10.3390/met8110894.
[31] K. Jurczyk, M.M. Kubicka, M. Ratajczak, M.U. Jurczyk, K. Niespodziana, D.M. Nowak, M. Gajecka, M. Jurczyk, Antibacterial activity of nanostructured Ti-45S5 bioglass-Ag composite against *Streptococcus mutans* and *Staphylococcus aureus*, Trans. Nonferrous Metals Soc. China 26 (2016) 118–125, https://doi.org/10.1016/S1003-6326(16)64096-7.
[32] H.Z. Ye, X.Y. Liu, Review of recent studies in magnesium matrix composites, J. Mater. Sci. 39 (2004) 6153–6171, https://doi.org/10.1023/B:JMSC.0000043583.47148.31.
[33] Z.C. Cordero, B.E. Knight, C.A. Schuh, Six decades of the Hall–Petch effect – a survey of grain-size strengthening studies on pure metals, Int. Mater. Rev. 61 (2016) 495–512, https://doi.org/10.1080/09506608.2016.1191808.
[34] T.J. Webster, J.U. Ejiofor, Increased osteoblast adhesion on nanophase metals: Ti, Ti6Al4V, and CoCrMo, Biomaterials vol. 25 (2004) 4731–4739, https://doi.org/10.1016/j.biomaterials.2003.12.002.
[35] K. Jurczyk, U. Braegger, M. Jurczyk, Nanotechnology in dental implants, in: M. van de Voorde (Ed.), Nanoscience and Nanotechnology - Advances and Developments in Nano-Sized Materials, De Guyter, Berlin, 2018, pp. 57–74.
[36] R. Kumar, H. Münstedt, Silver ion release from antimicrobial polyamide/silver composites, Biomaterials 26 (2005) 2081–2088, https://doi.org/10.1016/j.biomaterials.2004.05.030.
[37] C.S. Ciobanu, F. Massuyeau, L.V. Constantin, D. Predoi, Structural and physical properties of antibacterial Ag-doped nano-hydroxyapatite synthesized at 100 °C, Nanoscale Res. Lett. 6 (2011) 613–620, https://doi.org/10.1186/1556-

276X-6-613.
[38] J.S. Kim, E. Kuk, K.N. Yu, J.H. Kim, S.J. Park, H.J. Lee, S.H. Kim, Y.K. Park, Y.H. Park, C.Y. Hwang, et al., Antimicrobial effects of silver nanoparticles, Nanomedicine 3 (2007) 95–101, https://doi.org/10.1016/j.nano.2006.12.001.
[39] M.S. Wong, W.C. Chu, D.S. Sun, H.S. Hung, J.H. Chen, P.J. Tsai, N.T. Lin, M.S. Yu, S.F. Hsu, S.L. Wang, et al., Visible-light-induced bactericidal activity of a nitrogen-doped titanium photocatalyst against human pathogens, Appl. Environ. Microbiol. 72 (2006) 6111–6116, https://doi.org/10.1128/AEM.02580-05.
[40] J.M. Munita, C.A. Arias, Mechanisms of antibiotic resistance, Microbiol. Spectr. 4 (2016), https://doi.org/10.1128/microbiolspec.VMBF-0016-2015.
[41] Toxicity profiles, formal toxicity summary for MOLYBDENUM. https://rais.ornl.gov/tox/profiles/molybdenum_f_V1.html.
[42] M. Riaz, R. Zia, F. Saleemi, T. Hussain, *In vitro* antibacterial activity of that Ta_2O_5 doped glass-ceramic against pathogenic bacteria, J. Alloy. Comp. 764 (2018) 10–16, https://doi.org/10.1016/j.jallcom.2018.06.053.
[43] D.A. Pelletier, A.K. Suresh, G.A. Holton, et al., Effects of engineered cerium oxide nanoparticles on bacterial growth and viability, Appl. Environ. Microbiol. 76 (2010) 7981–7989, https://doi.org/10.1128/AEM.00650-10.
[44] A. Thill, O. Zeyons, O. Spalla, et al., Cytotoxicity of CeO_2 nanoparticles for Escherichia coli. physico-chemical insight of the cytotoxicity mechanism, Environ. Sci. Technol. 40 (2006) 6151–6156, https://doi.org/10.1021/es060999b.

Artykuł nr 4:

P, Sochacka, M,U, Jurczyk, K, Kowalski, P,K, Wildstein, M, Jurczyk,

Ultrafine-Grained Ti-31Mo-Type Composites with HA and Ag, Ta2O5 or CeO2 Addition for Implant Applications

Materials 14 (2021) 644
doi,org/10,3390/ma14030644

materials

MDPI

Article

Ultrafine-Grained Ti-31Mo-Type Composites with HA and Ag, Ta_2O_5 or CeO_2 Addition for Implant Applications

Patrycja Sochacka [1,*], Mieczyslawa U. Jurczyk [2], Kamil Kowalski [1], Przemyslaw K. Wirstlein [3] and Mieczyslaw Jurczyk [1]

[1] Institute of Materials Science and Engineering, Poznan University of Technology, Jana Pawła II 24, 61-138 Poznan, Poland; kamil.kowalski@put.poznan.pl (K.K.); mieczyslaw.jurczyk@put.poznan.pl (M.J.)
[2] Division of Mother's and Child's Health, Poznan University of Medical Sciences, Polna 33, 60-535 Poznan, Poland; mjur@poczta.onet.pl
[3] Department of Gynaecology and Obstetrics, Division of Reproduction, Poznan University of Medical Sciences, Polna 33, 60-535 Poznan, Poland; abys@wp.pl
* Correspondence: patrycja.sochacka@doctorate.put.poznan.pl; Tel.: +48-61-665-3508

Abstract: Ultrafine-grained Ti31Mo alloy and Ti31Mo5HA, Ti31Mo5HA-Ag (or Ta_2O_5, CeO_2) composites with a grain size of approximately 2 μm were produced by the application of mechanical alloying and powder metallurgy. Additionally, the surface of the Ti31Mo alloy was modified. In the first stage, the specimens were immersed in 5M NaOH for 24 h at 60 °C. In the second stage, hydroxyapatite (HA) was deposited on the sample surface. The cathodic deposition at −5 V vs. open circuit potential (OCP) in the electrolyte containing 0.25M $CaNa_2$-EDTA (di-calcium ethylenediaminetetraacetic acid), 0.25M K_2HPO_4 in 1M NaOH at 120 °C for 2 h was applied. The bulk Ti31Mo alloy is a single β-type phase. In the alkali-modified surface titanium oxide, Ti_3O is formed. After hydrothermal treatment, the surface layer mostly consists of the $Ca_{10}(PO_4)_6(OH)_2$ (81.23%) with about 19% content of $CaHPO_4 \cdot 2H_2O$. Using optical profiler, roughness 2D surface topography parameters were estimated. The in vitro cytocompatibility of synthesized materials was studied. The cell lines of normal human osteoblasts (NHost) and human periodontal ligament fibroblasts (HPdLF) was conducted in the presence of tested biomaterials. Ultrafine-grained Ti-based composites altered with HA and Ag, Ta_2O_5 or CeO_2 have superior biocompatibility than the microcrystalline Ti metal. NHost and HPdLF cells in the contact with the synthesized biomaterial showed stable proliferation activity. Biocompatibility tests carried out indicate that the ultrafine-grained Ti31Mo5HA composites with Ag, Ta_2O_5, or CeO_2 could be a good candidate for implant applications.

Keywords: Ti31Mo alloy; hydroxyapatite; biomaterials; ultrafine grain; metal matrix composites; cell proliferation; MTS assay

check for updates

Citation: Sochacka, P.; Jurczyk, M.U.; Kowalski, K.; Wirstlein, P.K.; Jurczyk, M. Ultrafine-Grained Ti-31Mo-Type Composites with HA and Ag, Ta_2O_5 or CeO_2 Addition for Implant Applications. *Materials* **2021**, *14*, 644. https://doi.org/10.3390/ma14030644

Academic Editor: Giovanni Vozz
Received: 4 January 2021
Accepted: 28 January 2021
Published: 30 January 2021

1. Introduction

Stainless steel, cobalt alloys, titanium, and titanium-base alloys are applied as implant materials. These cannot be substituted by ceramics or polymers because of their high strength and toughness [1]. Stainless steel and Co–Cr–Mo due to high Young modulus in comparison to that of bone tend to fail after long-term use.

In the production of dental and orthopedic implants titanium and its alloys are used [2]. These biomaterials have interesting properties: low density (4.5 g/cm^3), low Young modulus (about 100 GPa), high tensile strength (240 MPa), and due to the passive titanium oxide film (TiO_2) have acceptable corrosion properties [3]. On, the other hand, titanium and titanium alloys, due to low hardness, have poor tribological properties [4]. Additionally, some research reports signifying metal release and corrosion in vivo [5,6].

The aim of the current study is directed at improving the physicochemical and mechanical properties as well as biocompatibility of Ti-based systems through crystal structure evolution (α → β) and new microstructure formation (micro → nano or ultrafine) via its

chemical composition modification and processing method, respectively [4,5,7–19]. β-type titanium alloys are interesting biomaterials for innovative implantable medical devices. Recently studies on TiMo, TiNb, TiZrNb, TiNbHf, TiNbZrTa, TiNbZrTaSiFe have confirmed their interesting properties for future application in medicine [9,13–17,19–25]. It is important to note, that the cytotoxicity of Mo, Zr, and Nb is lower than that for commercial purity Ti [26].

The latest studies have proven that Ti–Mo alloys open new possibilities for advanced medical implants [13,16,17]. The solubility limits of molybdenum in titanium is 8 wt. % [27]. The phase evolutions and properties of Ti–Mo ($10 \leq x \leq 35$) alloys were studied [16]. Additionally, the influence of the preparation method on transitions ($\alpha \rightarrow \beta$) as well as on the microstructure, mechanical, corrosion, and surface wettability properties was investigated, as well [17]. It is possible to obtain Ti–Mo alloys with high β-phase content and also low porosity by using hot pressing (HP) at low temperature (800 °C/5 min) compared to cold pressing and sintering (800 °C/0.5 h).

One possibility to enhance the mechanical, corrosion, and biological properties of implant materials, except the chemical composition modification, is the microstructure control via severe plastic deformation (SPD) [28,29] or mechanical alloying (MA) processing methods [11,12,15–19]. Published results proved that the nano- or ultrafine grain microstructure of titanium and its alloys improved the mechanical properties as well as the biocompatibility [18,19,29–32].

To change the biological properties of titanium alloys, composites can be synthesized that combine good mechanical properties of titanium and the excellent biocompatibility and bioactivity of ceramics (hydroxyapatite (HA), 45S5 Bioglass) [33]. Bioceramic–titanium composites will have practical applications in medicine and can replace titanium alloys with a ceramic coating. It is well known that ceramic coating improves the surface bioactivity, however, it often falls off due to the poor ceramic/metal interface bonding [11,19,34].

Biomaterials with nano- or ultrafine- grains offer an interesting property for new products in medical applications [4,10,15–19,28–32,35]. Our previous studies confirmed that Ti or Ni-free 316L stainless steel—hydroxyapatite composites exhibit superior properties due to the nanostructure. [10,36]. The mechanical properties and corrosion resistance on bulk Ti-*x* wt. % 45S5 Bioglass nanocomposites (x = 0, 3, 10, and 20) were investigated [10]. For example, the bulk Ti-10 wt. % 45S5 Bioglass composite in comparison to pure titanium is more corrosion resistant and twice as harder. Ti-10 wt. % 45S5 Bioglass scaffold shows an enhanced property for dental implant applications. These composites show better cytocompatibility in comparison with microcrystalline commercial purity titanium.

Another example of materials for potential applications in dentistry and medicine are independently synthesized bulk metal matrix nanocomposites (MMNC) based on titanium and boron [12]. Novel in situ bionanomaterials MMNC based on Ti-B obtained in the processes of mechanical synthesis and powder metallurgy show new properties compared to the microcrystalline counterpart. The combination of their unique structure with good mechanical properties, as well as cell viability and cytological compatibility depending on the processing conditions favor the nanoscale range of results of the Ti-TiB. [12].

Recently, ultrafine-grained Ti-Zr-Nb type composites with 45S5 Bioglass and Ag, Cu, or Zn metals have synthesized, as well [19]. Higher biocompatibility than the reference material (microcrystalline Ti) was observed. Ti23Zr25Nb-9BG composite has interesting mechanical properties. An elastic modulus equals 45 GPa, which is lower than the E modulus for Ti23Zr25 samples with 70% porosity (55 GPa).

In this paper in vitro cytocompatibility of Ti-31 Mo alloy and Ti31Mo5HA, Ti31Mo5HA-Ag (or Ta_2O_5, CeO_2) biocomposites were investigated and compared with commercial purity (CP) Ti. Additionally, the surface of the basic Ti31Mo alloy was modified. The biomaterials were tested on the cell lines of normal human osteoblasts (NHost) and human periodontal ligament fibroblasts (HPdLF). The studies aimed to confirm superior biocompatibility of ultrafine-grained Ti-based composites altered with HA and Ag, Ta_2O_5, or CeO_2.

2. Materials and Methods

2.1. Sample Preparation

Details on sample synthesis are available in our recent papers [16,18]. The ultrafine-grained Ti31Mo-type samples (diameter—6 mm; height—3 mm) were synthesized by MA and powder metallurgy. High-purity powder precursors from Alfa-Aesar, Heysham, Lancashire; United Kingdom (Ti), Sigma-Aldrich, St. Louis, MO, USA), (Mo, HA, Ag, Ta_2O_5, and CeO_2) were used. In the first stage, the powders were ground in SPEX 8000 Mixer Mill (SPEX SamplePrep, Metuchen, NJ, USA) for 39 h at room temperature and the ball to powder ratio (BPR) was 10:1. Then, the green compacts were obtained by uniaxial pressing (600 MPa) and finally were sintered at 800 °C for 0.5 h in an argon atmosphere.

Polishing, then washing with distilled water, rinsing and degreasing ultrasonically in ethanol, and finally, air-drying were carried out to prepare the surface of the samples for surface treatment. To obtain an oxide layer on the surface the samples were immersed in 5M NaOH (Poch S.A., Gliwice, Poland) for 24 h in a vessel heated to 60 °C in a furnace. After the alkali treatment specimens were washed with distilled water and ethanol. Finally, the hydroxyapatite was deposited on the surface. Aqueous electrolyte containing 0.25M $CaNa_2$-EDTA (Sigma-Aldrich, St. Louis, MO, USA), 0.25M K_2HPO_4 (Alfa-Aesar, Heysham, Lancashire; United Kingdom) in 1M NaOH (Poch S.A., Gliwice, Poland) at 120 °C for 2 h was applied.

For this study, the synthesized Ti-31Mo—materials were labeled as follows:

- ultrafine-grained Ti31Mo alloy—Ti31Mo
- ultrafine-grained Ti31Mo alloy after NaOH 60 °C/24 h oxidation—Ti31Mo (Ox)
- ultrafine-grained Ti31Mo alloy after hydrothermal treatment—Ti31Mo (HT)
- ultrafine-grained Ti31Mo-5 wt. % HA composite—Ti31Mo5HA
- ultrafine-grained Ti31Mo-5 wt. % HA-1 wt. % Ag composite—Ti31Mo5HA1Ag
- ultrafine-grained Ti31Mo-5 wt. % HA-2 wt. % CeO_2 composite—Ti31Mo5HA2CeO_2
- ultrafine-grained Ti31Mo-5wt. % HA-2 wt. % Ta_2O_5 composite—Ti31Mo5HA2Ta_2O_5

2.2. Materials Characterization

The crystal structure was studied by the application of Panalytical Empyrean equipment with copper radiation; l = 1.54 Å (Almelo, The Netherlands). Additionally, the Rietveld approach was used on the Maud software (Luca Lutterotti, University of Trento, Trento, Italy) for the crystal data estimation and phase quantitative analysis [11,12,15–19]. The applied estimation involved the simulation of the diffraction patterns based on the structural models for Ti(β) (ref. code 01-074-7075), Ti_3O (ref. code 01-073-1117), $Ca_{10}(PO_4)_6(OH)_2$ (ref. code 04-010-6315), and $CaHPO_4{\cdot}2H_2O$ (ref. code 01-072-1240). The chemical compositions and microstructure of the studied alloy and composites were investigated by the application of a scanning electron microscope (SEM, VEGA 5135, and Mira 3, Tescan, Brno, Czech Republic) with an energy-dispersive spectrometer (EDS, PTG Prison Avalon). T8000 Profiler (Hommel–Etamic, Villingen-Schwenningen, Germany) was applied to analyze the surface morphology of the samples. The EVOVIS software (Hommel-Etamic, Villingen-Schwenningen, Germany) was applied to analyze the obtained profiles. The arithmetic mean roughness (μm)—R_a, the maximum height of the profile μm)—R_t, 10-point mean roughness (μm)—R_z was estimated. The weight loss (W) of the samples, after immersion in them for 7 days in the Ringer solution environment, was measured to evaluate the corrosion resistance of synthesized biomaterials. Digital camera Kruss-DSA25 (KRÜSS GmbH, Hamburg, Germany) and Kruss-Advanced 1.5 software (KRÜSS GmbH, Hamburg, Germany) and ellipse fitting method were used to determine the contact angles for diiodomethane and glycerol at 23 °C [37]. The application of Owens, Wendt, Rabel, and Kaelble method allowed to establish the surface free energy (SFE) [38,39].

2.3. In Vitro Evaluation

The in vitro cytocompatibility investigations were done under standard conditions in 96 well culture dishes in the Heraeus BB16 incubator (Heraeus Instruments GmbH Bereich

Termotech, Hanau, Germany) at 37 °C temperature, in an atmosphere of 5% CO_2, and humidity level of 95%. The discs of Ti31Mo—type materials, as well as microcrystalline titanium, were sterilized by immersion in 70% of the EtOH dilution and drying in a laminar flow hood with the ultraviolet (UV) sterilization of each side of the insert for 12 h.

Normal human osteoblasts (NHost., CC-2538) and human periodontal ligament fibroblasts (HPdLF, CC-7049) were ordered together with a dedicated set of breeding media, respectively: CC-3207 OGM Osteoblast Growth BulletKit (CC-3208+CC-4193) and CC-3205 SCGM Stromal Bullet CellKit (CC-3204+CC-4181) at LONZA Group Ltd. (Morristown, NJ, USA). More details related to cell line preparation with the conditioning of breeding media are available in our recently published paper [19].

To assess the number of cell proliferation, viability, and cytotoxicity the CellTiter 96® AQueous Non-Radioactive Cell Proliferation Assay (MTS) (Promega, Madison, WI, USA) was applied [12,19,32,35]. The MTS assay protocol is based on the reduction of the MTS tetrazolium compound by viable cells to generate a colored, soluble formazan product the quantity of which was measured spectrophotometrically (λ = 490 nm) in the ELISA plate reader, (MRX Dynex, Chantilly, VA, USA). Microcrystalline titanium (Ti) was applied as reference material of the cell growth in the conditioned media of the composite Ti31Mo-type samples. The cells were grown in triplicates for 24, 72, and 120 h in each cell type and test materials. The MTS test results were averaged for each type of cells and conditioned medium. The relative viability of the cells (RVC) was calculated based on the value of absorbance [19].

Photographic documentation of the cell cultures was conducted in conditioned media in 24 well dishes, on sterile 13 mm cover slides. The photographic documentation was made in the magnification of 150 × by the application of a Nikon digital camera (Nikon, Minato-ku, Tokyo, Japan).

3. Results

3.1. Crystal Structure, Phase Contents, the Morphology

The uniaxial pressing of Ti31Mo type materials leads to the formation of green compacts. These were sintered at 800 °C for 0.5 h. The Ti31Mo alloy showed Ti(β)-type phase (a = 3.2433 Å). In the Ti31Mo5HA composite, mainly β-type phases (61.1%), as well as the α-Ti (24.3%) and Ti_3P (14.6%), were observed. The presence of the Ti_3P phase confirms the decomposition of HA during the MA process. More details related to the HA content on the crystal structure of Ti-31Mo alloy can be found in our previous paper [18].

In bulk Ti31Mo5HA composite with 1 wt. % Ag, 2 wt. % Ta_2O_5 and 2 wt.% CeO_2 the multiphase material were observed: regular phases $Ti_{0.67}Mo_{0.33}$, $Ti_{0.75}Mo_{0.25}$, β-Ti in total amounts 65.4, 54.6, and 74.5, respectively, and hexagonal α-Ti forms as also Ti_3P, Ti_4P_3 related to HA addition. The SEM micrograph of the bulk ultrafine-grained Ti31Mo alloy is shown in Figure 1. The average grains of about 2 μm can be seen for this sample. The average grain size is about 150–170 μm in microcrystalline Ti.

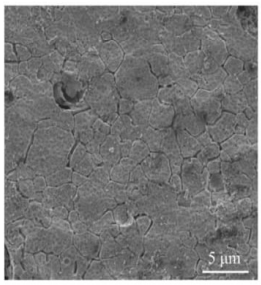

Figure 1. Scanning electron microscopy (SEM) micrograph of the bulk ultrafine-grained Ti31Mo alloy.

Figure 2 shows X-ray diffraction (XRD) results of ultrafine-grained Ti31Mo alloy before (a), after NaOH 60 °C/24 h (b), and hydrothermal treatments (c). The bulk Ti31Mo alloy is a single β-type phase. In the alkali modified (5M NaOH for 24 h at 60 °C) surface titanium oxide, Ti_3O, is formed. Its content equals 4.93%. After hydrothermal treatment, the surface layer mostly consists of the $Ca_{10}(PO_4)_6(OH)_2$ (81.23%) with about 19% content of $CaHPO_4 \cdot 2H_2O$ (Table 1). Due to their bioactive properties, these ceramics are useful in bone surgery. Additionally, they are non-toxic and non-allergic.

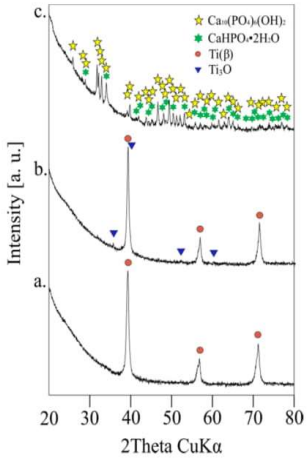

Figure 2. Ti31Mo alloy before modification (**a**), after NaOH 60 °C/24 h (**b**), and hydrothermal treatment (**c**).

Table 1. The structural parameters of Ti31Mo alloys before modification, after NaOH 60 °C/24 h, and hydrothermal treatment.

Structure Parameters			Ti31Mo	sTi31Mo (Ox)	Ti31Mo (HT)
sig		-	1.4629564	1.5791782	1.405559
R_{wp}		[%]	6.0970262	6.329574	5.535124
R_{exp}		[%]	4.167606	4.0081444	3.9381716
Ti(β)	A	[%]	**100.00**	**95.07**	-
	a	[Å]	3.2433(1)	3.2426(1)	-
	V	[$Å^3$]	34.1(0)	33.5(0)	-
Ti_3O	A	[%]	-	**4.93**	-
	a	[Å]	-	5.1361(41)	-
	c	[Å]	-	9.5623(164)	-
	V	[$Å^3$]	-	36.6(0)	-
$Ca_{10}(PO_4)_6(OH)_2$	A	[%]	-	-	**81.23**
	a	[Å]	-	-	9.4252(6)
	c	[Å]	-	-	6.8894(6)
	V	[$Å^3$]	-	-	530.1(1)
$CaHPO_4 \cdot 2H_2O$	A	[%]	-	-	**18.77**
	a	[Å]	-	-	6.3748(32)
	b	[Å]	-	-	15.2564(58)
	c	[Å]	-	-	5.7910(31)
	V	[$Å^3$]	-	-	487.8(7)

In the alkali and hydrothermally treated Ti31Mo alloy, the hydroxyapatite was deposited. Porous Ca-P protrusions in cauliflower-like shape are visible (Figure 3). The morphology, size, and structural organization of HA particles could be controlled by changing the temperature and time during the HT process. The osteoblast cells will be grown

on that porous Ca-P layer. Figure 4 shows a cross-section view of the surface layer with a thickness close to 155 µm.

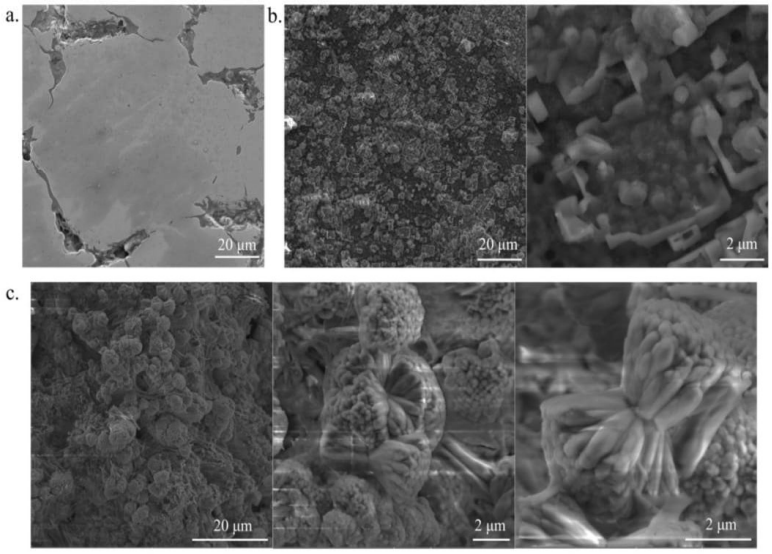

Figure 3. SEM micrographs for Ti31Mo before modification (**a**), after NaOH 60 °C/24 h (**b**), and hydrothermal treatment (**c**).

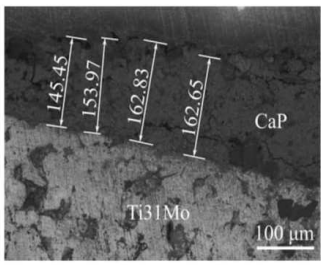

Figure 4. Cross-section view of CaP surface layer for Ti31Mo after hydrothermal treatment.

The EDS analysis confirmed the XRD analysis and proved the content of both Ca and P on the surface after HT treatment (Table 2, Figure 5). After immersion in 5M NaOH at 60 °C for 24 h, the average sodium content was equal to 2.22 wt. % due to the presence of the sodium titanate [40] which can positively influence the nucleation and growth of the surface layer. EDS analysis of the deposited Ca-P layer (Figures 3 and 4) confirmed the formation of hydroxyapatite (HA), which was similar to the human hard tissues in morphology and composition. An important property of HA is its stability in the body fluids in comparison to other calcium phosphates.

Table 2. Energy-dispersive spectrometer (EDS) results for Ti31Mo after NaOH 60 °C/24 h and hydrothermal treatment.

Element	Line	Ti31Mo(Ox)	Ti31Mo(HT)
		wt. %	wt. %
Ti	$K\alpha_1$	50.07	0.00
Mo	$L\alpha_1$	41.63	0.00
Ca	$K\alpha_1$	0.00	45.07
P	$K\alpha_1$	0.00	24.28
O	$K\alpha_1$	6.07	16.56
Na	$K\alpha_1$	2.22	6.81
K	$K\alpha_1$	0.00	7.28
Total	-	**100.00**	**100.00**

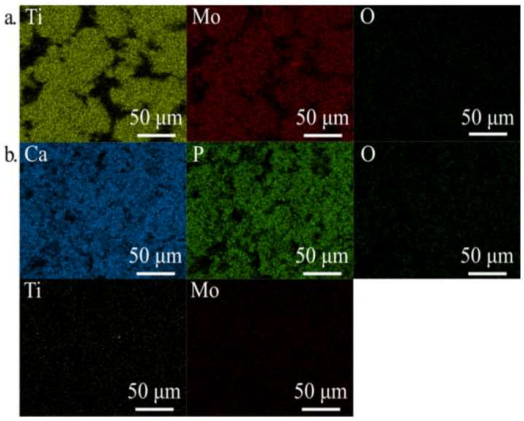

Figure 5. EDS mapping for Ti31Mo after NaOH 60 °C/24 h (**a**) and hydrothermal treatment (**b**).

3.2. Surface Properties

Figure 6 shows X-profiles, at the different processing stages, of the bulk Ti31Mo alloy. Surface roughness is a leading property of the implant during the osseointegration. The proliferation of cells can be supported also by nano-topography [29,31,41]. The bulk ultrafine-grained Ti31Mo alloy had Ra, Rt, and Rz values of approximately 1.04, 14.55, and 10.59 µm, respectively (Table 3). After NaOH 60 °C/24 h (b) and hydrothermal treatments this alloy surface had an average Ra, Rt, and Rz values in the range of 2–9, 22–62, and 16–45 µm, respectively. Large pores formed on the surface of the sample during the two steep of treatment aid proliferation. The highly developed surface morphology obtained after additional Ca-P deposition facilitates the colonization by pathogenic microorganisms [42–46].

Table 3. Two-dimensional (R_a, R_t, R_z) parameters for the Ti31Mo alloy before modification, after NaOH 60 °C/24 h, and hydrothermal treatment; parameters are taken from the surface area of 1.08 mm^2.

2D Parameters	Ti31Mo	Ti31Mo (Ox)	Ti31Mo (HT)
$\mathbf{R_a}$	1.04 ± 0.13	2.40 ± 0.36	9.22 ± 1.93
$\mathbf{R_t}$	14.55 ± 0.78	22.18 ± 1.85	62.52 ± 10.85
$\mathbf{R_z}$	10.59 ± 0.77	15.70 ± 1.69	45.39 ± 5.95

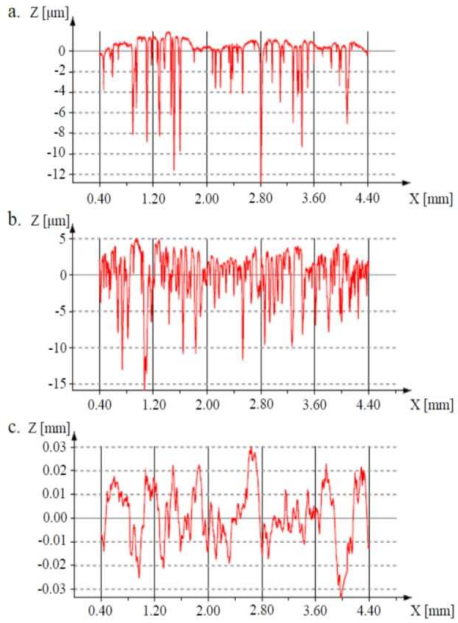

Figure 6. The surface roughness of the Ti31Mo before modification (**a**), after NaOH 60 °C/24 h (**b**), and hydrothermal treatment (**c**).

3.3. Corrosion and Surface Wetting Properties

Plasma-spraying, grit blasting, acid etching, anodization, or calcium phosphate coatings are methods used to reduce the corrosion rate of titanium alloys in simulated body fluids [8,11,47–50]. In this study, the corrosion resistance was evaluated by the weight loss (W) of the samples after immersion in the Ringer solution environment. In the case of Ti31Mo alloy after HT treatment W equals 0.0150 mg/day (Table 4). The alkali treatment led only to a decrease in weight loss, which was caused by the $Na_2Ti_2O_4(OH)_2$ and Ti_3O formation. The same positive effect was observed previously in the case of mechanically alloyed and sintered titanium-hydroxyapatite nanocomposites and other Ti-based metallic biomaterials [51–53]. Better corrosion resistance is possible with Ti-Bioglass(45S5)-Ag composites due to the rutile layer on the surface [10].

Table 4. Estimated weight loss (W) after 7-days immersing in Ringer solution environment and contact angle (CA), surface free energy, disperse, and polar for Ti31Mo before modification, after NaOH 60 °C/24 h and hydrothermal treatment.

Parameter	Unit	Ti31Mo	Ti31Mo (Ox)	Ti31Mo (HT)
W	**(mg/day)**	0.0496(16)	0.0357(22)	0.0150(25)
Diiodomethane CA	**(°)**	58.76 ± 4.54	46.16 ± 5.71	impossible to measure
Glycerol CA	**(°)**	50.12 ± 1.39	55.97 ± 5.31	31.28 ± 2.78
Surface free energy	**(mN/m)**	43.16 ± 0.37	42.54 ± 3.07	-
Disperse	**(mN/m)**	29.29 ± 2.61	36.37 ± 3.10	-
Polar	**(mN/m)**	13.87 ± 2.87	6.17 ± 1.41	-

The surface contact angles and free energy in diiodomethane and glycerol were significantly improved for an electrochemically etched and deposited sample (Table 4). Surface free energy was measured to be about 43 mN/m after NaOH 60 °C/24 h treatment. On the other hand, contact angles were decreased to about 31°, after hydrothermal treatment,

in the case of glycerol. As a result, the materials after surface treatment were more hydrophilic, which promotes the growth of bone tissue. This surface had a positive effect on the absorption, adhesion, and cell proliferation activity [54].

3.4. Biocompatibility Studies

An in vitro test is a method to test for the toxicity of a biomaterial [54,55]. In our study, we tested Normal Human Osteoblasts and Human Periodontal Ligament Fibroblasts. The MTS [3-(4,5-dimethylthiazol-2-yl)-5-(3-carboxymethoxyphenyl)-2-(4-sulfophenyl)-2H -tetrazolum] assay was used to assess cell proliferation in a conditioned medium. The tetrazolium salts were reduced by viable cells to formazan products that are directly soluble in the cell culture medium. The quantity of formazan product was measured. Microcrystalline titanium (Ti) was applied as reference material for the cell growth of the composite Ti31Mo-type samples.

The sample chemical composition and its microstructures as well as the time of culture of NHost and HPdLF influences strongly the final growth patterns. As we can see in Figures 7 and 8, the growth rate was differentiated between the NHost and HPdLF cultures. Generally, NHost cells overgrow more regularly and faster on the tested Ti31Mo-type biomaterials.

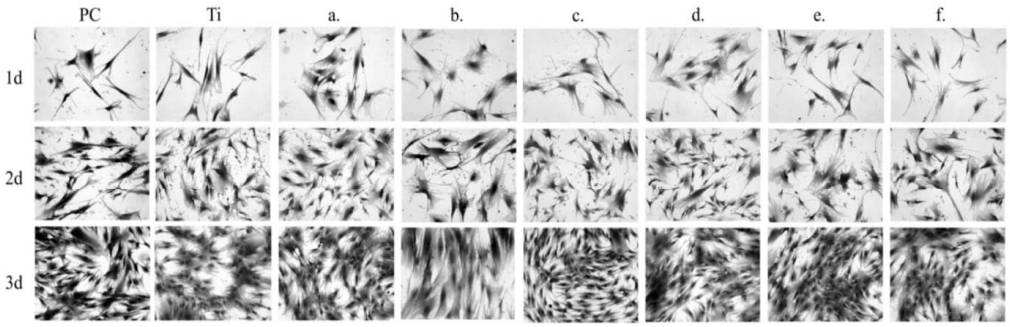

Figure 7. Morphology of the normal human osteoblast (NHost) cells cultured for a different time: 24 h, 3 days, and 5 days: Ti31Mo (**a**), Ti31Mo after hydrothermal treatment (HT) (**b**), Ti31Mo5HA (**c**), Ti31Mo5HA1Ag (**d**), Ti31Mo5HA2CeO_2 (**e**), Ti31Mo5HA2Ta_2O_5 (**f**).

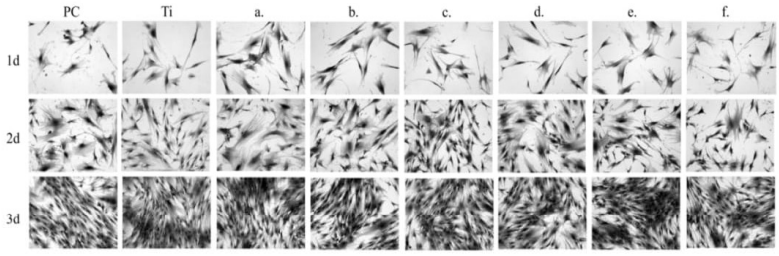

Figure 8. Morphology of the fibroblasts cells cultured for a different time: 24 h, 3 days, and 5 days: Ti31Mo (**a**), Ti31Mo after hydrothermal treatment (HT) (**b**), Ti31Mo5HA (**c**), Ti31Mo5HA1Ag (**d**), Ti31Mo5HA2CeO_2 (**e**), Ti31Mo5HA2Ta_2O_5 (**f**).

Results of metabolic activity of NHost. and HPdLF and RVC values (%) for the reference sample (Ti) measured based on the MTS test after 24 h, 72 h, and 120 h of breeding in conditioned media are shown in Figures 9 and 10; PC (positive control) is the cells of a given type bred in a fresh, unconditioned medium. Interesting results were noted for the Ti31Mo after hydrothermal treatment and for bulk Ti31Mo5HA1Ag, Ti31Mo5HA2CeO_2, Ti31Mo5HA2Ta_2O_5 samples.

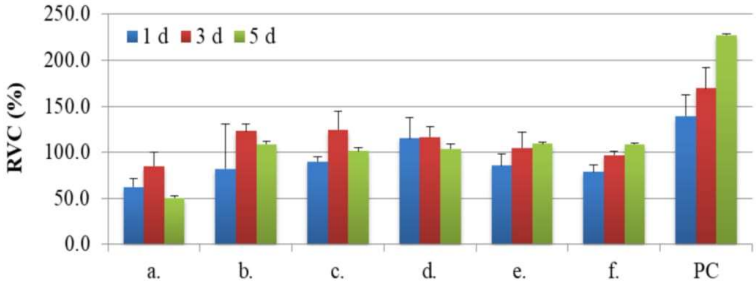

Figure 9. The results of the MTS assays performed at 1, 3, and 5 days on the viability of the osteoblasts for: Ti31Mo (**a**), Ti31Mo after hydrothermal treatment (**b**), Ti31Mo5HA (**c**), Ti31Mo5HA1Ag (**d**), Ti31Mo5HA2CeO_2 (**e**), Ti31Mo5HA2Ta_2O_5 (**f**); PC—positive control.

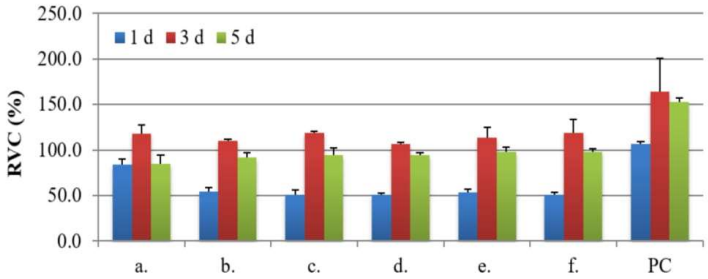

Figure 10. The results of the MTS assays performed at 1, 3, and 5 days on the viability of the fibroblasts for: Ti31Mo (**a**), Ti31Mo after hydrothermal treatment (**b**), Ti31Mo5HA (**c**), Ti31Mo5HA1Ag (**d**), Ti31Mo5HA2CeO_2 (**e**), Ti31Mo5HA2Ta_2O_5 (**f**); PC—positive control.

4. Discussion

β-type Ti alloys are interesting metallic materials for medical applications. Ultrafine-grained Ti-31 Mo alloy and Ti31Mo5HA, Ti31Mo5HA-Ag (or Ta_2O_5, CeO_2) composites were synthesized and their properties investigated. The heat treatment of the amorphous material after the MA process led to the creation of β-type Ti31Mo alloy with a unique microstructure with a grain size of 2 μm. The increase of the HA concentration in the Ti31Mo composite increased the content of the α-phase. The alkali and hydrothermal treatment in the electrolyte containing 0.25M $CaNa_2$-EDTA, 0.25M K_2HPO_4 in 1M NaOH at 120 °C for 2 h were applied. On a porous surface, the bioactive ceramic CaP layer was deposited.

In the corrosive environment of the tissue and body fluids, implants unexpected local corrosion. The corrosion products in the tissue can create a toxic effect [3]. The tests in the Ringer solution showed a positive effect on corrosion resistance of the CaP layer formed on ultrafine-grained Ti31Mo composite. This composite showed the best corrosion resistance after oxidation and CaP deposition (estimated weight loss of W = 0.015 mg/day). Contact angles of ultrafine-grained Ti31Mo alloy were determined in glycerol and show a visible decrease for bulk Ti31Mo alloy after oxidation and hydrothermal treatment (CA = 31°).

In vitro cytocompatibility of Ti-31 Mo alloy and Ti31Mo5HA, Ti31Mo5HA-Ag (or Ta_2O_5, CeO_2) biocomposites was investigated and compared with commercial purity (CP) Ti. The cell lines of normal human osteoblasts (NHost) and human periodontal ligament fibroblasts (HPdLF) was conducted in the presence of tested biomaterials. NHost and HPdLF cells showed very good cell proliferation, colonization, and multilayering. The surface topography and the chemical composition of the biomaterial are key factors for the successful implant integration with the hard tissue. So, the biofunctionalization

of synthesized composites represents an important procedure in the development of biomaterials that support the initial healing of the implant.

Silver has good antibacterial properties [54,56]. Earlier, the properties of Ti samples modified with nanodendrites of Ag were studied in detail [32]. These biomaterials have good biocompatibility. Recently, the antibacterial properties of Ti31Mo5HA composite containing Ag, Ta_2O_5, and CeO_2 against *Staphylococcus aureus* was evaluated [18]. The Ti31Mo5HA1Ag and Ti31Mo5HA2CeO_2 biomaterials have lower adhesion levels of *S. aureus* ($p < 0.05$). Additionally, these composites possess good mechanical properties [18]. Young's modulus around 95 GPa is measured for bulk Ti31Mo5HA composites with 1 wt. % Ag and 2 wt. % CeO_2 additions.

Good biocompatibility makes these biomaterials attractive in applications in implant applications. Performed in vitro studies confirm that ultrafine-grained bulk Ti31Mo-type composites altered with HA and Ag, Ta_2O_5, or CeO_2 did not show cytotoxic properties against cultured NHost and HPdLF cells. Independently, electrochemical anodic and cathodic surface treatment was applied to the Ti-6Zr-4Nb bulk alloy with nanostructure [57]. This treatment supports osteoblast adhesion and cell proliferation due to the created pores.

Recently, the properties of Ti-based scaffolds with a porosity of 70% and pore sizes in the range of 200–300 μm were synthesized by the application of titanium and ammonium hydrogen carbonate particles [58]. Anodization and heat treatment allows the formation of bioactive anatase nanotubes with the size of approximately 100 nm. Due to apatite creation, this surface modification on the Ti scaffold improved the biocompatibility. Finally, the compressive strength of 36.8 MPa was equal to the cancellous bone.

Until now, large numbers of new Ti-based alloys have been synthesized and their properties studied in vivo [12–14,20–26,44–46,49,50]. The environmental impacts and toxicity of ultrafine Ti-bioceramic composites should be evaluated. New implant biomaterials with β-crystal structure and ultrafine-grained microstructure should demonstrate a reduced susceptibility to bacterial colonization and should not have pathogenic effects. The ultrafine-grained Ti31Mo-type composites with the HA and Ag, Ta_2O_5, or CeO_2 addition may support the continuous adaptation process to the implant by the host organism.

5. Conclusions

In our study, bulk ultrafine-grained Ti31Mo-type composites with HA and Ag, CeO_2, or Ta_2O_5 additions were synthesized. The results of surface modifications of the ultrafine-grained Ti31Mo alloy were shown. This Ti31Mo alloy is favorable for biomedical applications. The modification of the alloy surface improves their properties. The alkali treatment (immersion in 5M NaOH (60 °C/24 h) and hydrothermal treatment in the electrolyte containing 0.25M $CaNa_2$-EDTA, 0.25M K_2HPO_4 in 1M NaOH at 120 °C for 2 h, achieves promising results of surface fitting for implant applications. Ca-P layer formation during cathodic deposition is useful in osseointegration. The in vitro biocompatibility studies show that the bulk composites based on Ti31Mo5HA and Ag, CeO_2, or Ta_2O_5 are good candidates for future implant applications.

Author Contributions: Conceptualization, M.J.; Formal analysis, P.S., M.U.J., K.K. and M.J.; Funding acquisition, M.J.; Investigation, P.S.; M.U.J.; K.K., P.K.W. and M.J.; Supervision, M.J.; Writing—original draft, P.S. and M.J.; Writing—review and editing, P.S., M.U.J., K.K., P.K.W. and M.J. All authors have read and agreed to the published version of the manuscript.

Funding: The work has been financed by the National Science Centre Poland under decision no.: DEC-2017/25/B/ST8/02494.

Informed Consent Statement: Not applicable.

Conflicts of Interest: Authors declare no conflict of interest.

References

1. Zaman, H.K.; Sharif, S.; Idris, M.H.; Kamarudin, A. Metallic Biomaterials for Medical Implant Applications: A Review. *Appl. Mech. Mater.* **2015**, *735*, 19–28. [CrossRef]

2. Rack, H.J.; Qazi, J.I. Titanium alloys for biomedical applications. *Mater. Sci. Eng. C* **2006**, *26*, 1269–1277. [CrossRef]
3. Bodunrin, M.O.; Chown, L.H.; van der Merwe, J.W.; Alaneme, K.K.; Oganbule, C.; Klenam, D.E.F.; Mphasha, N.P. Corrosion behavior of titanium alloys in acidic and saline media: Role of alloy design, passivation integrity, and electrolyte modification. *Corros. Rev.* **2020**, *38*, 25–47. [CrossRef]
4. Elias, C.N.; Lima, J.H.C.; Valiev, R.; Meyers, M.A. Biomedical applications of titanium and its alloys. *JOM* **2008**, *60*, 46–49. [CrossRef]
5. Dragan-Raileanu, L.A.; Cotrutz, C.E.; Munteanu, C.; Strugaru, S.; Avram, P.; Istrate, B.; Petreus, T. In vitro study regarding the cytotoxicity of some TiNbZr alloys. *Ann. Rom. Soc. Cell Biol.* **2013**, *18*, 186–191.
6. Sidambe, A.T. Biocompatibility of advanced manufactured titanium implants-A review. *Materials* **2014**, *7*, 8168–8188. [CrossRef]
7. Cojocaru, V.D.; Nocivin, A.; Trisca-Rusu, C.; Dan, A.; Irimescu, R.; Raducanu, D.; Galbinasu, B.M. Improving the Mechanical Properties of a β-type Ti-Nb-Zr-Fe-O Alloy. *Metals* **2020**, *10*, 1491. [CrossRef]
8. Godarzi, R.; Rasmusson, L.; Dasmah, A.; Albrektsson, T. Effects of implant design and surface on osseointegration. An experimental study in the dog mandible. *Appl. Osseointegr. Res.* **2008**, *7*, 58–60.
9. Eisenbarth, E.; Velten, D.; Müller, M.; Thull, R.; Breme, J. Biocompatibility of β-stabilizing elements of titanium alloys. *Biomaterials* **2004**, *25*, 5705–5713. [CrossRef]
10. Jurczyk, K.; Niespodziana, K.; Jurczyk, M.U.; Jurczyk, M. Synthesis and characterization of titanium-45S5 bioglass nanocomposites. *Mater. Des.* **2011**, *32*, 2554–2560. [CrossRef]
11. Miklaszewski, A.; Jurczyk, M.U.; Jurczyk, M. Microstructural development of Ti-β alloyed layer for hard tissue applications. *J. Mater. Sci. Technol.* **2013**, *29*, 565–572. [CrossRef]
12. Miklaszewski, A.; Jurczyk, M.; Kaczmarek, M.; Paszel-Jaworska, A.; Romaniuk, A.; Lipińska, N.; Żurawski, J.; Urbaniak, P.; Jurczyk, M. Nanoscale size effect in in situ titanium based composites with cell viability and cytocompatibility studies. *Mater. Sci. Eng. C* **2017**, *73*, 525–536. [CrossRef] [PubMed]
13. Meng, Q.; Zhang, J.; Huo, Y.; Sui, Y.; Zhang, J.; Guo, S.; Zhao, X. Design of low modulus β-type titanium alloys by tuning shear modulus C44. *J. Alloys Compd.* **2018**, *745*, 579–585. [CrossRef]
14. Frutos, E.; Karlík, M.; Jiménez, J.A.; Langhansová, H.; Lieskovská, J.; Polcar, T. Development of new β/α″-Ti-Nb-Zr biocompatible coating with low Young's modulus and high toughness for medical applications. *Mater. Des.* **2018**, *142*, 44–55. [CrossRef]
15. Marczewski, M.; Miklaszewski, A.; Jurczyk, M. Structure evolution analysis in ultrafine-grained Zr and Nb-based beta titanium alloys. *J. Alloys Compd.* **2018**, *765*, 459–469. [CrossRef]
16. Sochacka, P.; Miklaszewski, A.; Jurczyk, M. Development of β-type Ti-x at. % Mo alloys by mechanical alloying and powder metallurgy: Phase evolution and mechanical properties ($10 \leq x \leq 35$). *J. Alloys Compd.* **2019**, *776*, 370–378. [CrossRef]
17. Sochacka, P.; Miklaszewski, A.; Kowalski, K.; Jurczyk, M. Influence of the processing method on the properties of Ti23 at.% Mo alloy. *Metals* **2019**, *9*, 931–947. [CrossRef]
18. Sochacka, P.; Miklaszewski, A.; Jurczyk, M.; Pecyna, P.; Ratajczak, M.; Gajecka, M.; Jurczyk, M.U. Effect of hydroxyapatite and Ag, Ta_2O_5 or CeO_2 addition on the properties of ultrafine-grained Ti31Mo alloy. *J. Alloys Compd.* **2020**, *823*, 153749. [CrossRef]
19. Marczewski, M.; Jurczyk, M.U.; Kowalski, K.; Miklaszewski, A.; Wirstlein, P.K.; Jurczyk, M. Composite and surface functionalization of ultrafine-grained Ti23Zr25Nb alloy for medical applications. *Materials* **2020**, *13*, 5252. [CrossRef]
20. Guillemot, F.; Prima, F.; Bareille, R.; Gordin, D.-M.; Gloriant, T.; Durrieu, M.; Ansel, D.; Baquey, C. Design of new titanium alloys for orthopaedic applications. *Med. Biol. Eng. Comput.* **2004**, *42*, 137–141. [CrossRef]
21. Bai, Y.; Deng, Y.; Zheng, Y.; Li, Y.; Zhang, R.; Lv, Y.; Zhao, Q.; Wei, S. Characterization, corrosion behavior, cellular response and in vivo bone tissue compatibility of titanium–niobium alloy with low Young's modulus. *Mater. Sci. Eng. C* **2016**, *59*, 565–576. [CrossRef] [PubMed]
22. Majumdar, P.; Singh, S.B.; Dhara, S.; Chakraborty, M. Influence of boron addition to Ti–13Zr–13Nb alloy on MG63 osteoblast cell viability and protein adsorption. *Mater. Sci. Eng. C* **2015**, *46*, 62–68. [CrossRef] [PubMed]
23. Wang, B.L.; Li, L.; Zheng, Y.F. In vitro cytotoxicity and hemocompatibility studies of Ti-Nb, Ti-Nb-Zr and Ti-Nb-Hf biomedical shape memory alloys. *Biomed. Mater.* **2010**, *5*, 044102. [CrossRef] [PubMed]
24. Bărbînţă, A.C.; Earar, K.; Crimu, C.I.; DrĂgan, L.A.; Munteanu, C. In Vitro Evaluation of the Cytotoxicity of Some New Titanium Alloys. *Key Eng. Mater.* **2014**, *587*, 303–308. [CrossRef]
25. Kopova, I.; Stráský, J.; Harcuba, P.; Landa, M.; Janeček, M.; Bačákova, L. Newly developed Ti–Nb–Zr–Ta–Si–Fe biomedical beta titanium alloys with increased strength and enhanced biocompatibility. *Mater. Sci. Eng. C* **2016**, *60*, 230–238. [CrossRef]
26. Park, Y.-J.; Song, Y.-H.; An, J.-H.; Song, H.-J.; Anusavice, K.J. Cytocompatibility of pure metals and experimental binary titanium alloys for implant materials. *J. Dent.* **2013**, *41*, 1251–1258. [CrossRef]
27. Murray, J.L. The Mo-Ti (Molybdenum-Titanium) System. *Bull. Alloy Phase Diagrams* **1981**, *2*, 185–192. [CrossRef]
28. Valiev, R.Z.; Semenova, I.P.; Jakushina, E.; Latysh, V.V.; Rack, H.; Lowe, R.C.; Petruzelka, J.; Dluhos, L.; Hrusak, D.; Sochova, J. Nanostructured SPD processed titanium for medical implants. *Mater. Sci. Forum* **2008**, *584*, 49–54. [CrossRef]
29. Estrin, Y.; Kasper, C.; Diederichs, S.; Lapovok, R. Accelerated growth of preosteoblastic cells on ultrafine grained titanium. *J. Biomed. Mater. Res. Part A* **2009**, *90*, 1239–1242. [CrossRef]
30. Zhang, L.; Webster, T.J. Nanotechnology and nanomaterials: Promises for improved tissue regeneration. *Nano. Today* **2009**, *4*, 66–80. [CrossRef]

31. Webster, T.J.; Ejiofor, J.U. Increased osteoblast adhesion on nanophase metals: Ti, Ti6Al4V, and CoCrMo. *Biomaterials* **2004**, *25*, 4731–4739. [CrossRef] [PubMed]
32. Kaczmarek, M.; Jurczyk, K.; Koper, J.K.; Paszel-Jaworska, A.; Romaniuk, A.; Lipińska, N.; Żurawski, J.; Urbaniak, P.; Jakubowicz, J.; Jurczyk, M.U. In vitro biocompatibility of anodized titanium with deposited silver nanodendrites. *J. Mater. Sci.* **2016**, *51*, 5259–5270. [CrossRef]
33. Cao, W.P.; Hench, L. Bioactive materials. *Ceramics Int.* **1966**, *22*, 493–507. [CrossRef]
34. Türk, S.; Altınsoy, I.; Efe, G.Ç.; Ipek, M.; Özacar, M.; Bindal, C. Biomimetic synthesis of Ag, Zn or Co doped HA and coating of Ag, Zn or Co doped HA/fMWCNT composite on functionalized Ti. *Mater. Sci. Eng. C* **2019**, *99*, 986–998. [CrossRef] [PubMed]
35. Kaczmarek, M.; Jurczyk, M.U.; Rubis, B.; Banaszak, A.; Kolecka, A.; Paszel, A.; Jurczyk, K.; Murias, M.; Sikora, J.; Jurczyk, M. In vitro biocompatibility of Ti-45S5 bioglass nanocomposites and their scaffolds. *J. Biomed. Mater. Res. Part A* **2014**, *102*, 1316–1324. [CrossRef]
36. Tulinski, M.; Jurczyk, M. Nanostructured nickel-free austenitic stainless steel composites with different content of hydroxyapatite. *Appl. Surf. Sci.* **2012**, *260*, 80–83. [CrossRef]
37. Fitzgibbon, A.; Pilu, M.; Fisher, R.B. Direct least square fitting of ellipses. *IEEE Trans. Pattern. Anal. Mach. Intell.* **1999**, *21*, 476–480. [CrossRef]
38. Kaelble, D.H. Dispersion-polar surface tension properties of organic solids. *J. Adhes.* **1970**, *2*, 66–81. [CrossRef]
39. Owens, D.K.; Wendt, R.C. Estimation of the surface free energy of polymers. *J. Appl. Polym. Sci.* **1969**, *13*, 1741–1747. [CrossRef]
40. Kim, C.; Kendall, M.R.; Miller, M.A.; Long, C.L.; Larson, P.R.; Humphrey, M.B.; Madden, A.S.; Tas, A.C. Comparison of titanium soaked in 5 M NaOH or 5 M KOH solutions. *Mater. Sci. Eng. C* **2013**, *33*, 327–339. [CrossRef]
41. Ward, B.C.; Webster, T.J. Increased functions of osteoblasts on nanophase metals. *Mater. Sci. Eng. C* **2007**, *27*, 575–578. [CrossRef]
42. Webster, T.J.; Schadler, L.S.; Siegel, R.W.; Bizios, R. Mechanisms of enhanced osteoblast adhesion on nanophase alumina involve vitronectin. *Tissue Eng.* **2001**, *7*, 291–301. [CrossRef] [PubMed]
43. Hench, L.L. Bioceramics: From concept to clinic. *J. Am. Ceram. Soc.* **1991**, *74*, 1487–1510. [CrossRef]
44. Burgers, R.; Hahnel, S.; Reichert, T.E.; Rosentritt, M.; Behr, M.; Gerlach, T.; Handel, G.; Gosau, M. Adhesion of Candida albicans to various dental implant surfaces and the influence of salivary pellicle proteins. *Acta Biomater.* **2010**, *6*, 2307–2313. [CrossRef]
45. Wong, S.Y.; Moskowitz, J.S.; Veselinovic, J.; Rosario, R.A.; Timachova, K.; Blaisse, M.R.; Fuller, R.C.; Klibanov, A.M.; Hammond, P.T. Dual functional polyelectrolyte multilayer coatings for implants: Permanent microbicidal base with controlled release of therapeutic agents. *J. Am. Chem. Soc.* **2010**, *132*, 17840–17848. [CrossRef]
46. Guillem-Marti, J.; Delgado, L.; Godoy-Gallardo, M.; Pegueroles, M.; Herrero, M.; Gil, F.J. Fibroblast adhesion and activation onto micro-machined titanium surfaces. *Clin. Oral Implants Res.* **2013**, *24*, 770–780. [CrossRef]
47. Yamazoe, M. Study of corrosion of combinations of titanium/Ti-6Al-4V implants and dental alloys. *Dent. Mater. J.* **2010**, *29*, 542–553. [CrossRef]
48. Adamek, G.; Jurczyk, M.U.; Jakubowicz, J. Biocompatibility of the electrochemically modified surface of the ti-6Zr4Nb alloy. *J. Biomater. Tissue Eng.* **2011**, *1*, 101–109. [CrossRef]
49. Sun, L.; Berndt, C.C.; Gross, K.A.; Kucuk, A. Material fundamentals and clinical performance of plasma-sprayed hydroxyapatite coatings: A review. *J. Biomed. Mater. Res.* **2001**, *58*, 570–592. [CrossRef]
50. Wirsching, K.; Lehle, K.; Jacob, P.; Gleich, O.; Strutz, J.; Kwok, P. Influence of surface processing on the biocompatibility of titanium. *Materials* **2011**, *4*, 1238–1248. [CrossRef]
51. Niespodziana, K.; Jurczyk, K.; Jakubowicz, J.; Jurczyk, M. Fabrication and properties of titanium—hydroxyapatite nanocomposites. *Mater. Chem. Phys.* **2010**, *123*, 160–165. [CrossRef]
52. Upadhyay, D.; Panchal, M.A.; Dubey, R.S.; Srivastava, V.K. Corrosion of alloys used in dentistry: A review. *Mater. Sci. Eng. A* **2006**, *432*, 1–11. [CrossRef]
53. Zhang, B.B.; Zheng, Y.F.; Liu, Y. Effect of Ag on the corrosion behavior of Ti–Ag alloys in artificial saliva solutions. *Dent. Mater.* **2009**, *25*, 672–677. [CrossRef] [PubMed]
54. Yin, I.X.; Zhang, J.; Zhao, I.S.; Mei, M.L.; Li, Q.; Chu, C.H. The Antibacterial Mechanism of Silver Nanoparticles and Its Application in Dentistry. *Int J. Nanomed.* **2020**, *15*, 2555–2562. [CrossRef]
55. Unabia, R.B.; Candidato, R.T.; Pawłowski, L.; Salvatori, R.; Bellucci, D.; Cannillo, V. In vitro studies of solution precursor plasma-sprayed copper-doped hydroxyapatite coatings with increasing copper content. *J. Biomed. Mater. Res. Part B Appl. Biomater.* **2020**, *108*, 2579–2589. [CrossRef]
56. Pelletier, D.A.; Suresh, A.K.; Holton, G.A.; McKeown, C.K.; Wang, W.; Gu, B.; Mortensen, N.P.; Allison, D.P.; Joy, D.C.; Allison, M.R.; et al. Effects of engineered cerium oxide nanoparticles on bacterial growth and viability. *Appl. Environ. Microbiol.* **2010**, *76*, 7981–7989. [CrossRef]
57. Jakubowicz, J.; Adamek, G.; Jurczyk, M.U.; Jurczyk, M. 3D topography study of the biofunctionalizednanocrystalline Ti-6Zr-4Nb/Ca-P. *Mater. Charact.* **2012**, *70*, 55–62. [CrossRef]
58. Fan, X.P.; Feng, B.; Weng, J.; Wang, J.X.; Lu, X. Processing and properties of porous titanium with high porosity coated by bioactive titania nanotubes. *Mater. Lett.* **2011**, *65*, 2899–2901. [CrossRef]

Oświadczenia współautorów o udziale w publikacjach

Poznań, dnia 23 marca 2021 r.

dr hab. inż Andrzej Miklaszewski, prof. PP
Instytut Inżynierii Materiałowej
Politechnika Poznańska
e-mail: andrzej.miklaszewski@put.poznan.pl

Oświadczenie

Niniejszym oświadczam, że w pracy P. Sochacka, **A. Miklaszewski**, M. Jurczyk, Development of β-type Ti-x at. % Mo alloys by mechanical alloying and powder metallurgy: Phase evolution and mechanical properties ($10 \leq x \leq 35$), J Alloys Compd. 776 (2019) 370-378. https://doi.org/10.1016/j.jallcom.2018.10.217. mój udział polegał na wytworzeniu stopów Ti-x at. % Mo ($10 \leq x \leq 35$) metodą prasowania na gorąco, wsparciu merytorycznym podczas analizy wyników i redagowaniu artykułu oraz byciu autorem korespondencyjnym. Jednocześnie wyrażam zgodę na wykorzystanie danych z tej publikacji na potrzeby przewodu doktorskiego Pani mgr inż. Patrycji Sochackiej.

.....
Podpis

Poznań, dnia 23 marca 2021 r.

prof. dr hab. Mieczysław Jurczyk
Instytut Inżynierii Materiałowej
Politechnika Poznańska
e-mail: mieczyslaw.jurczyk@put.poznan.pl

Oświadczenie

Niniejszym oświadczam, że w pracy P. Sochacka, A. Miklaszewski, **M. Jurczyk**, Development of β-type Ti-x at. % Mo alloys by mechanical alloying and powder metallurgy: Phase evolution and mechanical properties ($10 \leq x \leq 35$), J Alloys Compd. 776 (2019) 370-378. https://doi.org/10.1016/j.jallcom.2018.10.217. mój udział polegał na przeprowadzeniu procesów mechanicznej synezy, konsolidacji stopów Ti-x at. % Mo ($10 \leq x \leq 35$), merytorycznej ocenie opracowanych wyników oraz redagowaniu artykułu. Jednocześnie wyrażam zgodę na wykorzystanie danych z tej publikacji na potrzeby przewodu doktorskiego Pani mgr inż. Patrycji Sochackiej.

.....
Podpis

Poznań, dnia 23 marca 2021 r.

dr hab. inż Andrzej Miklaszewski, prof. PP
Instytut Inżynierii Materiałowej
Politechnika Poznańska
e-mail: andrzej.miklaszewski@put.poznan.pl

Oświadczenie

Niniejszym oświadczam, że w pracy P. Sochacka, **A. Miklaszewski**, K. Kowalski, M. Jurczyk, Influence of the Processing Method on the Properties of Ti-23 at.% Mo Alloy, Metals 9 (2019) 931. https://doi.org/10.3390/met9090931. mój udział polegał na wytworzeniu stopów Ti-23 at. % Mo metodą prasowania na gorąco, wsparciu merytorycznym podczas analizy wyników i redagowaniu artykułu. Jednocześnie wyrażam zgodę na wykorzystanie danych z tej publikacji na potrzeby przewodu doktorskiego Pani mgr inż. Patrycji Sochackiej.

.....
Podpis

Poznań, dnia 23 marca 2021 r.

dr inż. Kamil Kowalski
Instytut Inżynierii Materiałowej
Politechnika Poznańska
e-mail: kamil.kowalski@put.poznan.pl

Oświadczenie

Niniejszym oświadczam, że w pracy P. Sochacka, A. Miklaszewski, **K. Kowalski**, M. Jurczyk, Influence of the Processing Method on the Properties of Ti-23 at.% Mo Alloy, Metals 9 (2019) 931. https://doi.org/10.3390/met9090931. Mój udział polegał na pomocy przy wytworzeniu powłoki metodą MAO i EPD, jej obserwacji z wykorzystaniem mikroskopu skaningowego, wsparciu merytorycznym podczas analizy wyników i redagowaniu artykułu. Jednocześnie wyrażam zgodę na wykorzystanie danych z tej publikacji na potrzeby przewodu doktorskiego Pani mgr inż. Patrycji Sochackiej.

Kowalski

Podpis

Poznań, dnia 23 marca 2021 r.

prof. dr hab. Mieczysław Jurczyk
Instytut Inżynierii Materiałowej
Politechnika Poznańska
e-mail: mieczyslaw.jurczyk@put.poznan.pl

Oświadczenie

Niniejszym oświadczam, że w pracy P. Sochacka, A. Miklaszewski, K. Kowalski, **M. Jurczyk**, Influence of the Processing Method on the Properties of Ti-23 at.% Mo Alloy, Metals 9 (2019) 931. https://doi.org/10.3390/met9090931. mój udział polegał na przeprowadzeniu procesu mechanicznej syntezy, wytworzeniu stopów Ti-23 at. % Mo metodą topienia łukowego, prasowania i spiekania również z udziałem porofikatora, merytorycznej ocenie opracowanych wyników, redagowaniu artykułu oraz byciu autorem korespondencyjnym. Jednocześnie wyrażam zgodę na wykorzystanie danych z tej publikacji na potrzeby przewodu doktorskiego Pani mgr inż. Patrycji Sochackiej.

.....
Podpis

Poznań, dnia 23 marca 2021 r.

dr hab. inż Andrzej Miklaszewski, prof. PP
Instytut Inżynierii Materiałowej
Politechnika Poznańska
e-mail: andrzej.miklaszewski@put.poznan.pl

Oświadczenie

Niniejszym oświadczam, że w pracy P. Sochacka, **A. Miklaszewski**, M. Jurczyk, P. Pecyna, M. Ratajczak, M. Gajecka, M. U. Jurczyk, Effect of hydroxyapatite and Ag, Ta_2O_5 or CeO_2 addition on the properties of ultrafinegrained Ti31Mo alloy, J Alloys Compd. 823 (2020) 153749. https://doi.org/10.1016/j.jallcom.2020.153749. mój udział polegał na pomocy przy analizie strukturalnej XRD kompozytów, wsparciu merytorycznym podczas analizy wyników i redagowaniu artykułu. Jednocześnie wyrażam zgodę na wykorzystanie danych z tej publikacji na potrzeby przewodu doktorskiego Pani mgr inż. Patrycji Sochackiej.

.....

Podpis

Poznań, dnia 23 marca 2021 r.

prof. dr hab. Mieczysław Jurczyk
Instytut Inżynierii Materiałowej
Politechnika Poznańska
e-mail: mieczyslaw.jurczyk@put.poznan.pl

Oświadczenie

Niniejszym oświadczam, że w pracy P. Sochacka, A. Miklaszewski, **M. Jurczyk**, P. Pecyna, M. Ratajczak, M. Gajecka, M. U. Jurczyk, Effect of hydroxyapatite and Ag, Ta_2O_5 or CeO_2 addition on the properties of ultrafinegrained Ti31Mo alloy, J Alloys Compd. 823 (2020) 153749. https://doi.org/10.1016/j.jallcom.2020.153749. mój udział polegał na przeprowadzeniu procesów mechanicznej synezy, konsolidacji kompozytów, merytorycznej ocenie opracowanych wyników oraz redagowaniu artykułu. Jednocześnie wyrażam zgodę na wykorzystanie danych z tej publikacji na potrzeby przewodu doktorskiego Pani mgr inż. Patrycji Sochackiej.

.....
Podpis

Poznań, dnia 23 marca 2021 r.

mgr anal. med. Paulina Pecyna
Katedra i Zakład Genetyki i Mikrobiologii Farmaceutycznej
Uniwersytet Medyczny im. Karola Marcinkowskiego w Poznaniu
e-mail: paulinasawicka@ump.edu.pl

Oświadczenie

Niniejszym oświadczam, że w pracy P. Sochacka, A. Miklaszewski, M. Jurczyk, **P. Pecyna**, M. Ratajczak, M. Gajecka, M. U. Jurczyk, Effect of hydroxyapatite and Ag, Ta_2O_5 or CeO_2 addition on the properties of ultrafinegrained Ti31Mo alloy, J Alloys Compd. 823 (2020) 153749. https://doi.org/10.1016/j.jallcom.2020.153749. mój udział polegał na realizacji badań aktywności bakteryjnej wytworzonych materiałów oraz współpracy w analizie wyników tych badań. Jednocześnie wyrażam zgodę na wykorzystanie danych z tej publikacji na potrzeby przewodu doktorskiego Pani mgr inż. Patrycji Sochackiej.

Paulina Pecyna
Podpis

Poznań, dnia 23 marca 2021 r.

dr n. farm. Magdalena Ratajczak
Katedra i Zakład Genetyki i Mikrobiologii Farmaceutycznej
Uniwersytet Medyczny im. Karola Marcinkowskiego w Poznaniu
e-mail: mratajczak@ump.edu.pl

Oświadczenie

Niniejszym oświadczam, że w pracy P. Sochacka, A. Miklaszewski, M. Jurczyk, P. Pecyna, **M. Ratajczak**, M. Gajecka, M. U. Jurczyk, Effect of hydroxyapatite and Ag, Ta_2O_5 or CeO_2 addition on the properties of ultrafinegrained Ti31Mo alloy, J Alloys Compd. 823 (2020) 153749. https://doi.org/10.1016/j.jallcom.2020.153749. mój udział polegał na wykonaniu badań aktywności bakteryjnej wytworzonych materiałów oraz współpracy w analizie wyników tych badań. Jednocześnie wyrażam zgodę na wykorzystanie danych z tej publikacji na potrzeby przewodu doktorskiego Pani mgr inż. Patrycji Sochackiej.

Ratajczak

Podpis

UNIWERSYTET MEDYCZNY IM. KAROLA MARCINKOWSKIEGO W POZNANIU
KATEDRA I ZAKŁAD GENETYKI I MIKROBIOLOGII FARMACEUTYCZNEJ
Kierownik Katedry prof. dr hab. Marzena Gajęcka
Adres:
ul. Święcickiego 4
60-781 Poznań
tel./fax. (061) 854 67 20
e-mail: bakterio@ump.edu.pl

Poznań, 23.03.2021 r.

Oświadczenie

Niniejszym oświadczam, że w pracy P. Sochacka, A. Miklaszewski, M. Jurczyk, P. Pecyna, M. Ratajczak, **M. Gajecka**, M. U. Jurczyk, Effect of hydroxyapatite and Ag, Ta_2O_5 or CeO_2 addition on the properties of ultrafinegrained Ti31Mo alloy, J Alloys Compd. 823 (2020) 153749. https://doi.org/10.1016/j.jallcom.2020.153749. mój udział polegał na ocenie merytorycznej badań aktywności przeciwbakteryjnej wytworzonych materiałów. Jednocześnie wyrażam zgodę na wykorzystanie danych z tej publikacji na potrzeby przewodu doktorskiego Pani mgr inż. Patrycji Sochackiej.

KIEROWNIK
Katedry i Zakładu
Genetyki i Mikrobiologii Farmaceutycznej
prof. dr hab. Marzena Gajęcka

Poznań, dnia 23 marca 2021 r.

prof. dr hab. n. med. Mieczysława Urszula Jurczyk
Katedra i Klinika Zdrowia Matki i Dziecka
Uniwersytet Medyczny im. Karola Marcinkowskiego w Poznaniu
e-mail: mjur@poczta.onet.pl

Oświadczenie

Niniejszym oświadczam, że w pracy P. Sochacka, A. Miklaszewski, M. Jurczyk, P. Pecyna, M. Ratajczak, M. Gajecka, **M. U. Jurczyk**, Effect of hydroxyapatite and Ag, Ta_2O_5 or CeO_2 addition on the properties of ultrafinegrained Ti31Mo alloy, J Alloys Compd. 823 (2020) 153749. https://doi.org/10.1016/j.jallcom.2020.153749. mój udział polegał na pomocy przy badaniach aktywności bakteryjnej wytworzonych materiałów oraz współpracy w analizie wyników tych badań. Jednocześnie wyrażam zgodę na wykorzystanie danych z tej publikacji na potrzeby przewodu doktorskiego Pani mgr inż. Patrycji Sochackiej.

M. U. Jurczyk
.....
Podpis

Poznań, dnia 23 marca 2021 r.

prof. dr hab. n. med. Mieczysława Urszula Jurczyk
Katedra i Klinika Zdrowia Matki i Dziecka
Uniwersytet Medyczny im. Karola Marcinkowskiego w Poznaniu
e-mail: mjur@poczta.onet.pl

Oświadczenie

Niniejszym oświadczam, że w pracy P. Sochacka, **M. U. Jurczyk**, K. Kowalski, P. K. Wirstlein, M. Jurczyk, Ultrafine-Grained Ti-31Mo-Type Composites with HA and Ag, Ta_2O_5 or CeO_2 Addition for Implant Applications, Materials 14 (2021) 644. https://doi.org/10.3390/ma14030644. mój udział polegał na przeprowadzeniu testów biokompatybilności in vitro oraz analizie wyników tych badań. Jednocześnie wyrażam zgodę na wykorzystanie danych z tej publikacji na potrzeby przewodu doktorskiego Pani mgr inż. Patrycji Sochackiej.

M. U. Jurczyk
.....
Podpis

Poznań, dnia 23 marca 2021 r.

dr inż. Kamil Kowalski
Instytut Inżynierii Materiałowej
Politechnika Poznańska
e-mail: kamil.kowalski@put.poznan.pl

Oświadczenie

Niniejszym oświadczam, że w pracy P. Sochacka, M. U. Jurczyk, **K. Kowalski**, P. K. Wirstlein, M. Jurczyk, Ultrafine-Grained Ti-31Mo-Type Composites with HA and Ag, Ta_2O_5 or CeO_2 Addition for Implant Applications, Materials 14 (2021) 644. https://doi.org/10.3390/ma14030644. Mój udział polegał na pomocy przy wytworzeniu powłoki CaP metodą hydrotermalną, obserwacji z wykorzystaniem mikroskopu skaningowego wytworzonej powłoki oraz przekroju poprzecznego, wsparciu merytorycznym podczas analizy wyników i redagowaniu artykułu. Jednocześnie wyrażam zgodę na wykorzystanie danych z tej publikacji na potrzeby przewodu doktorskiego Pani mgr inż. Patrycji Sochackiej.

Podpis

Poznań, dnia 23 marca 2021 r.

dr n. med. Przemysław Krzysztof Wirstlein
Katedra Ginekologii, Położnictwa i Onkologii Ginekologicznej,
Klinika Rozrodczości
Uniwersytet Medyczny im. Karola Marcinkowskiego w Poznaniu
e-mail: abys@wp.pl

Oświadczenie

Niniejszym oświadczam, że w pracy P. Sochacka, M. U. Jurczyk, K. Kowalski, **P. K. Wirstlein**, M. Jurczyk, Ultrafine-Grained Ti-31Mo-Type Composites with HA and Ag, Ta_2O_5 or CeO_2 Addition for Implant Applications, Materials 14 (2021) 644. https://doi.org/10.3390/ma14030644. mój udział polegał na przeprowadzeniu testów biokompatybilności in vitro oraz analizie wyników tych badań. Jednocześnie wyrażam zgodę na wykorzystanie danych z tej publikacji na potrzeby przewodu doktorskiego Pani mgr inż. Patrycji Sochackiej.

.....
Podpis

Poznań, dnia 23 marca 2021 r.

prof. dr hab. Mieczysław Jurczyk
Instytut Inżynierii Materiałowej
Politechnika Poznańska
e-mail: mieczyslaw.jurczyk@put.poznan.pl

Oświadczenie

Niniejszym oświadczam, że w pracy P. Sochacka, M. U. Jurczyk, K. Kowalski, P. K. Wirstlein, **M. Jurczyk**, Ultrafine-Grained Ti-31Mo-Type Composites with HA and Ag, Ta_2O_5 or CeO_2 Addition for Implant Applications, Materials 14 (2021) 644. https://doi.org/10.3390/ma14030644. mój udział polegał na merytorycznej ocenie opracowanych wyników oraz redagowaniu artykułu. Jednocześnie wyrażam zgodę na wykorzystanie danych z tej publikacji na potrzeby przewodu doktorskiego Pani mgr inż. Patrycji Sochackiej.

.....
Podpis